Studies on Oxidation and Reactivity of Hydrocarbons/Biofuels/Ammonia

Doctoral Thesis

Thesis Title

Studies on Oxidation and Reactivity

of Hydrocarbons/Biofuels/Ammonia

Department of Mechanical Systems Engineering,

Graduate school of Engineering,

TOHOKU UNIVERSITY

YUKI MURAKAMI

Advising Professor at Tohoku Univ.	Associate Professor Nakamura, Hisashi
Research Advisor at Tohoku Univ.	
Dissertation Committee Members Name marked with "○" is the Chair of the Committee	○ Prof. Maruta, Kaoru 1 Prof. Kobayashi, Hideaki 2 Prof. Ju, Yiguang (Princeton University) 3 Associate Prof. Nakamura, Hisashi 4 Associate Prof. Hayakawa, Akihiro

TOHOKU UNIVERSITY
Graduate School of Engineering

Studies on Oxidation and Reactivity of Hydrocarbons/Biofuels/Ammonia

（炭化水素／バイオ燃料／アンモニアの酸化及び反応性に関する研究）

A dissertation submitted for the degree of Doctor of Philosophy (Engineering)

Department of Mechanical Systems Engineering

by

Yuki MURAKAMI

January 11 2022

Studies on Oxidation and Reactivity of Hydrocarbons/Biofuels/Ammonia

Yuki MURAKAMI

Abstract

The recent rapid climate change has led to a dramatic shift in the world's energy structure. There is a clear need to introduce low- and zero-carbon fuels that have a small environmental impact (e.g., syngas, methane, biofuels, hydrogen, and ammonia), in addition to efficient use of conventional fossil fuels. The objective of this dissertation is to investigate fundamental characteristics regarding oxidation and reactivity of low- and zero-carbon fuels in detail, and to identify the factors that control combustion phenomena, aiming at expanding the possibilities of utilization of such new fuels in practical combustion applications.

In Chapter 3, the combustion properties of reformate gases produced in an in-cylinder fuel reforming engine are investigated. First, combustion products from fuel reforming of a diesel component in an engine cylinder are estimated by 0-D adiabatic transient engine simulations. Initial temperatures and equivalence ratios are varied widely and their effects on reformate products are examined. Based on the simulated reformate product composition, representative reformate gas components are selected: CO, H_2 and CH_4. Composition of CO/H_2/CH_4 blends is varied widely, and its effects on reactivity of CO/H_2/CH_4/air mixtures are investigated using weak flame responses in a micro flow reactor with a controlled temperature profile (MFR). The results indicate that the reactivity of CO/H_2/CH_4/air mixtures is inhibited strongly as the CH_4 fraction in fuel blends increases. Chemical reaction analyses revealed that the OH radical consumption by CH_4 becomes larger and that by H_2 becomes smaller when the CH_4 fraction increases. Since CH_4 produces less reactive species such as CH_3, the mixture reactivity decreases as the CH_4 fraction increases.

In Chapter 4, the oxidation and reactivity of dimethyl ether (DME)/ammonia (NH_3) mixtures are investigated. Mixture composition and equivalence ratios of DME/NH_3/air mixtures are varied, and their effects on oxidation and reactivity of the mixtures are investigated. The results indicated that when the NH_3 fraction in DME/NH_3 blends is increased to 15%, the reactivity of DME/NH_3 mixtures is enhanced compared to the neat DME mixture. As the NH_3 fraction in DME/NH_3 blends is increased further, the reactivity of DME/NH_3 mixtures is decreased monotonically. It was found that low-to-intermediate temperature oxidation of DME induces NH_3 oxidation in the corresponding temperature region. The enhancement in the reactivity results from active radical production from loop reactions of NO and NO_2, which are produced from NH_3 oxidation. However, once the NH_3 fraction increases further, NH_3 consumes more OH radicals and oxidation of hydrocarbon species especially CO is inhibited, resulting in the decrease in the reactivity of DME/NH_3 mixtures. When the equivalence ratio is varied, almost no change in the reactivity is observed for the neat DME cases. However, the mixture reactivity is greatly decreased as the equivalence ratio is increased when NH_3 is blended with DME. It was found that the mixture reactivity decreases as the equivalence ratio increases because other species than CO (e.g., DME, CH_2O, NH_3 and H_2) consume more OH radicals due to high activation energy of CO.

In Chapter 5, the effects of high concentration of NO on oxidation and reactivity of CH_4/O_2/Ar

mixtures are investigated. The NO concentration in the mixture is varied for NO/CH_4 0.1–10%. The results showed that the reactivity of CH_4/O_2/Ar mixtures can be enhanced as the NO concentrations increase up to NO/CH_4 1.0% but slightly inhibited for NO/CH_4 10%. The radical sensitizing effects of NOx through looping reactions of NO and NO_2 can promote the oxidation of CH_4 and the conversion of CH_3 into CH_3O, realizing the oxidation sequence $CH_4 \rightarrow CH_3 \rightarrow CH_3O \rightarrow CH_2O \rightarrow HCO \rightarrow CO$ from the intermediate temperatures. When the NO fraction is increased to NO/CH_4 10%, a chain-propagating reaction $NO_2 + H = NO + OH$ and a chain-branching reaction $H + O_2 = O + OH$ compete for H radicals. Consequently, active radical production is inhibited slightly and the mixture reactivity is inhibited.

In Chapter 6, the characteristics of autoignition-assisted nonpremixed cool flames of diethyl ether (DEE) are investigated. As a first step, the conditions under which autoignition-assisted cool flames of DEE are observed are identified in the laminar counterflow flame experiment. As the fuel concentration decreases, the low temperature ignition limit merges with the extinction limit of cool flames, resulting in the autoignition-assisted cool flames. Under such conditions, the hysteresis between the cool flame and the unreactive mixture disappears and a monotonic transition between the unburning mixture and the steady cool flame occurs. Based the information from the laminar experiments, a turbulent autoignition-stabilized lifted cool flame of DEE/air was successfully observed at 550 K in a Co-flow Axisymmetric Reactor-Assisted Turbulent (CARAT) burner. A lift-off height scaling from a previous study of autoignition-stabilized laminar lifted flames is modified for this study to $H_L \sim U_0 \cdot \tau_{1st}^2$, where τ_{1st} is the first-stage ignition delay time in a homogeneous adiabatic reactor. A chemical kinetic model, which showed the best predictions of the measured laminar cool flame limits, also displayed the best correlation to the lift-off heights of turbulent cool flames.

Table of Contents

List of Figures

List of Tables

Chapter 1 :
Introduction

Due to the rapid climate change in recent years, a quick and drastic shift away from fossil fuels is required strongly in the global energy systems. The recent roadmap for the global energy sector presented by the International Energy Agency (IEA) suggests that the significant reduction of conventional fossil fuels such as oils, coals, natural gas is pivotal but is not sufficient for the “Net Zero by 2050” scenario, which aims to achieve net zero greenhouse gas (GHG) emissions by 2050 and to limit the rise in the global temperature to 1.5 ℃ [1]. In the roadmap, not only a rapid shift away from fossil fuels, but also the introduction of low- and zero-carbon fuels, such as hydrogen, hydrogen-based fuels, synthetic fuels, and biofuels, are required strongly.

In the global frameworks to reduce GHG emissions, as represented by the Kyoto Protocol (1997) [2] and the Paris Agreement (2015) [3], the goals are set for individual country. However, in the maritime industry, the GHG emissions regulatory standards are determined independently by the International Maritime Organization (IMO). This is because the nationality of vessels and that of operators are often different in the international shipping, which is not compatible with the country-specific reduction measures of these regulations [4]. Over the last several decades, IMO has focused mainly on the prevention of marine and air pollution caused by marine transportation based on the MARPOL protocol (1973/1978) [5],

the International Convention for the Prevention of Pollution from Ships. In the MALPOL protocol annex VI (2005) [6], strict regulations for SOx, NOx and particulate matter emissions from marine transportation had been adopted. In 2011, a chapter was added to the protocol, which sets energy efficiency standards for newly developed vessels [7]. However, these standards are not applied only to existing vessels. Surprisingly, the initial framework for reducing GHG emissions from marine transportation was introduced by IMO in 2018 [8]. This is the first global strategy to tackle GHG emissions in the maritime industry. The strategy sets three main goals: (1) 40% reduction in carbon intensity (i.e., CO_2 emissions per transport work) of international marine transportation by 2030 (compared to 2008), (2) 50% reduction in the annual GHG emissions from international marine transportation by 2050 (compared to 2008), and (3) net zero GHG emissions from international shipping as soon as possible within this century. However, any concrete global plans to achieve these goals have not been proposed yet. Currently, individual countries are formulating more strategic plans to achieve these goals. Very recently, a roadmap for achieving GHG emission goals, called “Shipping Zero Emission Project”, has been proposed by Japan Ship Technology Research Association (JSTRA) and Ministry of Land, Infrastructure, Transport and Tourism (MLIT) [4]. One of the major strategies proposed in the roadmap is replacement of conventional oils used in the maritime industry with low- or zero-carbon fuels including methane, hydrogen and ammonia as alternative energy sources. There are two possible scenarios proposed [4]: (a) Fuel shift from LNG to carbon-recycled methane and (b) Expansion of hydrogen and/or ammonia.

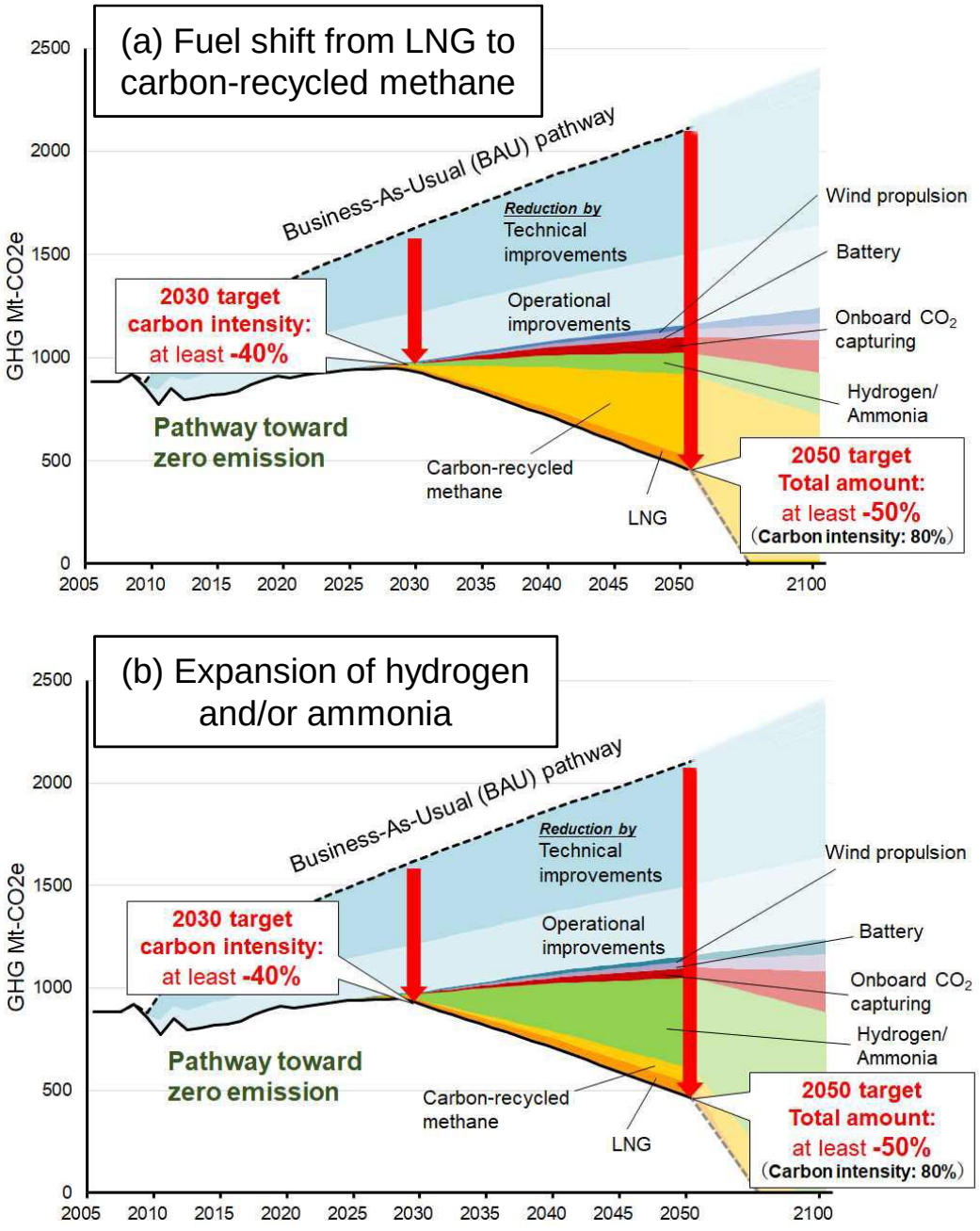

Figure 1-1: Possible scenarios for GHG emissions and reduction. (a) Fuel shift from LNG to carbon-recycled methane. (b) Expansion of hydrogen and/or ammonia [4].

Figure 1-1a presents the overview of GHG emissions in the scenario (a). This scenario assumes a situation, in which LNG-fueled vessels are widely used but hydrogen- or ammonia-fueled vessels are not because of insufficient fuel supply or infrastructure issues. LNG, carbon

recycled methane, and biofuels account for a vast part of reduction of GHG emissions in this case. On the other hand, Fig. 1-1b represents the overview of GHG emissions in the scenario (b). In this scenario, a situation is assumed, in which hydrogen- or ammonia-fueled vessels are introduced more widely than LNG-fueled vessels. Hydrogen and ammonia account for more part of reduction of GHG emissions than that in the scenario (a). In both scenarios, it is apparently inevitable to replace conventional fossil fuels with new, low- and zero-carbon fuels to reduce GHG emissions to a considerable degree. Moreover, the vast reduction of GHG emissions is supported significantly by technical and operational improvements.

Based on the drastic transformation surrounding the energy and emission strategies in the maritime industry over the last decade, this dissertation focuses on fundamental combustion characteristics of low- and zero-carbon fuels including synthetic gas, methane, biofuels and ammonia, aiming at expanding possibilities of use of such fuels in new and existing combustion applications. More specific subjects are introduced in the following sections.

1.1 In-cylinder fuel reforming

In Chapter 3, combustion properties of reformate gases produced in an in-cylinder fuel reforming engine are investigated. Since 2000s, soot and NOx emissions from international shipping have been restricted strictly due to severe environmental pollutions. In conventional diesel engines, since only air is compressed in the cylinder, the compression ratio can be increased, and high thermal efficiency can be achieved. However, when fuel is injected into

compressed air in an engine cylinder, it takes some time to vaporize liquid fuels, and autoignition may occur before mixing of a fuel and air is completed. The inhomogeneity of mixtures causes a rapid local temperature rise, leading to production of NOx and soot. As a major strategy to reduce NOx emissions, installation of DeNOx equipment using Selective Catalytic Reduction (SCR) technique has been recommended [9,10]. However, SCR systems are large usually and installation space could not be secured especially in small vessels. As a solution to these problems, in-cylinder fuel reforming engines are contrived. This type of engines utilizes liquid fuels and reduces soot and NOx emissions without having SCR systems [11]. A conceptual image of an in-cylinder fuel reforming engine is presented in Fig.1-2.

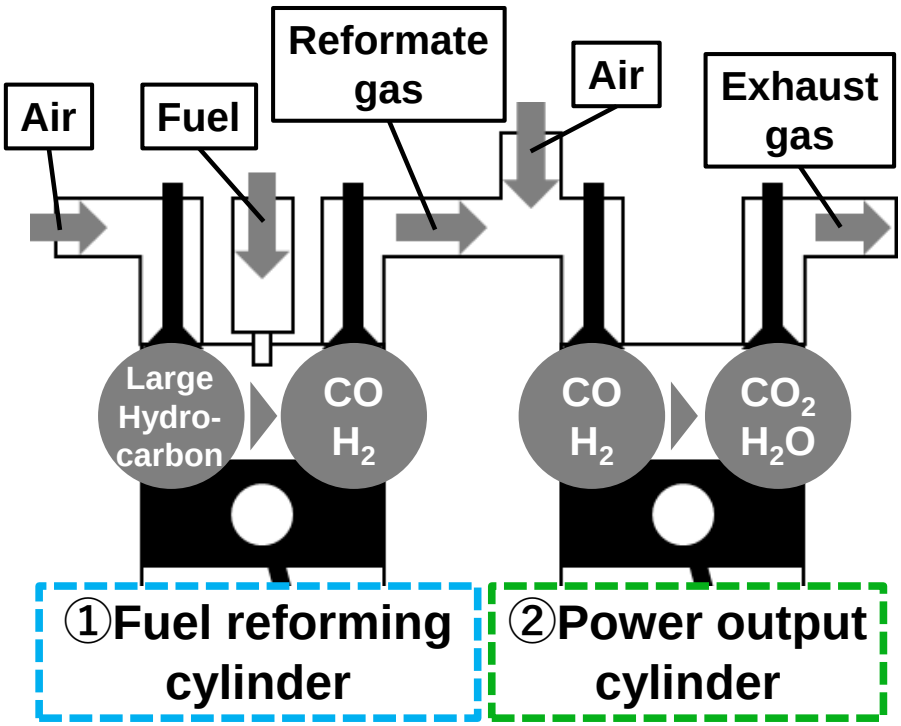

Figure 1-2: A conceptual image of in-cylinder fuel reforming engine.

In this engine, some cylinders are used for fuel reforming and the rests are used for power output. In a reforming cylinder, a reformate gas mixture, which includes mainly CO and H_2, is produced from partial oxidation of fuel/air mixtures under extremely fuel-rich conditions through piston compression-expansion strokes. The produced reformate gas is then introduced into an output cylinder with fresh air. Subsequently, combustion of the reformate gas/air mixture takes place near stoichiometry to extract power output. The ϕ–T diagram in Fig. 1-3, first proposed by Kamimoto et al. [12], presents the soot/NOx formation regime on an equivalence ratio–maximum temperature plane [13]. As shown in the ϕ–T diagram, the combustion condition of conventional diesel engines covers a large part of the soot and NOx formation regime. In fuel reforming cylinders, the flame temperature is expected to be low because of extremely fuel-rich conditions, which mitigates soot formation (regime ① in Fig. 1-3). In a power output cylinder, even near stoichiometry, a lower flame temperature condition can be realized because of the dilution with N_2, CO_2, and H_2O included in the reformate gas (regime ② in Fig. 1-3). Therefore, in-cylinder fuel reforming engines can realize low soot and NOx emission by controlling combustion conditions of each cylinder without having any exhaust gas treatment systems.

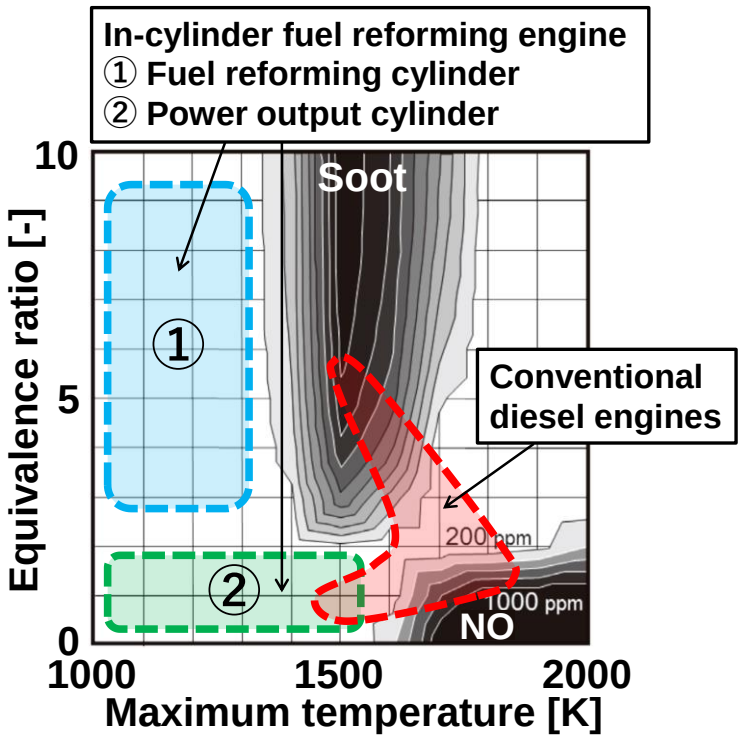

Figure 1-3: Combustion conditions of conventional diesel engines and in-cylinder fuel reforming engines described on ϕ-T diagram [12,13].

However, in fuel reforming engines, the composition of reformate products varies widely depending on reforming conditions. The variation in reformate gas composition has been reported in many practical applications such as biomass and coal reforming in stationary power plants [14–16]. Especially in the fuel reforming in small reciprocating systems, conditions such as pressure and temperature in a cylinder change greatly depending on operating conditions, thereby changing composition of reformate gas significantly. Moreover, the residence time for mixtures in an engine cylinder is limited to extremely short, which results in incompletion of fuel reforming. As a result, reformate contains a large amount of small hydrocarbons and diluents in addition to CO and H_2, the major components of reformate gas called syngas. Subsequently, this results in wide variation in the reactivity of

reformate gas which is utilized in power output cylinders. However, reactivity of syngas mixtures with small hydrocarbons and diluents has been investigated under limited conditions. In Chapter 3, fuel reforming characteristics in an engine cylinder are first investigated using a 0-D adiabatic transient engine model. Then, reactivity of representative reformate gas mixtures is examined using weak flame responses in a micro flow reactor with a controlled temperature profile (MFR), which is introduced in Chapter 2.

1.2 Ammonia/hydrocarbon combustion

Not only in maritime industry, but in the whole Japanese industry, ammonia (NH_3) has been considered as a promising hydrogen energy source to reduce CO_2 emissions. Fuel NH_3 has been selected as one of 14 representative sectors in “Green Growth Strategy Through Achieving Carbon Neutrality in 2050” proposed by Japanese government [17] in 2020. NH_3 contains no carbon atom in its molecule, and has high volumetric hydrogen density [18,19]. Actually, liquid NH_3 possesses high energy density that is 70% greater than that of liquid hydrogen [18]. Recently, Kurata et al. first reported a demonstration of power generation using a 50 kW class micro gas-turbine system powered solely by NH_3/air combustion [20]. They used strong swirl flows and preheating to compensate for low reactivity and low burning speed of NH_3 and stabilize NH_3/air flames in a gas turbine system. The combustion efficiency of the NH_3/air gas turbine system, which is defined as the ratio of the thermal efficiency of NH_3/air combustion normalized by that of the CH_4/air combustion under same operating

conditions, reached 89–96%, reflecting a strong potential of NH_3 to replace fossil fuels as an alternative energy source.

To compensate for the low reactivity and low burning speed of NH_3 as a fuel, blending NH_3 with fuels that are more reactive has been considered. Combustion properties of NH_3/H_2 blends have been investigated extensively during the last decade [21–27]. Many researchers have confirmed that H_2 addition can improve combustion properties of NH_3 dramatically, particularly in terms of ignition delay times [22,24,25] and of laminar burning velocity [21,23,26,27] at various temperatures, pressures, and fuel blend ratios. To expand opportunities for the practical use of NH_3 in existing combustion systems, fuel reactivity must be controlled flexibly to correspond to widely various power outputs. In this regard, researchers have started working on NH_3 blending with various hydrocarbon fuels [28–35]. From a rapid compression machine (RCM) experiment, Yu et al. reported ignition delay times of *n*-heptane/NH_3 mixtures [34]. Their results demonstrated that ignition delay times of *n*-heptane increased greatly as the NH_3 fractions in fuel blends increased, and especially demonstrated that NH_3 altered the low temperature reactivity of *n*-heptane. However, comparisons between their experimentally obtained results and numerical predictions showed large discrepancies. They concluded that the model predictions must be improved further to reproduce the measured ignition delay times quantitatively. Dai et al. recently assessed CH_4 [32] and DME [35] as an additive to NH_3. They measured ignition delay times of CH_4/NH_3 and DME/NH_3 mixtures in RCM experiments at high pressures. Their results indicated that,

even with very small fractions of CH_4 or DME (approx. 5%), reactivity of CH_4/NH_3 and DME/NH_3 mixtures is enhanced dramatically compared to neat NH_3 mixtures. They pointed out that, for both CH_4/NH_3 and DME/NH_3 mixtures, interaction between hydrocarbons and NH_3-related species strongly affects the early stage of fuel oxidation. Moreover, for DME/NH_3 mixtures, reactive species generated from the early-stage DME oxidation accelerate NH_3 oxidation. They emphasized the importance of understanding interaction between hydrocarbons and NH_3-related species, especially at low-to-intermediate temperatures, during the early stage of hydrocarbon oxidation occurs.

Despite intensive investigations on hydrocarbon/NH_3 mixture combustion, information related to the oxidation and reactivity of hydrocarbon/NH_3 mixtures remains inadequate. In Chapter 4, effects of mixture composition and equivalence ratios on the oxidation and reactivity of DME/NH_3 mixtures. Chemical reaction analyses based on experimental information and numerical simulation are conducted, particularly addressing chemical interactions between hydrocarbons and NH_3-related species.

1.3 Effects of nitric oxide on hydrocarbon oxidation

As mentioned in the previous section, NH_3 combustion has a great potential to contribute to zero CO_2 emissions because of its carbon-free nature. However, large amounts of NOx produced from NH_3 combustion have remained as one of challenges to overcome [18,36] in NH_3 combustion. In several studies, extremely high NO emissions with around 4000 volume

ppm from NH_3/CH_4 combustion have been reported [37–39]. Since NO has considerable effects on environmental pollutions, NO with such high concentration has to be processed properly and effectively. In conventional internal combustion engines, the exhaust gas recirculation (EGR) technique is introduced widely. EGR is introducing a part of exhaust gases to a fresh fuel/air mixture before combustion. With EGR, the maximum gas temperature decreases due to high specific heat capacities of exhaust gases. Lower combustion temperatures decrease heat loss to cylinder walls, resulting in higher thermal efficiency. Moreover, lower combustion temperatures suppress the production of thermal NO. EGR also can contribute to control ignition timings in internal combustion engines such as diesel engines and homogeneous charge compression ignition (HCCI) engines [40]. Chemically active species as NOx in exhaust gases play an important role in the ignition control of internal combustion engines. The sensitization by NO of oxidation of various fuels have been intensively investigated [41–48]. The sensitization of fuel oxidation results essentially from looping reactions of NO and NO_2. The destruction of hydrocarbon fuels is promoted by OH radicals produced from the interaction between NO/NO_2 and the H_2-O_2 system. Furthermore, intermediate hydrocarbon species also react with NO/NO_2, and overall oxidation process can be promoted. Dagaut et al. investigated effects of NO on the oxidation of natural gas components in JSR at 10 atm [47]. They pointed out that CH_3O_2 plays an important role at low pressure and low temperatures. Rasmussen et al. expanded the pressure conditions up to 100 atm and considered the sensitizing effects of NO on the CH_4 oxidation in the flow reactor

experiment [45]. Their results revealed that CH_3NO_2 has effects to inhibit the oxidation of fuel at extremely high-pressure conditions. Recently, Song et al. investigated the sensitizing effects of NO and NO_2 on the oxidation of CH_4 in JSR experiments [43]. The results showed that HONO, an intermediate species from NO–NO_2 looping reactions, also can enhance the sensitization of CH_4 oxidations by producing OH radicals especially at low temperatures. However, these studies concentrated on conditions with limited NO concentrations (up to 1000 ppm in test mixtures). As mentioned earlier, in some practical applications such as NH_3/hydrocarbon combustion and NO reburning techniques, NO concentration in a reaction zone is expected to be much higher [37–39]. However, effects of high concentration NO on hydrocarbon oxidation have not been investigated well. Motivated by these facts, Chapter 5 focuses on the effects of high concentration NO on oxidation and reactivity of hydrocarbons.

1.4 Autoignition-assisted cool flames

Ignition control is a critically important factor for the efficient engine operation especially for conventional diesel engines and homogeneous charge compression ignition (HCCI) engines, in which ignition timing is dominated by mixture reactivity. In diesel engines, for example, autoignition and autoignition-assisted flame propagation are the dominant events within the combustion process [49]. Specifically, for diesel fuels, autoignition events are initiated by first-stage ignition and subsequent transition to a cool flame. The cool flame then propagates across unburned mixtures from a lean side to a rich side [50]. Subsequently,

second-stage (hot) ignition occurs in locally-rich mixtures, that eventually transition into turbulent hot flames that propagate back from the rich mixture to the location of the stoichiometric contour [50–52]. Since these events often occur under turbulent conditions and at high autoignition Damköhler numbers, the interaction of turbulence with autoigniting cool flames should be further investigated [51,53–56]. Recently, Zhang et al. [57] pointed out that flame structure and flame propagation speed of cool flames can change dramatically depending on autoignition Damköhler numbers, which are defined as the ratio between the flow residence time and the chemical reaction time, i.e., the first-stage ignition delay time for cool flames (or the total ignition delay time for hot flames). However, the majority of cool flame experimental studies were conducted with laminar flames at low autoignition Damköhler numbers in which flame stabilization and autoignition are decoupled [58–60]. Few experiments have been conducted to understand flame transition from cool flames to hot flames and/or behavior of autoignition-assisted turbulent cool flames. The absence of such experiments under both laminar and turbulent conditions leaves a gap in understanding the role of autoignition in cool flame stabilization.

Recently, Novoselov et al. experimentally and computationally investigated the interaction between dimethyl ether cool flames and turbulence in a nonpremixed turbulent jet flow at a low autoignition Damköhler number [61]. The results revealed that the flame stabilization location was very sensitive to the burner exit temperatures. As a result, the numerical simulations were difficult to compare directly with the measurements due to the

large uncertainty in the burner exit temperatures. On the other hand, the stabilization of autoignition-assisted flames is primarily controlled by chemical kinetics, in which the stabilization mechanism is dictated by the balance between heat loss and heat generation due to autoignition. In this regard, chemical kinetic models which give better predictions of characteristics of autoignition-assisted flames are required strongly. Therefore, there is a clear need to study low-temperature autoignition-assisted flames to understand flame stabilization mechanisms at high autoignition Damköhler numbers, and also to validate existing chemical kinetic models. In Chapter 6, the flame stabilization and flame transition of autoignition-assisted nonpremixed cool flames of diethyl ether (DEE) are investigated. Firstly, the autoignition and extinction limits of laminar nonpremixed cool flames are examined in a counterflow burner configuration. Based on the information obtained in the laminar flame measurements, turbulent nonpremixed cool flames are established by using a Co-flow Axisymmetric Reactor-Assisted Turbulent (CARAT) burner. Finally, a correlation between the lift-off heights of turbulent cool flames and the first-stage ignition delay times is examined.

1.5 Outlines of the dissertation

Motivated by backgrounds mentioned in the earlier sections, this dissertation investigates oxidation and reactivity of various low carbon fuels including small hydrocarbons, biofuels, and ammonia in terms of combustion chemistry and flame dynamics. The principal objectives are as follows:

1. To estimate combustion products from in-cylinder fuel reforming of large hydrocarbons and to evaluate reactivity of the representative reformate gases.
2. To investigate detail oxidation and reactivity of biofuel/ammonia mixtures, especially paying attention to interactions between hydrocarbon and NH_3 at low-to-intermediate temperatures.
3. To clarify effects of high concentration NO on hydrocarbon oxidation and reactivity.
4. To investigate characteristics of autoignition-assisted cool flames under both laminar and turbulent conditions.

This dissertation comprises seven chapters. In Chapter 1. The background and objectives of this dissertation are presented. Experimental platforms employed in this dissertation (i.e., a micro flow reactor with a controlled temperature profile (MFR), a laminar counter flow burner, and a Co-flow Axisymmetric Reactor-Assisted Turbulent (CARAT) burner) are introduced in Chapter 2. In Chapter 3, the in-cylinder fuel reforming concept is considered. Reformate products from partial oxidation of a hydrocarbon fuel in an engine cylinder are estimated based on a 0-D adiabatic transient computation. Representative reformate products under realistic engine operation conditions are identified. Reactivity changes depending on reformate gas composition are evaluated based on weak flame responses in MFR. Chapter 3 has been adapted from the following publication [62]: Yuki Murakami, Hisashi Nakamura, Takuya Tezuka, Go Asai, Kaoru Maruta, “Reactivity of $CO/H_2/CH_4$/air Mixtures derived from

In-cylinder Fuel Reformation Examined by a Micro Flow Reactor with a Controlled Temperature Profile", Combustion Science and Technology, Vol.193, No.2 : 266-279 (2021).

In Chapter 4, effects of fuel blending ratios and equivalence ratios on oxidation and reactivity of dimethyl ether (DME)/ammonia (NH_3) mixtures are investigated. Mixture composition and equivalence ratios of DME/NH_3/air mixtures are varied as parameters, and the effects of these parameters on oxidation and reactivity of the mixtures are investigated based on weak flame responses in MFR. Chapter 4 has been adapted from the following publication [63]: Yuki Murakami, Hisashi Nakamura, Takuya Tezuka, Kenji Hiraoka, Kaoru Maruta, "Effects of mixture composition on oxidation and reactivity of DME/NH_3/air mixtures examined by a micro flow reactor with a controlled temperature profile", Combustion and Flame, Vol. 238, 111911 (2022).

In Chapter 5, effects of high concentration NO on methane oxidation are investigated. NO concentration in CH_4/O_2/Ar mixtures is varied widely, and changes in mixture oxidation and reactivity are evaluated with weak flame responses in MFR.

In Chapter 6, characteristics of autoignition-assisted cool flames of a biofuel are investigated under laminar and turbulent conditions. A counterflow burner for laminar experiment and a Co-flow Axisymmetric Reactor-Assisted Turbulent (CARAT) burner for turbulent experiment are employed. The work of Chapter 6 was conducted under the supervision by Professor Yiguang Ju in Princeton University. Chapter 6 has been adapted from the following publication [64]: Yuki Murakami, Christopher B. Reuter, Omar R. Yehia,

Yiguang Ju, “Studies of autoignition-assisted nonpremixed cool flames”, Proceedings of the Combustion Institute, Vol. 38, Issue 2:2333-2340 (2021).

Finally, the conclusions of this dissertation are presented in the Chapter 7.

Chapter 2 :

Experimental platforms

2.1 Micro flow reactor with a controlled temperature profile (MFR)

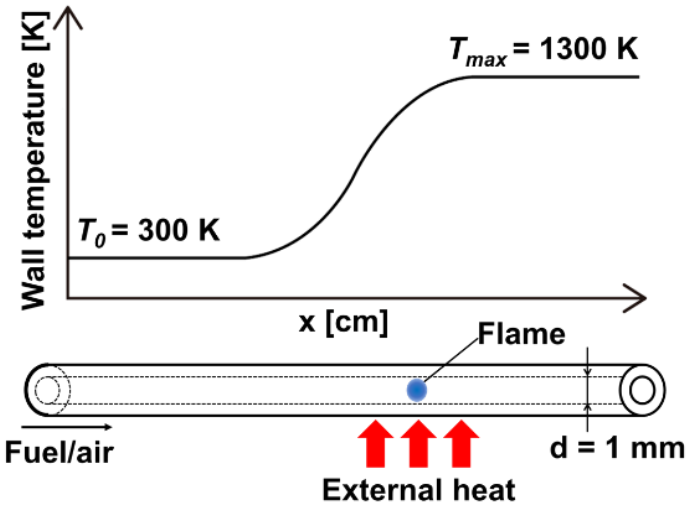

Figure 2-1: Schematic of a micro flow reactor with a controlled temperature profile.

To investigate oxidation and reactivity of given fuels effectively, a micro flow reactor with a controlled temperature profile (MFR) is used in several chapters of this dissertation (Chapter 3, 4, 5). MFR was first introduced by Maruta et al. in 2005 [65] to investigate flame dynamics in a heated micro channel. A schematic of the MFR system is presented in Fig. 2-1. The system comprises a quartz tube and an external heat source (e.g., a burner flame or an electric heater). The inner diameter of the quartz tube is smaller than the ordinary diameter of given fuels. A stationary wall temperature profile is formed along the quartz tube by the external heat source. Once a mixture of a given fuel and an oxidizer is introduced into the

reactor, oxidation of fuel proceeds as the wall temperature increases in the flow direction. From the past studies using MFR, it was confirmed that there exist three types of different flame responses depending on inlet flow velocity of a mixture, which will be introduced in the following section.

2.1.1 Flame responses in MFR

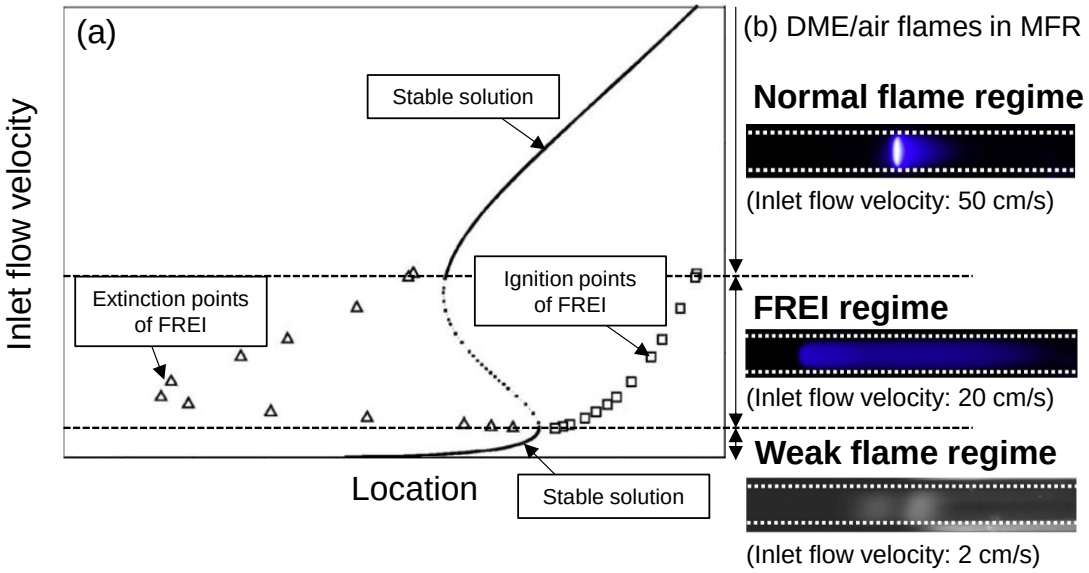

Figure 2-2: Flame responses observed in MFR [66,67].

Figure 2-2a presents the general relation between flame locations and inlet flow velocity (indicated with solid/dotted lines) obtained by a theoretical analysis for the MFR system [66]. Additionally, examples of the flame images of corresponding flame responses for stoichiometric dimethyl ether (DME)/air mixtures [67] are shown in Fig. 2-2b. The vertical axis of Fig. 2-2a is inlet flow velocity and the horizontal axis is spatial locations in MFR. Analytical solution (equivalent to flame location) shows a S-shaped curve which has three

branches. The solid lines correspond to stable solutions and the dotted line represents unstable solutions. The upper stable branch corresponds to normal flames. The middle branch indicated by a dotted line is unstable solution, in which FREI (Flames with Repetitive Extinction and Ignition [65]) phenomena are observed experimentally at this intermediate flow velocity. FREI are a cyclic phenomenon involving autoignition, autoignition front propagation and flame extinction. Under FREI conditions, autoignition of mixtures occurs first at a high temperature region in MFR. Then a reaction front (or an ignition kernel) propagates upstream and extinguishes at a low temperature region due to increasing heat loss. A low-velocity branch indicated by a solid line corresponds to weak flame. Ignition (square symbols) and extinction positions (triangle symbols) of FREI are also indicated in the figure. Ignition points of FREI are smoothly connected to the weak flame branch. Those points and weak flame branch are equivalent to the ignition branch of the Fendell curve [68]. Weak flames indicate "ignition-related property of given mixture" although it is steady unconventional flame [67,69–71].

2.1.2 Weak flames in MFR

In the weak flame regime, the local gas temperature increase by heat generation from combustion chemical reactions is extremely small (around 10–20 K) because of small chemical enthalpy input (less than 1 W, in general). Note that wall temperature profile in flow direction is maintained by an external heat source. By having a tube with a diameter below

ordinary quenching diameters, the gas-phase temperatures are strongly governed by the wall temperatures defined by an external heat source, particularly at low inlet flow velocity. Therefore, the temperature of a weak flame is close to the local wall temperature and overall thermal runaway is suppressed. In general, ordinary ignition phenomena are observed as transient phenomena with radical pool growth and subsequent thermal runaway. On the contrary for weak flames in MFR, chemical reactions occurring in ignition phenomena is reproduced as steady solution in the form of steady "weak flames". For such low flow velocity where weak flames are observed, flow velocity is almost insensitive to weak flame locations [67,71,72].

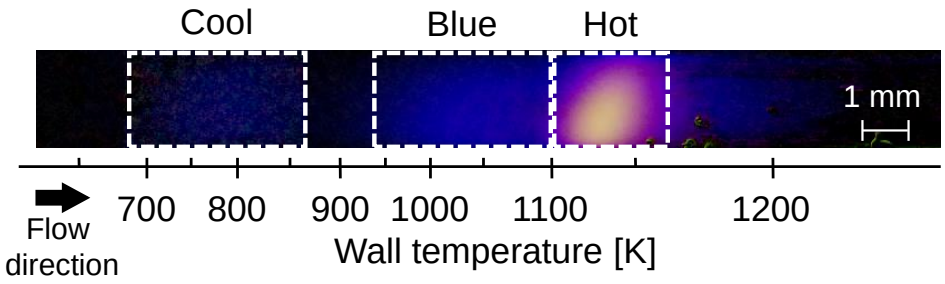

Figure 2-3: Weak flame of stoichiometric *n*-heptane/air mixtures at inlet flow velocity of 1.2 cm/s [70].

Another characteristic feature of weak flames is that a weak flame of a given fuel with multi-stage oxidation simultaneously appears as three separated weak reaction zones. The weak flame of a stoichiometric n-heptane/air mixture is presented in Fig. 2-3 [70]. Three chemiluminescence zones are observed at temperatures of 700–850 K, 950–1100 K and 1100–

1150 K. Speciation profiles for a stoichiometric n-heptane/air weak flame are presented in Fig. 2-4.

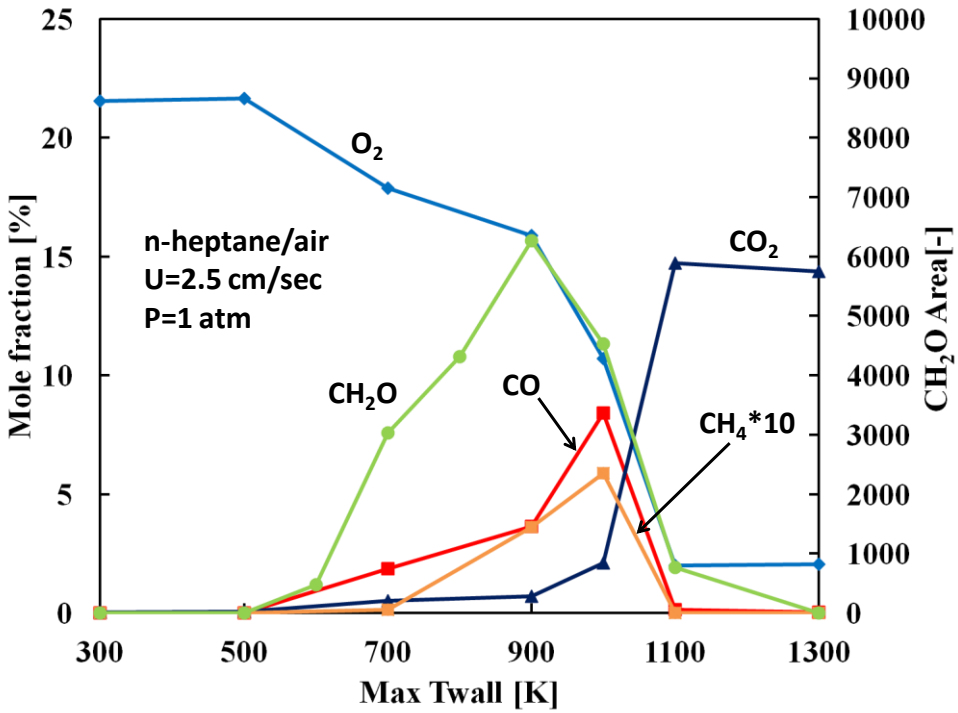

Figure 2-4: Measured species profiles of the stoichiometric *n*-heptane/air weak flame at atmospheric pressure and inlet flow velocity of 2.5 cm/s [69].

In typical transient multi-stage ignition, low-temperature oxidation is characterized by the formation of CH_2O. As seen in Fig. 2-4, CH_2O is produced from 600–700 K. This reaction zone is called "cool flame". CH_2O is then consumed in the early stage of high-temperature reaction at around 900–1000 K and the large amount of CO is formed. This reaction zone is called "blue flame". The term "blue flame" has been used since 1940s (e.g., the work by Topps and Townend [73]) to distinguish it from cool and hot flames. Finally, CO and other unburned species are completely oxidized to CO_2 at around 1000–1100 K. This

reaction zone is called “hot flame”. In summary, respective reaction zones are termed as follows: “cool flame” for the initial oxidation of fuel and the production of CH_2O, “blue flame” for the oxidation from CH_2O to CO and “hot flame” for the oxidation from CO to CO_2. It is also interesting to note that “blue flame” is recently termed as “warm flame” [56], as this reaction zone locates in between “cool flame “ and “hot flame”. The first, second and third chemiluminescence zones observed in the weak flame in Fig. 2-3 correspond to cool, blue, and hot flames, respectively.

Additionally, locations of three reaction zones of weak flames could be used as a measure of reactivity of given fuels. As an example, weak flame images of fuels with different research octane numbers (RONs) are presented in Fig. 2-5 [70]. Two or three chemiluminescence zones appear in the flow direction, corresponding to cool, blue and hot flames from the low temperature side. As seen in Fig. 2-5, hot flames shift to the higher temperature side as the RON increases. This trend indicates that weak flames of fuels with lower and higher reactivity locate in at higher and lower temperature regions in the reactor. In Fig. 2-5, the difference in mixture reactivity between RON 0 and 100 appears as a 40 K difference in wall temperatures at hot flame locations. Figure 2-6 presents weak flames of fuels with different cetane numbers (CNs) [74]. In this case, the difference in mixture reactivity between CN 100 and 15 appears as a 20 K difference in wall temperatures at hot flame locations. These features of weak flames realizes the evaluation of reactivity of not only conventional hydrocarbons [67,70,71,74,75] but also ammonia [76] and hydrofluorocarbons

[77,78]. In Chapter 3, 4 and 5, reactivity of different test mixtures is evaluated relying on weak flame locations in MFR.

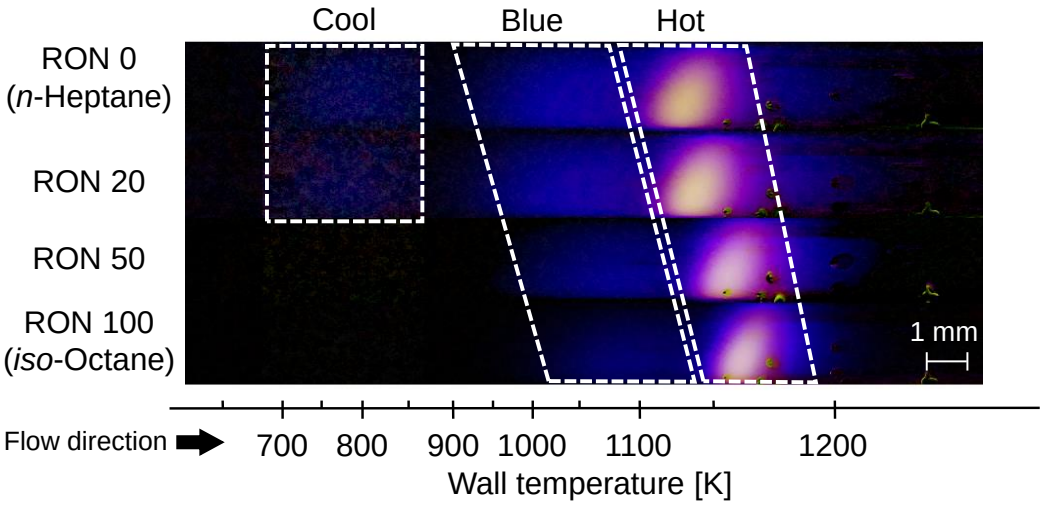

Figure 2-5: Weak flames of fuels with different RONs (Research Octane Numbers) [70].

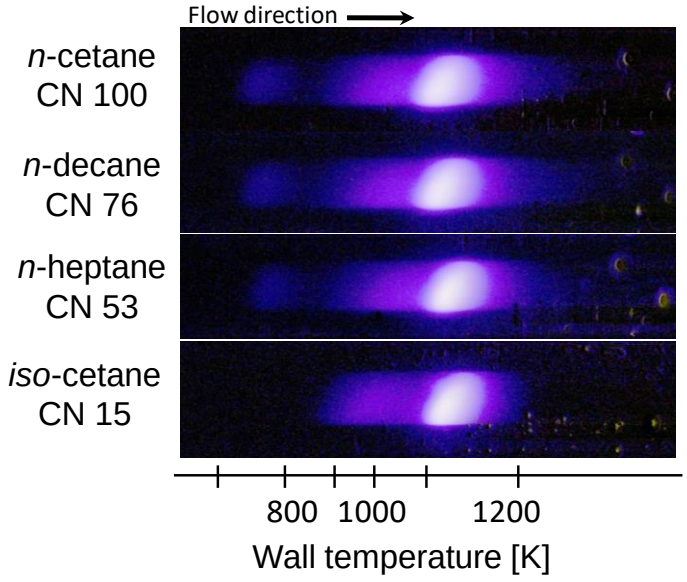

Figure 2-6: Weak flames of fuels with different CNs (Cetane Numbers) [74].

2.2 Counterflow burner

In Chapter 6, an atmospheric laminar counterflow burner is utilized to investigate characteristics of cool flames under laminar conditions. The structure of the counterflow burner is depicted in Fig. 2-7. The exit diameter (*D*) of both the top and bottom burner nozzles is 13 mm. Each nozzle is surrounded by a co-flow channel in which heated nitrogen flows. The burner separation distance (*L*) is kept at 22.5 mm throughout all measurements. A global strain rate (*a*) is conventionally defined as follows [79]:

$$a = 2\left(\frac{U_O}{L}\right)\left(1 + \frac{U_F\sqrt{\rho_F}}{U_O\sqrt{\rho_O}}\right) \tag{2.1}$$

where U_o and U_F are the respective velocities of the oxidizer and fuel flows at nozzle exits, ρ_O and ρ_F are the densities of the oxidizer and fuel flows at nozzle exits, and L is the burner nozzle separation distance. When the two streams are momentum balanced, the global strain rate is simply expressed as follows:

$$a = \frac{4U_O}{L}. \tag{2.2}$$

A fuel/nitrogen mixture is expelled out of the upper burner nozzle and meets the heated air flow from the bottom nozzle. Both the upper and lower nozzles are surrounded by nitrogen co-flows. In Chapter 6, all the flows are heated to 550 K at the nozzle exits, unless otherwise stated. The temperatures of the flow at the nozzle exits are maintained within ±5 K using PID control. Since the cool flame chemiluminescence is quite dim, an unfiltered ICCD camera (Princeton Instruments, PI-MAX 4) is used to monitor the cool flame chemiluminescence.

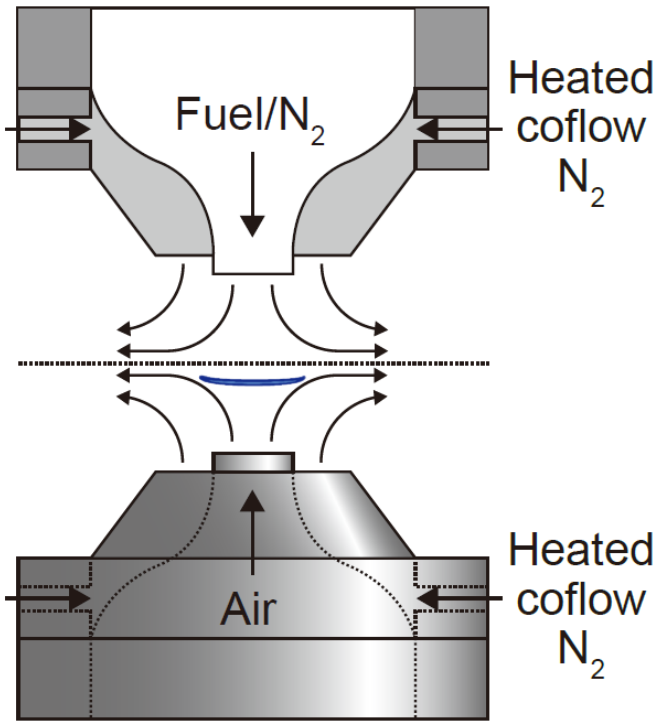

Figure 2-7: Schematic of the structure of the counterflow burner.

2.3 Co-flow Axisymmetric Reactor-Assisted Turbulent (CARAT) burner

In Chapter 6, cool flame characteristics under turbulent conditions are also investigated. To stabilize turbulent cool flames at well-defined boundary conditions, the Co-flow Axisymmetric Reactor-Assisted Turbulent (CARAT) burner [61] is employed. The CARAT burner is an upgraded version of the Reactor-Assisted Turbulent Slot (RATS) burner. The structure of CARAT burner is depicted in Fig. 2-8. The CARAT burner has three flows: an inner (main) fuel flow, a pilot flow, and a co-flow. The inner fuel channel has a diameter of 1.5 cm. The pilot flow passes through a small annulus which has a width of 0.2 cm surrounding the main nozzle. A large exterior channel with a width of 3.8 cm contains the co-flow. The heated co-flow passes through a ceramic honeycomb mesh, which allows for flow laminarization and the specification of well-defined boundary conditions.

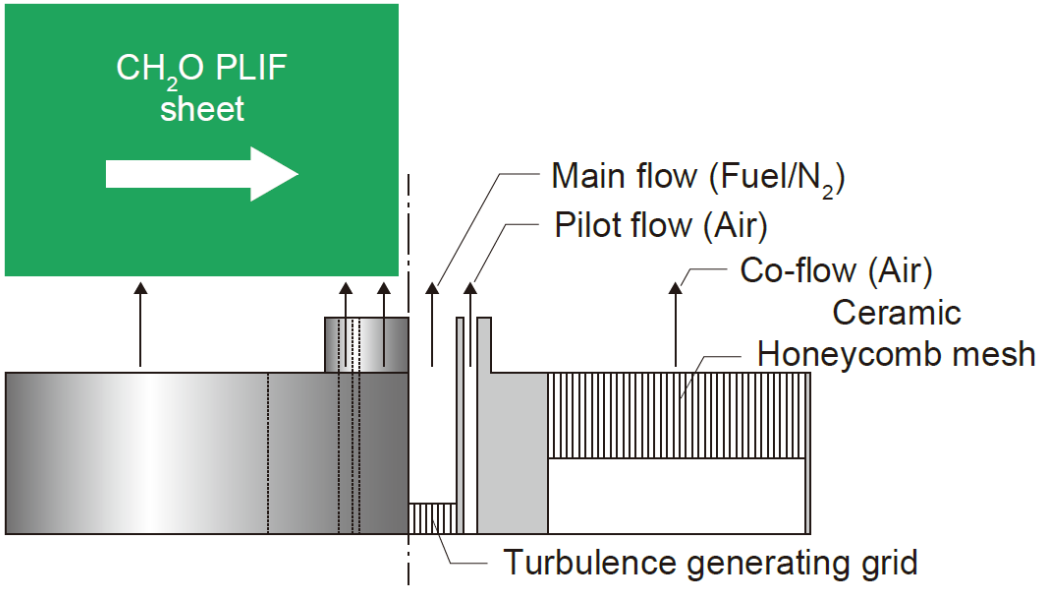

Figure 2-8: Schematic of the Co-flow Axisymmetric Reactor-Assisted Turbulent (CARAT) burner.

The turbulent Reynolds number (Re_T) is defined as follows:

$$Re_T = \frac{u_{rms} L_{int}}{\nu} \tag{2.3}$$

where u_{rms} is the root mean square of the turbulent velocity fluctuations, L_{int} is the integral length scale, and ν is the kinematic viscosity. The turbulent flow field characterization was performed at room temperature (T = 295 K) with air using a nanoscale thermal anemometry probe (NSTAP) operated with a Dantec Dynamics Streamline Pro Constant Temperature Anemometry system. The NSTAP was positioned at the centerline of the main nozzle exit (approximately even with the exit plane) and sampled at a frequency of 10 kHz, which significantly exceeded all temporal scales in the flow. The u_{rms} measured by the probe is defined as the square root of the variance of the measured velocity. The integral time scale (τ_{int}) of the velocity fluctuations is determined by extrapolating the power spectral density

towards zero frequency. By applying Taylor's frozen field hypothesis, L_{int} can be calculated as the product of the mean main flow velocity and the integral time scale. The respective correlations between the turbulence intensity and the bulk Reynolds number ($u_{rms}/U = f(Re_D)$), and between the integral length scale and the bulk Reynolds number ($L_{int} = f(Re_D)$) were estimated. By reflecting Re_D for elevated temperatures and test fluids to the correlations, the turbulent Reynolds number (Re_T) was estimated. The turbulent Reynolds number is kept low to prevent the cool flame from blowing off at the current experimental conditions ($Re_T \sim 30$). For one of the test conditions for turbulent nonpremixed cool flames in Chapter 6 (4% diethyl ether/96% nitrogen flow, T = 550 K, U = 3.0 m/s), the velocity fluctuation is u_{rms} = 0.49 m/s, the integral length scale is L_{int} = 2.31 mm, the bulk Reynolds number is Re_D = 1124, and the turbulent Reynolds number is calculated as Re_T = 28.

Chapter 3:
Reactivity of $CO/H_2/CH_4$/air mixtures derived from in-cylinder fuel reforming

3.1 Introduction

As introduced in Chapter 1, reducing soot and NOx emissions from marine transportation has been a global challenge. To avoid production of these pollutants from conventional diesel engines, the in-cylinder fuel reforming concept is considered. In this chapter, reformate products from partial oxidation of *n*-tridecane/air mixtures in an engine cylinder are estimated using a 0-D adiabatic transient computation. Representative reformate products under realistic engine operation conditions are identified. Based on composition analyses on reformate products, $CO/H_2/CH_4$/air mixtures are selected as target mixtures. Variation in mixture reactivity due to reformate gas composition is evaluated based on weak flame responses in MFR.

As the first step of this study, in-cylinder fuel reforming of a large hydrocarbon fuel is investigated using a 0-D adiabatic engine model. Details of this computation are provided in Appendix 3.A. The computation simulates one cycle of piston compression-expansion strokes in an engine cylinder under adiabatic condition. The equivalence ratio and the initial temperature of fuel/air mixtures are varied and their effects on the compositions of reformate products are investigated. Figure 3-1 presents the estimated mole fractions of representative

reformate products. According to the results, CO and H_2 are the major products for the lower equivalence ratios, ϕ = 1–5, whereas other species, especially small hydrocarbons such as CH_4, C_2H_4 are producible for higher equivalence ratios, ϕ = 5–10. A similar trend was also confirmed in experiments with a lab-scale diesel engine [80]. The variation in the composition of reformate products may changes the reactivity of mixtures considerably, thereby exerting marked effects on the design and the development of engines. Therefore, the impacts of small hydrocarbons on the reactivity of reformate gases should be further investigated.

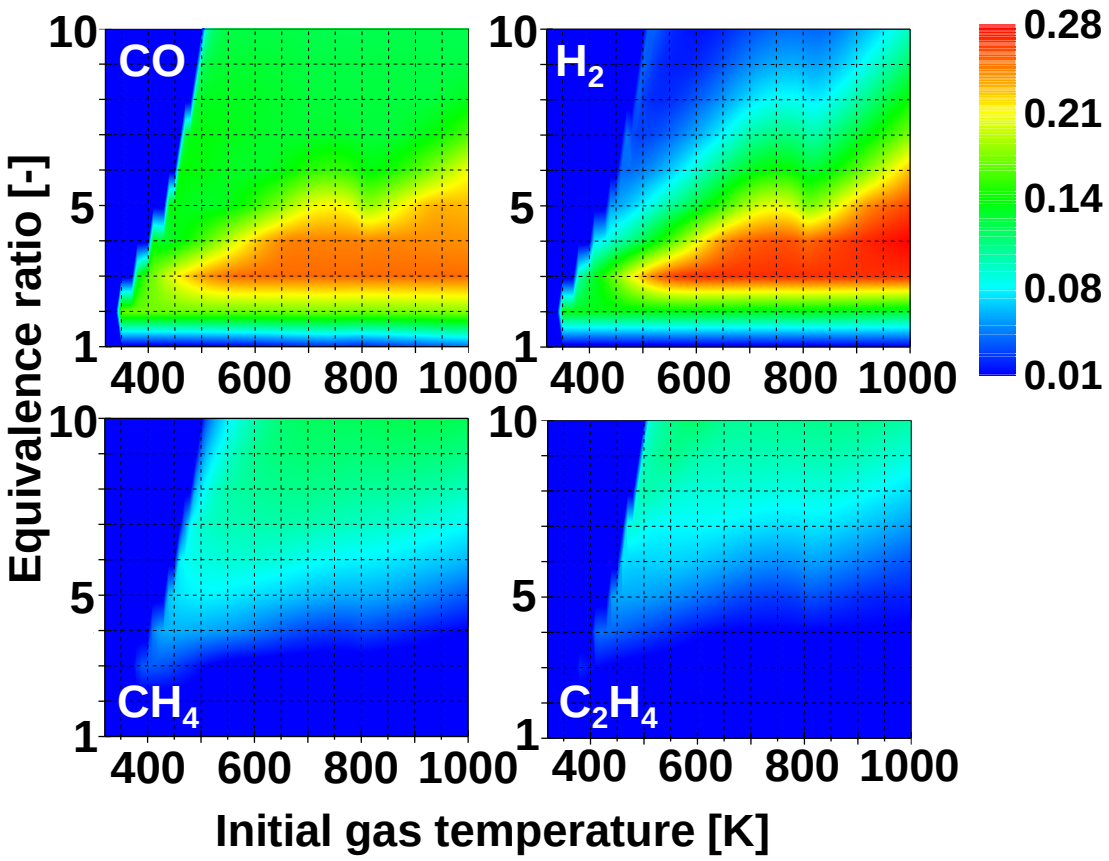

Figure 3-1: Computed mole fractions of CO, H_2, CH_4 and C_2H_4 produced in fuel reforming of *n*-tridecane/air mixtures after one cycle of piston compression-expansion strokes in an engine cylinder at adiabatic condition.

Although many studies have assessed the reactivity of pure CO/H_2 mixtures experimentally [81–86], experimental investigations on the reactivity of reformate gas including small hydrocarbons are still quite limited.. To present target mixture conditions investigated in the present study and earlier works considering the reactivity of CO/H_2 mixtures with small hydrocarbons [28,87–90], a $CO\text{-}H_2\text{-}CH_4$ ternary diagram is introduced (Fig. 3-2). CH_4 is selected as a representative small hydrocarbon because it is the simplest hydrocarbon and the most likely to be included in reformate products besides CO and H_2. For the conditions presented in Fig. 3-2, the mole fractions of CO, H_2 and CH_4 are extracted from the literatures [28,87–90] and normalized. As might be readily apparent, most cases are located on several specific regions in the diagram. The mixture conditions around CO/H_2 = 50/50 (the green shaded region) are intended for mixtures from coal and biomass reforming [28,88,89]. The conditions including a large amount of CH_4 (the yellow shaded region) are considered for the utilization of synthetic natural gas [87] and for dual fuel applications of natural gas and reformate gases [90]. On the other hand, the estimated mixture conditions for in-cylinder fuel reforming engines [91] are depicted as the blue shaded region, where few experimental data exist. These trends indicate that target composition can differ widely depending on applications, and few investigations have been conducted for mixtures including CO, H_2, and CH_4 simultaneously.

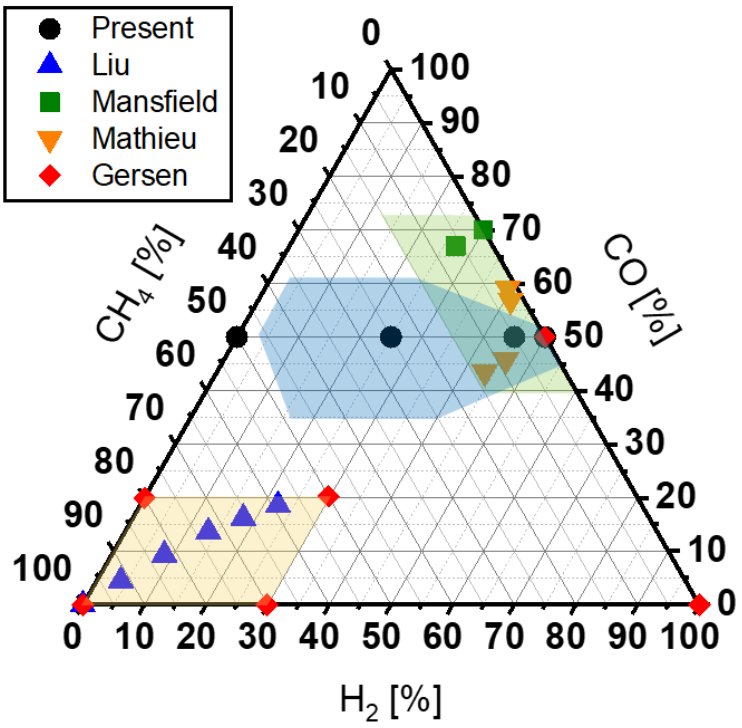

Figure 3-2: Ternary diagram indicating mixture conditions experimentally investigated the reactivity of CO–H_2–CH_4 mixtures in the present and earlier studies [28,87–90]**.**

Motivated by these facts, the effects of composition changes in CO/H_2/CH_4 mixtures on the reactivity are evaluated based on weak flame responses in MFR. Specifically, the ratios of H_2 and CH_4 are varied widely while the CO fraction is kept constant. Further details of the mixture composition investigated in this study are presented later. Experimental measurements are compared to computational predictions using several detailed chemical reaction models. A further chemical reaction analyses are then conducted to investigate dominant chemical reactions behind a trend observed in the experiments.

3.2 Experimental and computational methods

3.2.1 Experimental conditions

A quartz tube (inner diameter: 1 mm, outer diameter: 3 mm) is used as the reactor channel. The reactor is arranged in the horizontal direction. A H_2/air flat-flame burner is installed under the reactor to form a stationary temperature profile with the maximum temperature of 1300 K along the reactor wall. Flames are observed using a digital still camera (Nikon D800) with a bandpass filter (Optical Coating Japan, DIF-BP, 431.4 nm transparent wavelength, 6.5 nm half bandwidth) to exclude thermal radiation from the heated reactor wall. Flame images are taken after at least 15 mins so that the mixture flow is stabilized. The exposure time is fixed as 3 mins because the chemiluminescence from weak flames is quite dim. A measured flame location is defined as the location of the peak of the brightness profile extracted from a flame image. Each experiment is conducted at atmospheric pressure. Since the test mixtures in the present study includes CO, brass material is used for the purpose of preventing the formation of CO complex, which reportedly affects the combustion characteristics of syngas mixtures [92].

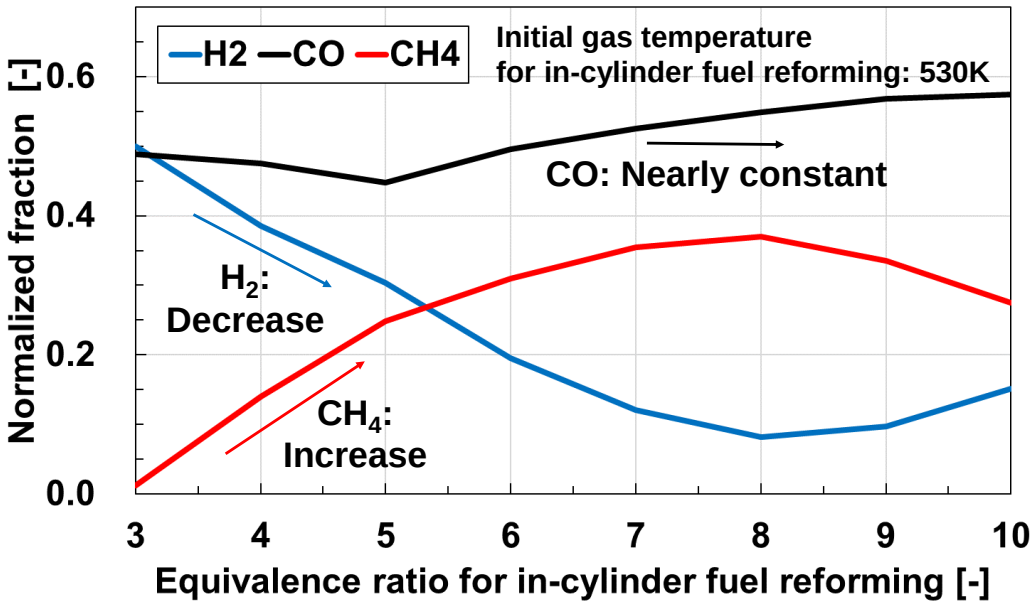

Figure 3-3: Normalized fractions of CO, H_2 and CH_4 plotted along equivalence ratios for in-cylinder fuel reforming at 530 K (the initial gas temperature for in-cylinder fuel reforming).

As mentioned earlier, the present study considers CO, H_2 and CH_4 as fuel components. To determine the fraction of each fuel component, a trend in the fractions of these three components presented in Fig. 3-1 is referred. The computed fractions of these components in the in-cylinder fuel reforming simulation at the initial temperature of 530 K, which is a practical operating temperature of the engine, are selected. The computed mole fractions of CO, H_2 and CH_4 at the initial reforming temperature of 530 K are extracted and normalized. The normalized fractions of CO, H_2 and CH_4 are then plotted against the equivalence ratios (Fig. 3-3). According to Fig. 3-3, the H_2 fraction is replaced with the CH_4 fraction at similar proportion, although the CO mole fraction keeps nearly constant (around 50%) over the almost entire equivalence ratios considered. The similar trend is also observed

for various initial gas temperatures. Consequently, simplified composition of test mixtures is determined based on the following manner: the CO fraction is constant (50%) and the H_2 fraction is replaced with the CH_4 fraction every 5%. The mole fractions of the mixtures are shown on Table 3-1. In the experiment, four conditions ($CO/H_2/CH_4$ = 50/50/0, 50/45/5, 50/25/25, 50/0/50) are examined (the shaded conditions on Table 3-1). Air is used as an oxidizer. The mixture flow velocity is set to 3 cm/s. All experiments are conducted at atmospheric pressure.

Table 3-1: Mole fractions of mixture components investigated in the present study. Shaded conditions indicate the mixtures considered in both experiments and computations. Non-shaded conditions are considered only in computations.

$CO/H_2/CH_4$	CO	H_2	CH_4	O_2	N_2
50/50/0	0.149	0.149	0.0000	0.149	0.554
50/45/5	0.135	0.121	0.014	0.155	0.576
50/40/10	0.123	0.098	0.025	0.160	0.595
50/35/15	0.113	0.079	0.034	0.164	0.610
50/30/20	0.105	0.063	0.042	0.167	0.624
50/25/25	0.097	0.049	0.049	0.170	0.635
50/20/30	0.091	0.036	0.055	0.173	0.645
50/15/35	0.086	0.026	0.060	0.175	0.654
50/10/40	0.081	0.016	0.065	0.177	0.661
50/5/45	0.076	0.008	0.069	0.179	0.668
50/0/50	0.072	0.000	0.072	0.181	0.674
Pressure [atm]	1.0				
Equivalence ratio	1.0				
Inlet flow velocity [cm/s]	3.0				

3.2.2 Numerical models

At low flow velocity where weak flames are observed, the flow in the reactor can be considered as a one-dimensional reactive diffusive flow without a boundary layer. Such a reactive flow condition can be simulated with a model for one-dimensional freely propagating premixed flame with an additional heat transfer term between the wall and gas in the energy equation (Eq. 3.1) [65]. The modified PREMIX code in ANSYS Chemkin-Pro v19.0 [93] is used for weak flame calculations throughout this dissertation.

$$\dot{M}\frac{dT}{dx} - \frac{1}{c_p}\frac{d}{dx}\left(\lambda A\frac{dT}{dx}\right) + \frac{A}{c_p}\sum_{k=1}^{K}\rho Y_k V_k c_{pk}\frac{dT}{dx} + \frac{A}{c_p}\sum_{k=1}^{K}\dot{\omega}_k h_k W_k - \frac{A}{c_p}\frac{4\lambda Nu}{d^2}(T_w - T) = 0 \qquad (3.1)$$

The computational domain is 10 cm long and an estimated wall temperature profile of 300–1300 K shown in Fig. 3-4 is used in the computation. A flame location in the computation is defined as the location of the peak of [CO]*[O] intensity based on the literature reporting that the chemiluminescence from various syngas mixtures is derived from CO_2^* yielded from CO + O + M = CO_2^* + M [94,95]. All mixture conditions on Table 3-1 are considered in the computation. Four detailed chemical reaction models are employed: USC mech ver. II [96], San Diego mechanism [97], AramcoMech3.0 [98], and HP-mech [99,100].

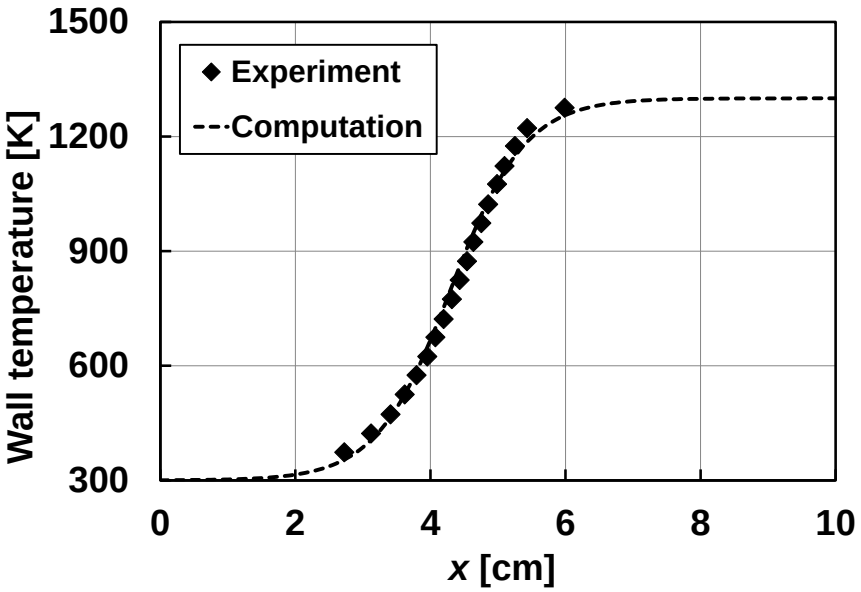

Figure 3-4: Measured wall temperature of the reactor and estimated wall temperature profile used in the computation.

In the present study, ignition delay times are also assessed in the computation as a different indicator of mixture reactivity. The computation is conducted using a zero-dimensional homogeneous reactor model in the AURORA package of ANSYS Chemkin-Pro v19 [93]. The mixture conditions (i.e., mixture composition, pressure) are the same as the MFR computations. HP-mech is used as a chemical reaction model for the computation.

3.3 Results and discussion

3.3.1 Weak flames of stoichiometric H_2/CO/CH_4 mixtures

Observed weak flame images of four CO/H_2/CH_4 mixtures are presented in Fig. 3-5. The flame location shifts greatly to the higher temperature region of the reactor as the H_2 fraction decreases and the CH_4 fraction increases, which indicates that the reactivity of the mixture decreases along the variation in the mixture composition. The difference in the wall

temperature at a flame location is approximately 246 K between the cases of $CO/H_2/CH_4$ = 50/50/0 and 50/0/50. According to an earlier study considering the research octane number (RON) effects on weak flame locations in MFR [70], the difference in the wall temperatures is approximately 40 K between RON = 0 and 100. Considering the fact, it must be emphasized that the variation in the reactivity investigated in the present study is extremely large. Moreover, the shift in flame locations seems greater in the cases with the small CH_4 fractions (CH_4 = 0% and 5%, ΔT = 83 K) compared to the cases of the larger CH_4 fractions (CH_4 = 25% and 50%, ΔT = 62 K).

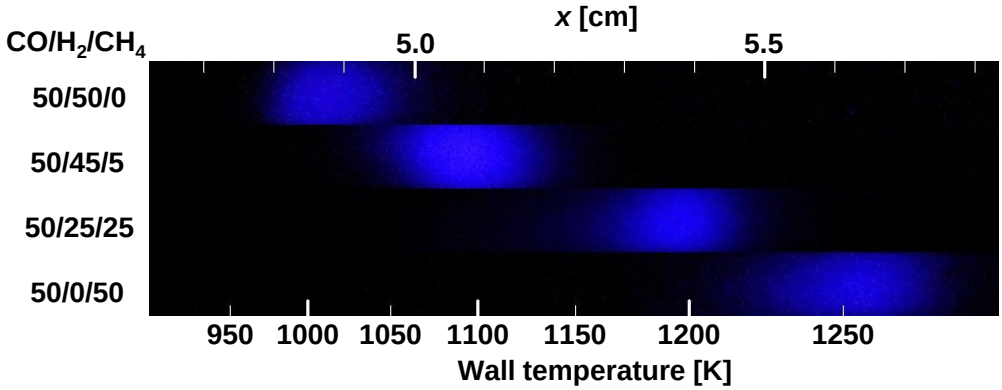

Figure 3-5: Weak flame images of $CO/H_2/CH_4$ = 50/50/0, 50/45/5, 50/25/25, and 50/0/50 obtained in the experiment.

Figure 3-6 shows the comparison of weak flame locations between the experimental measurements and computational predictions. The uncertainty of temperatures at a weak flame location is usually less than 5 K. In the computational results, the weak flame location shifts considerably to the higher temperature region as the H_2 fraction decreases and the CH_4

fraction increases. This trend is consistent with the experimental results. A larger shift of the flame locations is also observed in the computation for the cases with the small CH_4 fractions. Although the experimental and computational weak flame locations show qualitative agreement for all conditions considered, weak flames in the computation still tend to locate in the upstream side compared to the experimental flame locations. A further investigation must be conducted to assess the quantitative difference. Among four chemical reaction models used in this study, HP-mech showed the best agreement with the experimental weak flame locations over the mixture composition considered. Hence, further chemical reaction analyses have been conducted based on results from HP-mech.

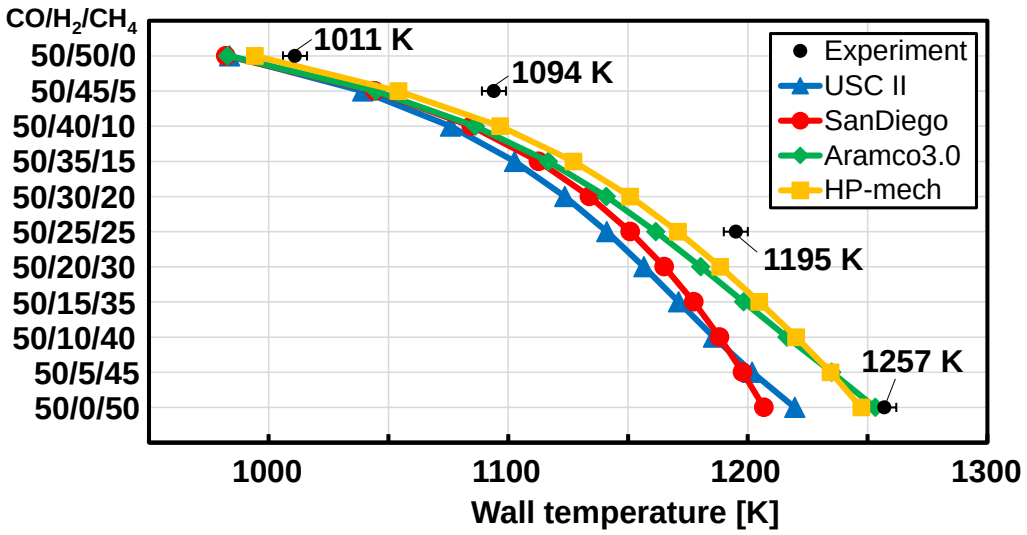

Figure 3-6: Comparison of weak flame locations of the stoichiometric $CO/H_2/CH_4$ mixtures between the experimental measurements (Black points) and the computational predictions (Colored lines). The uncertainty of the wall temperatures at a flame location is less than 5 K.

To show the correlation between the mixture reactivity indicated by weak flames and ignition delay times, the computed ignition delay times of stoichiometric $CO/H_2/CH_4$ mixtures are presented in Fig. 3-7. One apparent observation is that the ignition delay time increases as the H_2 fraction decreases and the CH_4 fraction increases over the entire temperature range considered. The trend is consistent with that indicated by the weak flames in the MFR experiment. It should be noted that the difference in the ignition delay times between $CO/H_2/CH_4$ = 50/50/0 and 50/0/50 is quite large (approx. a factor of 2000 at T = 1000 K). To experimentally measure ignition delay times with such a wide variation, both a shock tube and a rapid compression machine are required in general. Therefore, it is worth emphasizing that this study demonstrates the capability of weak flames in MFR to evaluate mixtures with widely various reactivities in a simple and well-defined configuration.

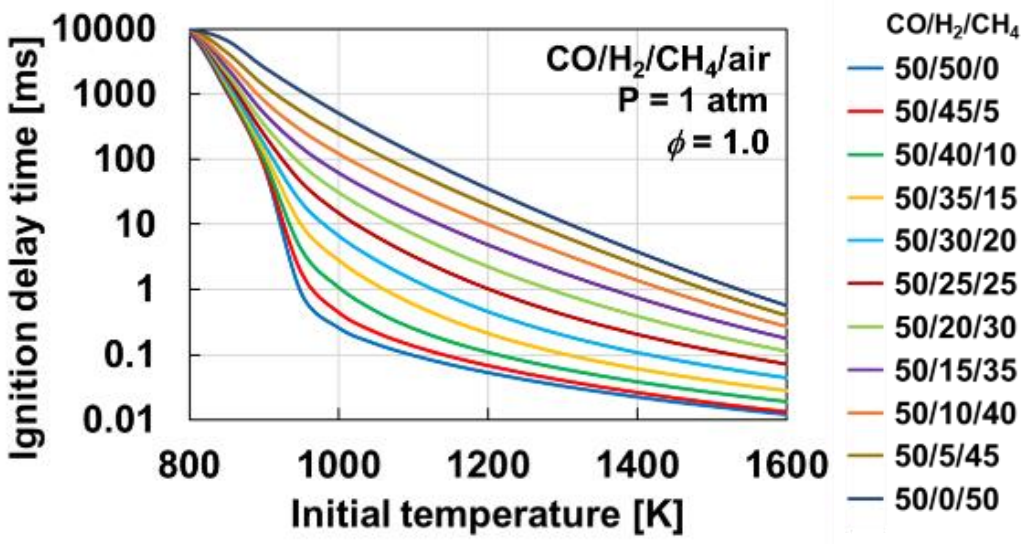

Figure 3-7: Computed ignition delay times of stoichiometric $CO/H_2/CH_4$/air mixtures at atmospheric pressure and initial temperatures of 800–1600 K by HP-mech.

Another observation can be made for the cases with large amounts of H_2 in the mixtures. In a low-temperature region (below 900 K), the ignition delay time is mostly similar regardless of mixture compositions. However, once the temperature increases to over 900 K, the ignition delay time decreases rapidly for the cases of $CO/H_2/CH_4$ = 50/50/0, 50/45/5, and 50/40/10. This behavior is attributable to the shift in the dominant reaction pathways of the H_2–O_2 system [101]. Under low temperature conditions, the oxidation of H_2 is governed by H + O_2 (+M) = HO_2 (+M). HO_2 radicals produce H_2O_2 through H_2 + HO_2 = H_2O_2 + H. Finally, OH radicals are produced by the decomposition of H_2O_2. Under high temperature conditions, OH radicals are produced mainly through H + O_2 = O + OH. This change in dominant reactions is apparent in the second explosion limit of the H_2–O_2 system [102,103]. The same trend was identified in an earlier study for weak flames of CO/H_2 mixtures with MFR, in which the effects of inert mixtures ([M]) on the syngas reactivity was investigated [81]. As the CH_4 fraction increases, the trend disappears because the dominant reactions are suppressed by reactions involving CH_4 and CH_4-related species.

3.3.2 Chemical reaction analysis

In general, ignition phenomena proceed with exponential increases of radicals. Especially, OH radicals are a crucially important species for fuel oxidation. Therefore, rate-of-production (ROP) analysis for the OH consumption is conducted to investigate the effects of the mixture

composition on the variation in the reactivity of the $CO/H_2/CH_4$ mixtures. Figure 3-8 presents the results of the ROP of OH radicals by fuel components computed with HP-mech. In the case of $CO/H_2/CH_4$ = 50/50/0, OH radicals are consumed mainly by H_2 and CO through R4: $H_2 + OH = H + H_2O$ and R30: $CO + OH = H + CO_2$. However, once CH_4 is included as a fuel component ($CO/H_2/CH_4$ = 50/45/5, 50/25/25, 50/0/50), CH_4 starts consuming OH radicals through R174: $CH_4 + OH = CH_3 + H_2O$ and competes with CO and H_2 for OH radicals. Here is an important difference in the products from these reactions. Through R4 and R30, H_2 and CO consume OH radicals and produce H radicals as a product, while CH_4 consumes OH radicals through R174 and produces CH_3 radicals. As mentioned in the previous section, H radicals lead to a chain-branching reaction and play an important role in the OH radical formation. Subsequently, produced OH radicals promote further destruction of fuels. In contrast, CH_3 radicals are less reactive compared to H radicals. Since the rate of CH_3 radical production increases and the rate of H radical production decreases as the CH_4 fraction increases, the OH formation from H radicals can be suppressed. This inhibition of radical pool growth by CH_4 results in the large decrease in the reactivity of the $CO/H_2/CH_4$ mixtures. Although the recombination reaction of a CH_3 radical and a H radical, $CH_3 + H (+M) = CH_4 (+M)$, can also have a great impact on the reactivity of the mixtures as reported in past studies [28,88], additional diagnostics have to be made to reason these effects in the MFR system. Thus, the competition of OH radicals by CO, H_2, and CH_4 and the larger production of CH_3 radicals appear to be the primary factor in the large decrease in the reactivity.

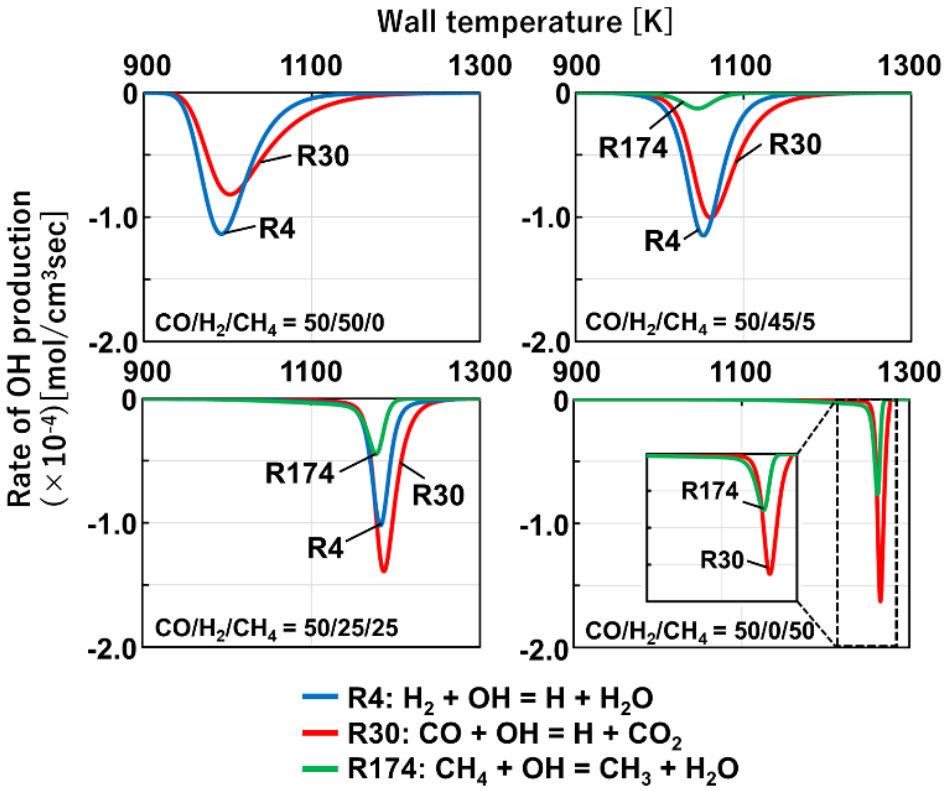

Figure 3-8: Rates of OH production for the cases of $CO/H_2/CH_4$ = 50/50/0, 50/45/5, 50/25/25, and 50/0/50. Negative values denote species consumption.

3.4 Conclusions

The reactivity of stoichiometric $CO/H_2/CH_4$/air mixtures at various composition was investigated based on weak flame responses in MFR. Both experimental and computational results showed that weak flame locations of $CO/H_2/CH_4$ mixtures shifted greatly to the higher temperature region as the H_2 fraction decreases and the CH_4 fraction increases, which indicates the reactivity of the $CO/H_2/CH_4$/air mixtures decreases considerably. Computed ignition delay times of $CO/H_2/CH_4$ mixtures at atmospheric pressure also indicated that the reactivity of those mixtures decreases greatly as CH_4 fraction increases. According to the rate-of-production analysis for OH radicals, it was demonstrated that OH radicals are consumed

mainly by fuel components, CO, H_2, and CH_4 for all mixture cases. For the CO/H_2 mixtures, OH radicals are mainly consumed by CO and H_2. Subsequently, H radicals are produced through R4: $H_2 + OH = H + H_2O$ and R30: $CO + OH = H + CO_2$. However, once CH_4 is included in the CO/H_2 mixtures, CH_4 starts consuming OH radicals through R174: $CH_4 + OH = CH_3 + H_2O$ and produces CH_3 radicals, which are less reactive species. The consumption rate of OH radicals by CH_4 become larger as the CH_4 fraction increases. This suppresses the OH formation from H radicals. Therefore, the primary factor for the significant decrease in the reactivity of the CO/H_2/CH_4 mixtures seems to be the increase of the OH consumption by CH_4 and the CH_3 radical production due to the increase of the CH_4 fraction.

Appendix

3.A 0-D adiabatic engine simulation

To estimate reformate gas composition from the fuel reforming in an engine cylinder, a 0-D adiabatic engine simulation is conducted using the multi-zone homogeneous charge compression-ignition model in AURORA package of Chemkin-Pro v19.0 [93]. This computation simulates an engine cycle from the intake valve close (IVC) to the exhaust valve open (EVO). In the present study, *n*-tridecane ($C_{13}H_{28}$) is selected as a target fuel, and its mixture with air is considered. The specification of the engine configuration for the computation is shown in Table 3A-1.

Table 3A-1: Specifications of the fuel reforming engine.

Compression ratio [-]	18.0
Clearance volume [cm^3]	89.908
Stroke ratio [-]	3.271
Rotation speed [rpm]	1800
Crank angle (IVC/EVO) [°]	-140/125

Computations are conducted within a range of crank angle from -140 to 125 degrees, which corresponds to the period from IVC to EVO. Composition of reformate products at the crank angle of 125 degrees is investigated. Initial pressure is set to 1.115 atm. Equivalence ratios and initial gas temperatures are varied from ϕ = 1 to 10 and from T_i = 320 K to 1000 K, respectively. To investigate fundamentals of in-cylinder fuel reforming, the initial temperature is extended up to 1000 K, which is an unrealistic value as a practical engine operation (e.g.,

550 K at maximum). The LLNL model for C_8–C_{16} n-Alkanes [11] is employed as the chemical kinetic model for the computation.

Figure 3A-1 presents the mole fractions of major components at EVO. The mole fractions of CO and H_2 are maximum at $\phi \approx 3$ and above $T_i \approx 500$ K, and then decrease with the increase of the equivalence ratio. The CO mole fraction is almost constant above $\phi \approx 5$ and $T_i \approx 500$ K while the H_2 mole fraction further decreases with the increase of the equivalence ratio. The CO_2 and H_2O mole fractions are large at near stoichiometry. H_2O mole fraction also increases at $\phi \approx 5$–10 and above $T_i \approx 450$ K. CH_4 and C_2H_4 are not produced below $\phi \approx 4$ while their mole fractions largely increase above $\phi \approx 5$ and $T_i \approx 500$ K. C_2H_2 is also formed at high equivalence ratio-high initial gas temperature region. However, the region of C_2H_2 production is much narrower and the amount is much smaller than those of CH_4 and C_2H_4. C_2H_6 is hardly produced for equivalence ratio-initial temperature conditions considered. These results indicate that CO and H_2 are mainly produced from $\phi \approx 2$ to 5 above $T_i \approx 500$ K, while the productions of small hydrocarbons such as CH_4 and C_2H_4 become larger above $\phi \approx 5$ and $T_i \approx 500$ K. Figure 3A-2 shows the maximum in-cylinder temperatures plotted on the equivalence ratio-initial temperature plane.

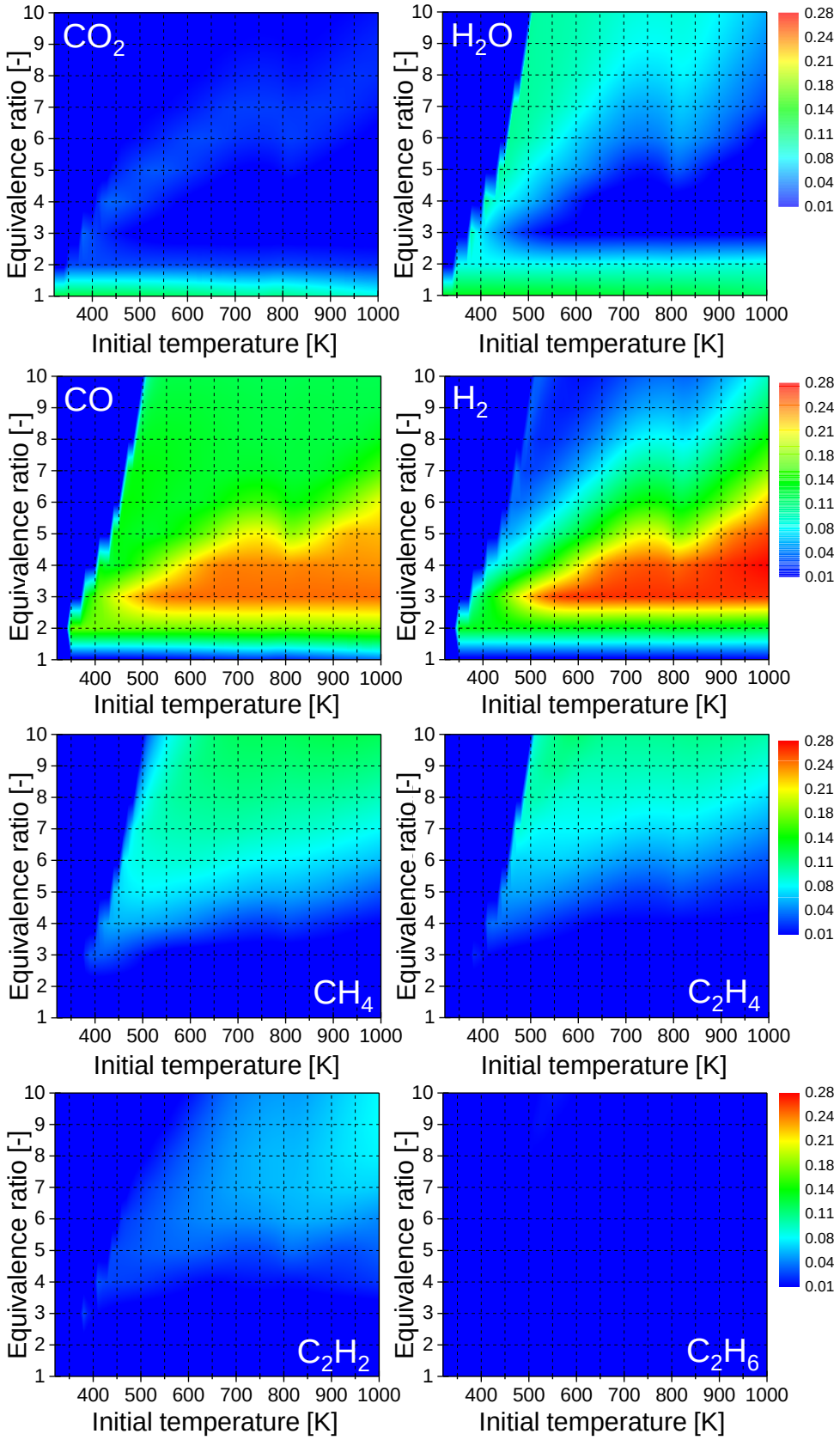

Figure 3A-1: Computed mole fractions of major reformate gas components produced from in-cylinder fuel reforming of *n*-tridecane/air mixtures.

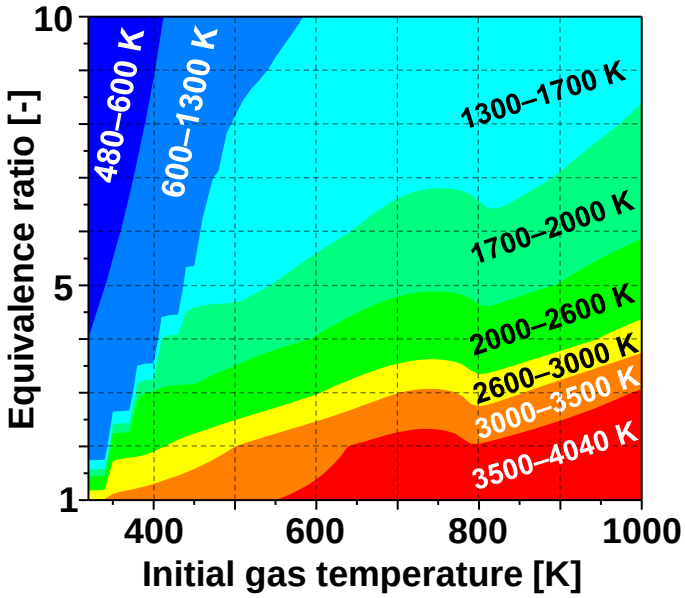

Figure 3A-2: Computed maximum gas temperatures during the fuel reforming process in an engine cylinder.

In Fig. 3A-2, the maximum gas temperatures are below 1700 K in the high equivalence ratio region (approximately higher than 7) at all the initial temperatures. At low initial temperatures around 500 K, the region where the maximum in-cylinder temperatures are below 1700 K is also seen at equivalence ratios between $\phi = 5$ and $\phi = 7$. According to the ϕ–T map introduced by Kamimoto and Bae [20], the production of soot is extremely small below 1700 K at any equivalence ratios considered in this work. Thus, no soot formation would be observed in such temperatures. Since the present computations are conducted under an adiabatic condition for simplicity, an actual range of equivalence ratio and initial temperature to attain low maximum in-cylinder temperatures is expected to be wider compared to the results of the present computations. In fact, engine experiments with n-heptane ($\phi = 2$ to 5 and T_i = 400 K to 500K) showed no soot formation [80].

Chapter 4 :
Effects of mixture composition on oxidation and reactivity of DME/NH_3/air mixtures

4.1 Introduction

As introduced in Chapter 1, blending NH_3 with more reactive fuels potentially expand possibility of its practical use in existing combustion applications. However, the oxidation and reactivity of hydrocarbon–NH_3 mixtures have not been investigated well. Especially, information regarding chemical interaction between hydrocarbons and NH_3 at low-to-intermediate temperatures is still scarce. In this work, fuel oxidation and reactivity are evaluated for widely various fuel blending ratios and equivalence ratios. To pay special attention to chemical interaction between hydrocarbons and NH_3 at low-to-intermediate temperatures, dimethyl ether (DME) is chosen as a base fuel. DME is a promising carbon-neutral fuel which is producible from renewable energy sources, and it is easy to handle in gas phase. An important aspect of DME is that it exhibits multi-stage oxidation, as do gasoline and diesel components. With DME, related information of oxidation and reactivity of larger hydrocarbon/NH_3 mixtures can be obtained.

The present chapter investigates effects of mixture composition and equivalence ratios on the oxidation and reactivity of DME/NH_3 mixtures based on weak flame responses in MFR. To realize a smooth transition into a carbon-free society, gradual replacement of hydrocarbon

fuels with NH_3 is one key direction. Therefore, conditions with large and small fractions of hydrocarbon and NH_3 are considered. Specifically, NH_3 fractions in DME/NH_3 fuel blends are varied for 0–50% and three equivalence ratios (ϕ = 0.5, 1.0 and 1.2) are examined. A combined chemical reaction model for DME/NH_3 mixtures is has been developed. Then chemical reaction analyses based on experimental information and numerical simulation are conducted, particularly addressing chemical interactions between hydrocarbons and NH_3-related species.

4.2 Experiment and Computation

4.2.1 Experiment setup

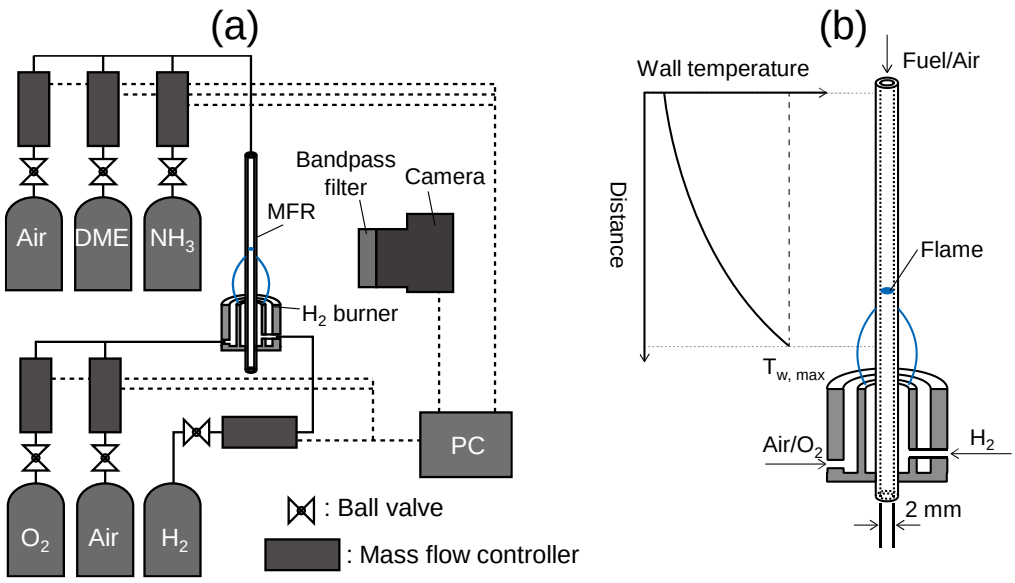

Figure 4-1: (a) Overview of the MFR experiment setup. (b) Schematic of the MFR structure.

For this study, a horizontal type of MFR is employed to obtain higher spatial resolution of weak flames. Schematics showing the experiment setup and the inner structure of MFR are

presented in Fig. 4-1. A quartz tube is placed vertically, passing through the center of a H_2/air burner. A stationary temperature profile with a maximum temperature of 1300 K is produced along the reactor wall by the surrounding burner flame. The inner wall temperature of the reactor is measured by inserting a K-type thermocouple from the bottom side of the reactor. An averaged temperature value obtained over a 2-min temperature history at each location in the reactor are used to estimate the wall temperature profile shown in Fig. 4-2. The uncertainty of the wall temperature at a hot flame location is ±5 K. The reactor inner diameter and the test section length are, respectively, 2 mm and 15 cm. All experiments are conducted at atmospheric pressure. As the base fuel, DME was selected as base fuels because it is a promising bio-fuel candidate, because it is easy to handle in the gas phase, and because it exhibits low temperature oxidation. In DME/NH_3 mixtures, the NH_3 fraction in fuel blends is varied between 0% and 50%. Air is used as the oxidizer. Three different equivalence ratios of ϕ = 0.5, 1.0, and 1.2 are considered. The inlet mixture flow velocity is set to 2 cm/s for the DME/NH_3 = 100/0 blend. Those for other DME/NH_3 blends are adjusted to keep combustion enthalpy input constant among same equivalence ratios. Mixture conditions are presented in Table 4-1. The respective flow rates of DME, NH_3, and air are controlled independently by mass flow controllers (MFC). The uncertainty of the flow rate of each gas flow is less than 1%. That of the equivalence ratio is less than 2%. Only stainless steel tubes with inert-treated surfaces are used for piping materials because NH_3 corrodes copper materials, and because the absorption of NH_3 on stainless steels is reported in an earlier report [104]. Each

experiment is conducted after keeping a mixture flowing in the reactor until a weak flame is stabilized at a certain location in MFR (at least 30 min after a mixture starts flowing into the reactor). Chemiluminescence of weak flames is observed with using a digital camera (D810; Nikon Corp.) with a bandpass filter (431.4 nm transparent wavelength, 6.5 nm half band width) to reduce the noises of thermal radiation from the heated quartz tube. The exposure time is set to 2 min for each flame picture. The peaks of brightness profiles extracted from flame images are defined as hot flame locations. Brightness profiles are generated by calculating the averaged brightness values of flame images in radial direction.

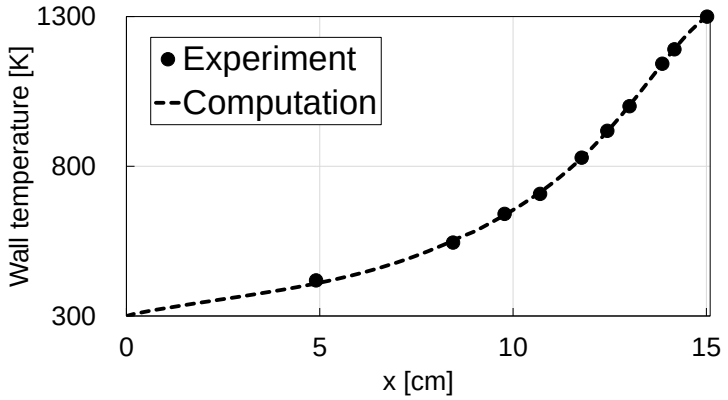

Figure 4-2: Measured wall temperatures and wall temperature profile used in the computation.

Table 4-1: Test mixture composition and inlet flow velocity for the experiment.

Equivalence ratio [-]	Compositions (DME/NH_3)	DME	NH_3	O_2	N_2	Inlet flow velocity [cm/s]	Combustion enthalpy flow rate [W]
$\phi = 0.5$	100/0	0.034	0.000	0.203	0.763	2.00	0.13
	85/15	0.032	0.006	0.202	0.760	2.01	
	75/25	0.031	0.010	0.201	0.757	2.02	
	50/50	0.027	0.027	0.199	0.748	2.05	
$\phi = 1.0$	100/0	0.065	0.000	0.196	0.738	2.00	0.24
	85/15	0.062	0.011	0.195	0.732	2.02	
	75/25	0.060	0.020	0.193	0.727	2.04	
	50/50	0.05	0.050	0.189	0.710	2.09	
$\phi = 1.2$	100/0	0.078	0.000	0.194	0.729	2.00	0.29
	85/15	0.074	0.013	0.192	0.722	2.03	
	75/25	0.070	0.023	0.190	0.716	2.05	
	50/50	0.059	0.059	0.185	0.696	2.13	

4.2.2 Conditions for computations

The reactive diffusive flow in MFR is modeled with the same modified PREMIX code in Chemkin-Pro [93] presented in Chapter 3. The wall temperature profile is estimated based on the measured temperatures (Fig. 4-2) and is used for the computation. The computational domain is 15 cm. Peak locations of the heat release rate (HRR) are regarded as an indicator of flame locations in the computation. Because DME exhibits multi-stage oxidation, three peaks appear in a computed HRR profile. Locations of the third HRR peak are regarded as locations of hot flames of DME/NH_3 mixtures for the comparison with the experimental flame locations.

A combined model of several reaction subsets is created for DME/NH_3 mixtures and is

used for the computation. As candidates for the DME reaction subset, the Zhao model [105], DME2000 [106,107], HP-mech [108], and skeletal Aramco 3.0 [98,109] are selected. As candidates for the NH_3 reaction subset, the Zhang model [110], the Mathieu model [104], the Glarborg model [111], the Nakamura model [112], and the Konnov [113] model are selected. Actually, HP-mech and the Nakamura model are chosen for the combined model because they showed the best reproducibility of the observed hot flame locations of the neat DME/air and neat NH_3/air mixtures. Model validation results are presented in Appendix 3B. For the hydrocarbon/NH_3 subset, the Glarborg model [114] is used to consider the interaction between C_1-C_2 species and N-related species. The combined reaction model comprises 234 species and 1685 reactions.

4.3 Results and discussion

4.3.1 Effects of mixture compositions on weak flame locations

Figures 4-3 presents the observed weak flame images of the stoichiometric DME/NH_3 mixtures and the brightness profiles extracted from the images. The brightness values are normalized by the maximum brightness intensity in each case for the easier comparison of flame locations. Chemiluminescence from hot flames is observed clearly for all DME/NH_3 mixtures at temperatures of 970–1170 K. Additionally, except for the case of the DME/NH_3 = 50/50 blend, indistinct chemiluminescence of blue flames is observed at 780–970 K. An interesting trend is found by that hot flames of the DME/NH_3 = 85/15 and 75/25 blends locate

in the lower temperature side more than that with DME/NH_3 = 100/0. As explained in Section 4.1, oxidation from CO to CO_2 occurs mainly in hot flames. Consequently, this trend in hot flame locations implies that the addition of small fractions of NH_3 promotes CO oxidation. As the NH_3 fraction in fuel blends is increased further from 15% to 50%, hot flame locations shift greatly to the higher temperature side, which indicates that the CO oxidation of the DME/NH_3 = 50/50 blend is completed at the higher temperature than that of other blends.

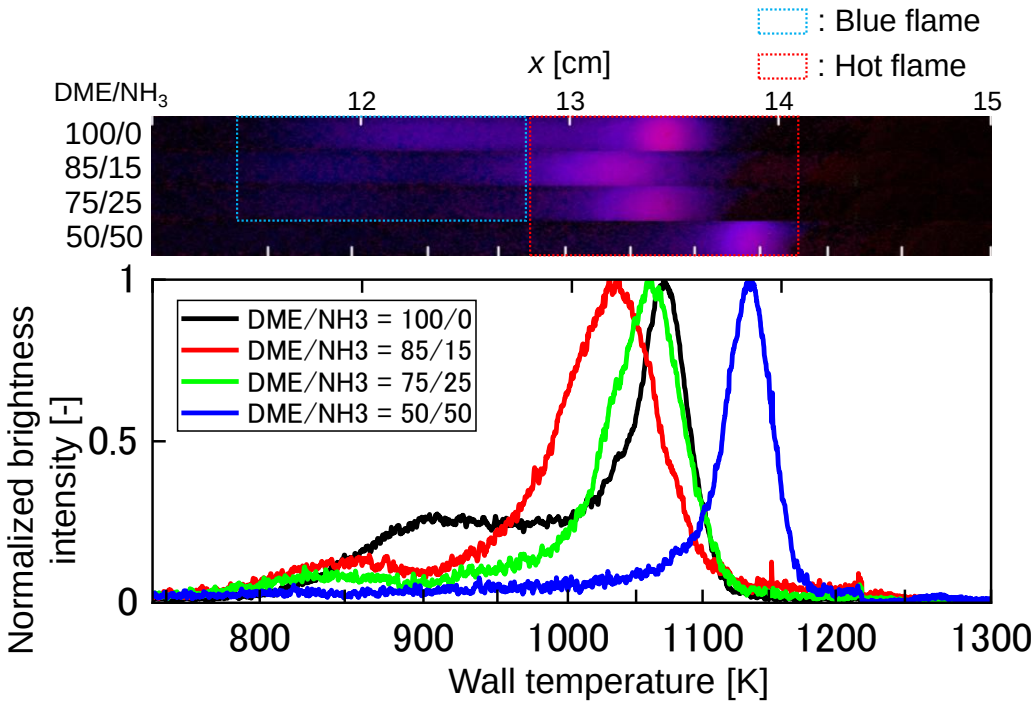

Figure 4-3: Observed weak flame images of stoichiometric DME/NH_3 mixtures and the brightness profiles extracted from the flame images. Chemiluminescence from flames are observed with a digital camera through a bandpass filter (transparent wavelength 431.4 nm, half band width 6.5 nm). The brightness values are normalized by the maximum brightness value in each case.

Figure 4-4 presents the comparison between experimentally and numerically obtained hot flame locations. The computational predictions well reproduce the observed hot flame locations. Especially the trend is predicted well that hot flames shift to the lower temperature side as the NH_3 fraction in the fuel blend is increased from 0% to 15%. The wall temperatures at flame locations in both experiments and computations are presented in Table 4-2. As the NH_3 fraction in fuel blends increases from 0% to 15%, hot flame locations shift to the lower temperature side by 41 K in the experiment and 11 K in the computation. However, as the NH_3 fraction in fuel increases from 15% to 50%, hot flame locations shift to the higher temperature side by 105 K in the experiment and 73 K in the computations. These results indicate the potential of NH_3 to alter the reactivity of DME considerably. In the following sections, the nature of NH_3 involvement in the oxidation of DME will be discussed using computational results and details obtained from chemical reaction analyses.

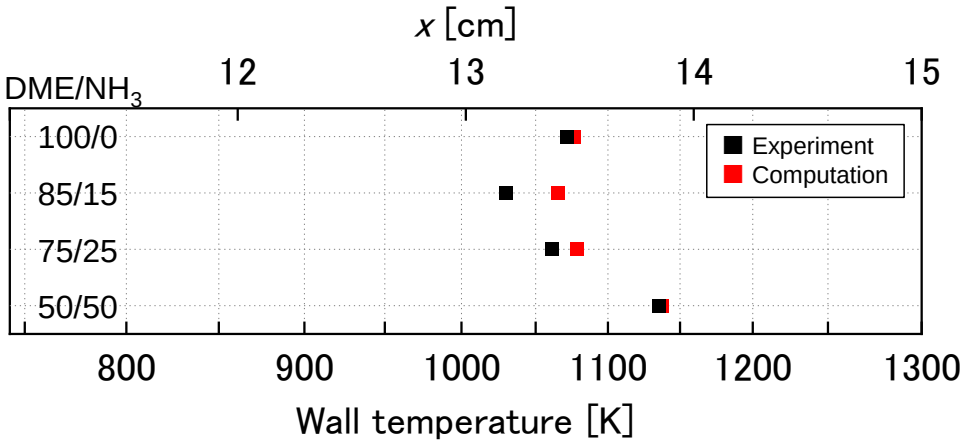

Figure 4-4: Comparison of hot flame locations observed in the experiment and computation.

Table 4-2: Wall temperatures at observed and computed hot flame locations.

DME/NH_3	Brightness peak location	Hot flame HRR peak location
100/0	1071 K	1076 K
85/15	1030 K	1065 K
75/25	1061 K	1078 K
50/50	1135 K	1138 K

4.3.2 Radical sensitization by NOx produced from NH_3 oxidation

Trends in hot flame locations of the DME/NH_3 mixtures reported in the preceding section suggest that CO oxidation is promoted when a small amount of NH_3 is blended with DME. This section presents a specific examination of how NH_3 can promote CO oxidation. Because OH radicals are the most crucially important species for fuel oxidation, rate-of-production (ROP) analyses are conducted for OH radicals. Figure 4-5 presents rates of OH radical consumption in the DME/NH_3 = 100/0 and 85/15 blends. Negative ROP values represent species consumption. The ROP values are stacked in these graphs. The size of each colored area represents the contribution of each reaction to the OH radical consumption. In both blends, three distinct reaction zones are observed: a cool flame zone at around 550–650 K, a blue flame zone at around 800–1000 K, and a hot flame zone at around 1050–1150 K. In the DME/NH_3 = 100/0 blend, OH radicals are consumed mainly by DME in the cool flame zone. In the blue flame zone, DME and CH_2O mainly consume OH radicals. It is noteworthy that some CO also consumes OH radicals in the blue flame zone.

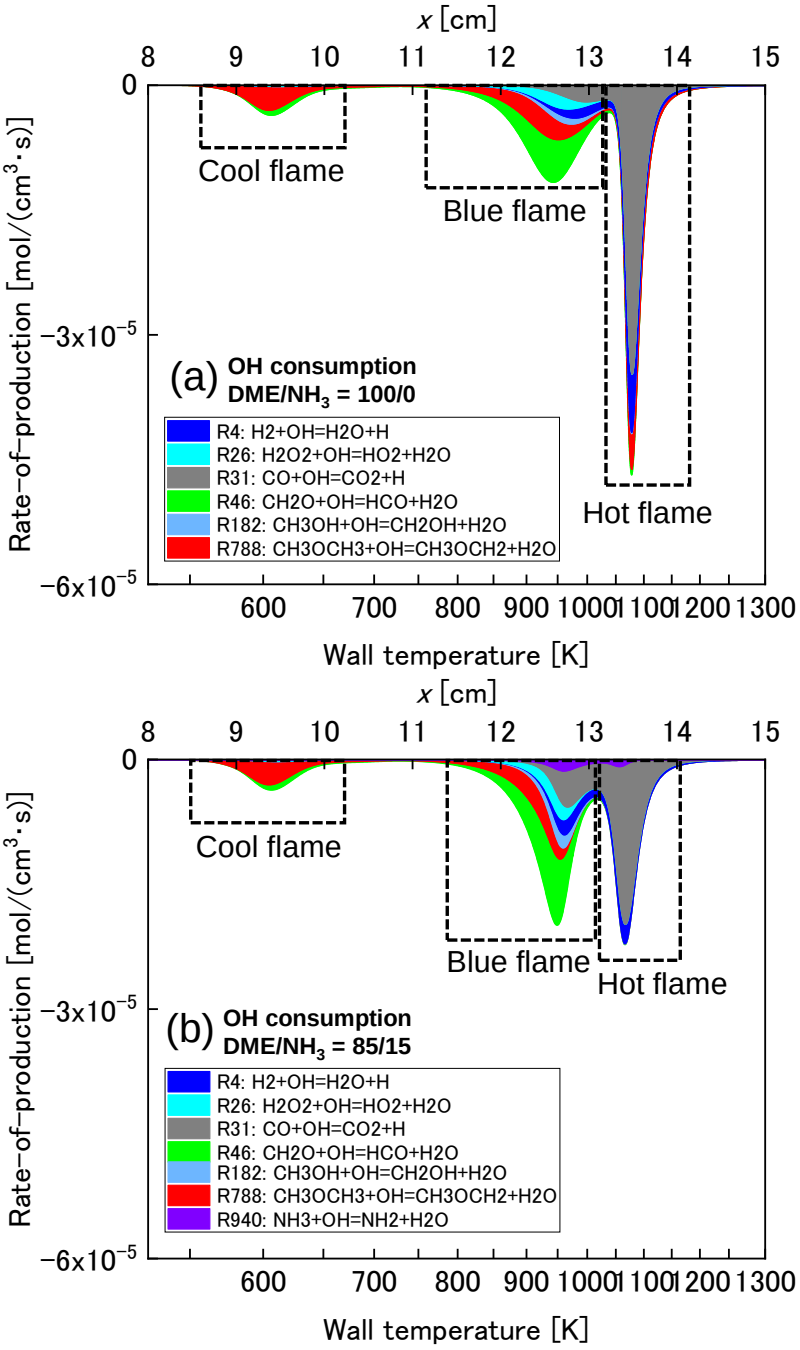

Figure 4-5: Rates of OH radical consumption in the DME/NH_3 = (a) 100/0 and (b) 85/15 blend. Negative rate-of-production (ROP) values represent consumption. The ROP values are stacked. Each colored area represents the contribution of each reaction.

In the hot flame zone, CO oxidation mainly proceeds. However, in the DME/NH_3 = 85/15 blend, NH_3 starts consuming OH radicals even in the blue flame zone, whereas NH_3 oxidation starts at over 1200 K in the neat NH_3-air case [76,112]. In the blue flame zone at around 800–

1000 K, NH_3 and CO start consuming OH radicals after DME and CH_2O consume OH radicals, which indicates that DME and CH_2O have higher priorities for OH radical consumption than NH_3 and CO. Compared to the DME/NH_3 = 100/0 blend, the overall OH radical consumption in the blue flame zone becomes more active for the DME/NH_3 = 85/15 blend. Especially, CO consumes more OH radicals in the blue flame zone, whereas the OH radical consumption by CO in the hot flame zone decrease greatly in the DME/NH_3 = 85/15 blend.

Additionally, the rates of OH radical production in the DME/NH_3 = 100/0 and 85/15 blends are presented by stacked areas in Fig. 4-6. In the DME/NH_3 = 100/0 blend, OH radicals are produced mainly through reactions with fuel radicals (R820: $CH_2OCH_2O_2H$ = OH + $2CH_2O$, R822: $O_2CH_2OCH_2O_2H$ = HO_2CH_2OCHO + OH and R823: HO_2CH_2OCHO = OCH_2OCHO + OH) in the cool flame zone. In the blue flame zone, the H_2O_2 decomposition (R22: H_2O_2 (+M) = 2OH (+M)) makes the greatest contribution to OH radical production. In the hot flame zone, the H_2–O_2 reaction system controls OH radical production [115]. By contrast, in the DME/NH_3 = 85/15 blend (Fig. 4-6b), the OH radical production in the blue flame zone is supported strongly by the reactions of NO and NO_2 (R971: NO + HO_2 = NO_2 + OH, R973: NO_2 + H = NO + OH) in addition to H_2O_2 decomposition (R22), whereas the OH production pathways in the cool/hot flame zone hardly change. The overall OH radical production in the blue flame zone also becomes larger with the DME/NH_3 = 85/15 blend than with the DME/NH_3 = 100/0 blend. Considering the starting point of the NH_3 oxidation in blue

flame zone (Fig. 4-5b) and the OH radical production through NO and NO_2 reactions (Fig. 4-6b), NO and NO_2 are products from the NH_3 oxidation in the blue flame zone. Note that NO in the blue flame zone is produced from the following sequences of NH_3 oxidation: $NH_3 \xrightarrow{+OH} NH_2 \xrightarrow{+NO_2} H_2NO \xrightarrow{+HO_2,+NO_2} HNO \xrightarrow{+O_2,+NO_2} NO$.

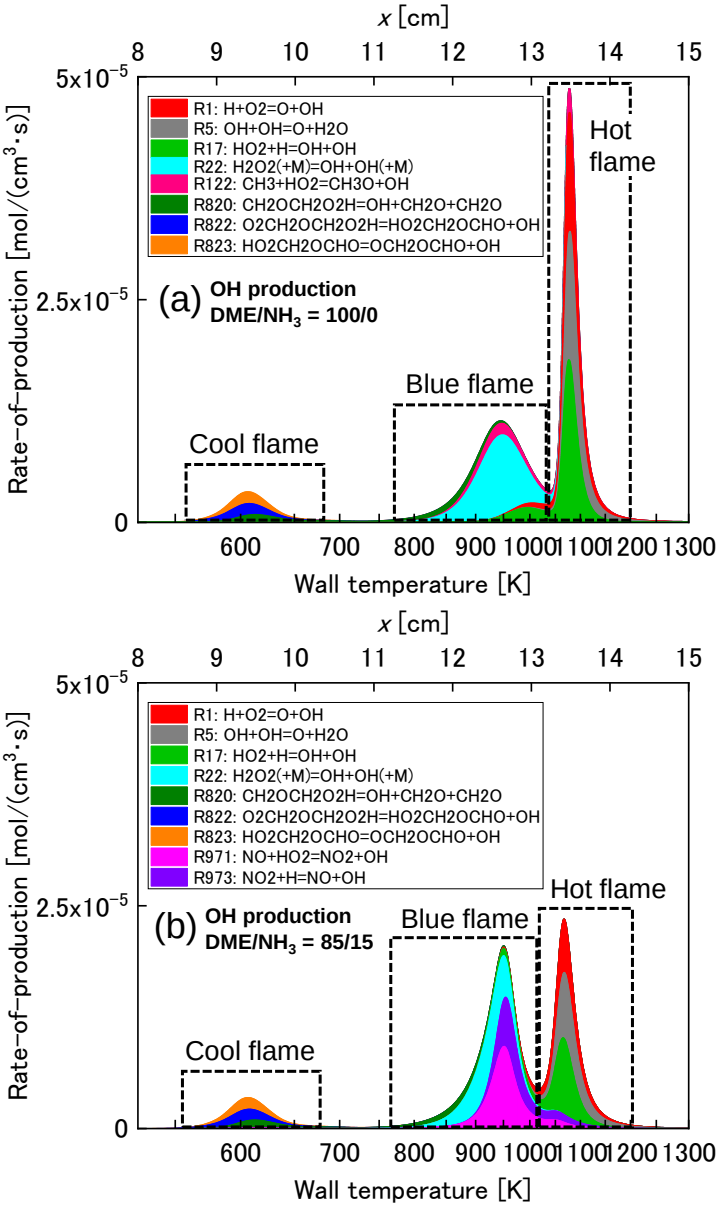

Figure 4-6: Rates of OH radical production in the DME/NH_3 = (a) 100/0 and (b) 85/15 blend. The ROP values are stacked. The size of each colored area represents the contribution of each reaction.

To investigate how NO is produced and consumed during fuel oxidation, ROP analyses are conducted for NO. The ROP of NO in the DME/NH_3 = 85/15 blend is presented in Fig. 4-7a. In the blue flame zone, the NO production proceeds through R973: NO_2 + H = NO + OH and R1219: CH_3 + NO_2 = CH_3O + NO. By contrast, NO is consumed mostly through R971: NO + HO_2 = NO_2 + OH. A schematic for these NO and NO_2 reactions is depicted in Fig. 4-7b. These reactions are known as the NO–NO_2 catalytic loop [33,43,47,116]. Its effects on the oxidation of various hydrocarbons have been investigated intensively over several decades [42,46,117–120]. It is designated as "catalytic loop" because NO and NO_2 convert less-reactive radical species such as HO_2 and CH_3 radicals into more-reactive species OH and CH_3O radicals (CH_3O radicals immediately decompose into CH_2O and H), whereas NO and NO_2 themselves are regenerated each other in the loop. Because of the nature of loop reactions, active radicals are produced effectively even with a small amount of NO (or NO_2), especially in the blue flame zone of 800–1000 K. Arunthanayothin et al. recently investigated effects of NH_3 additions on methane oxidation in jet-stirred reactor experiments [33]. They confirmed experimentally and numerically that, with 500 ppm NH_3 addition, the onset temperature of methane oxidation becomes lower than that in neat methane mixture cases. The trends also resulted from production of reactive species through the NO–NO_2 catalytic loop. This finding constitutes further evidence that the addition of small amounts of NH_3 enhances hydrocarbon mixture reactivity. In the present case, radical sensitization through NO–NO_2 catalytic loop accelerates fuel oxidation in the blue flame zone, which is the main

cause for the trend by which the hot flame of the DME/NH_3 = 85/15 blend shifts to the lower temperature side than that of the DME/NH_3 = 100/0 blend. With the nature of the separated reaction zones of weak flames in MFR and with the help of chemical reaction analyses, the MFR system specifies the temperature region in which the NO–NO_2 catalytic loop works actively.

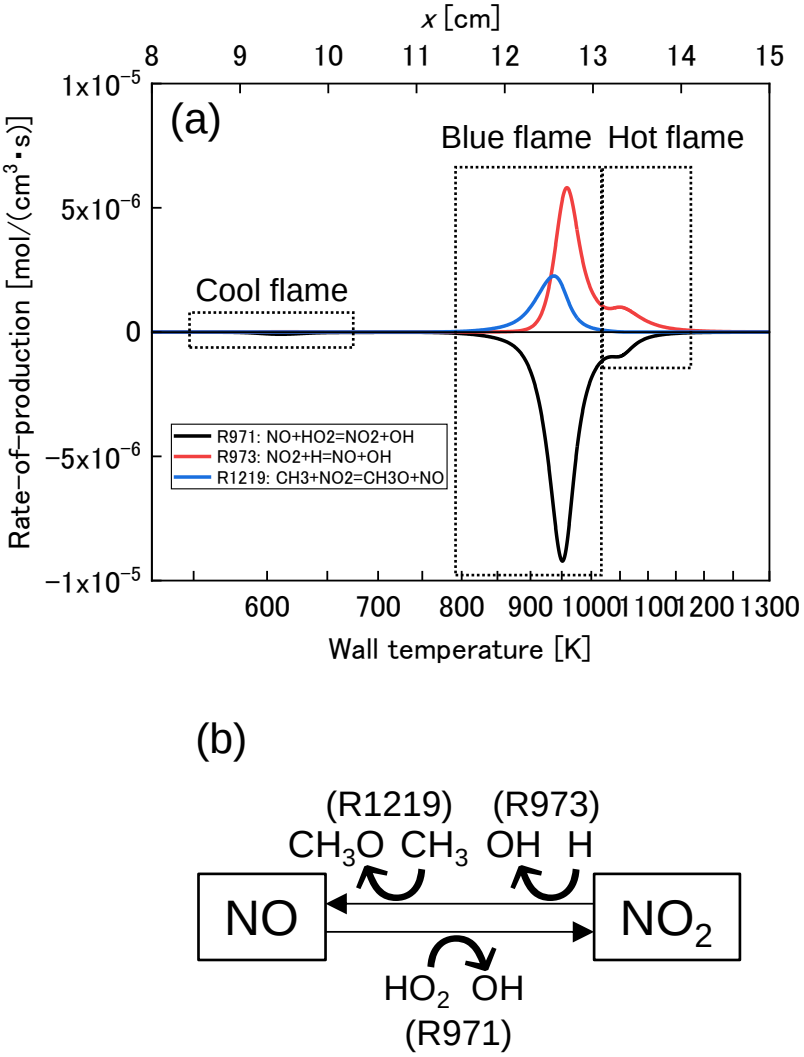

Figure 4-7: (a) Rate-of-production (ROP) of NO in the DME/NH_3 = 85/15 blend. Negative ROP values denote consumption. (b) Schematic of the NO–NO_2 catalytic loop reactions.

4.3.3 Inhibiting effects of NH_3 on CO oxidation

In both experimentally obtained results and computational predictions, hot flame locations shift to the higher temperature side as the NH_3 fraction in fuel blends increases further from 15% to 50%. The trend indicates that the DME/NH_3 mixture reactivity decreases as the NH_3 fraction in fuel blends increases further from 15%. This section specifically investigates the decrease in the mixture reactivity with the increase of the NH_3 fraction.

Similarly to the DME/NH_3 = 100/0 and 85/15 blends, ROP analyses are conducted for OH radicals for the DME/NH_3 = 75/25 and 50/50 blend (Fig. 4-8). The OH consumption by NH_3 increases greatly, especially in the blue flame zone, and that by CO decreases when the NH_3 fraction in fuel blend is increases from 25% to 50%. This indicates that the increase in NH_3 fractions greatly alters the reaction pathways for the OH radical production and consumption in the blue flame zone. Therefore, path flux analyses are conducted for OH radicals at the blue flame HRR peak locations.

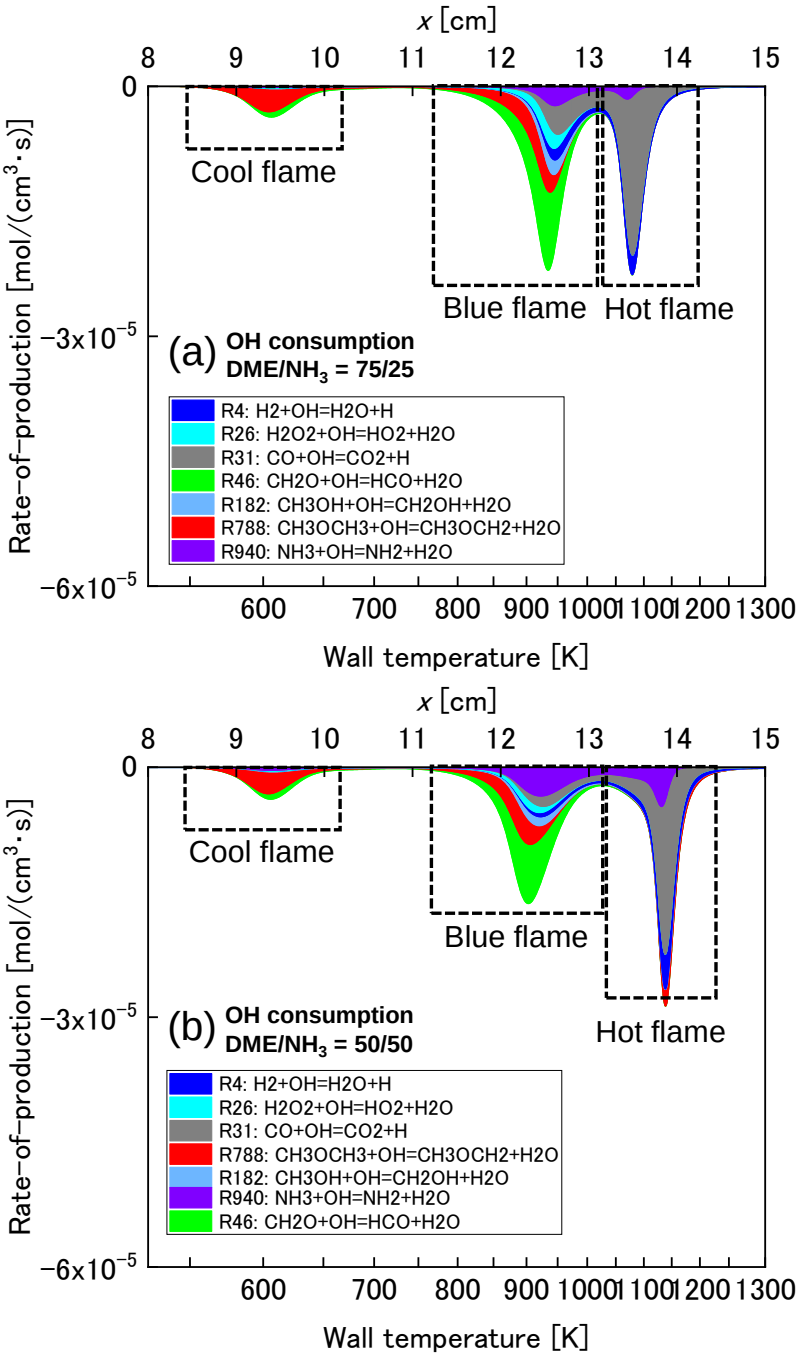

Figure 4-8: Rates of OH radical consumption in the DME/NH_3 = (a) 75/25 and (b) 50/50 blend. Negative ROP values denote consumption. The ROP values are stacked. The size of each colored area represents the contribution of each reaction.

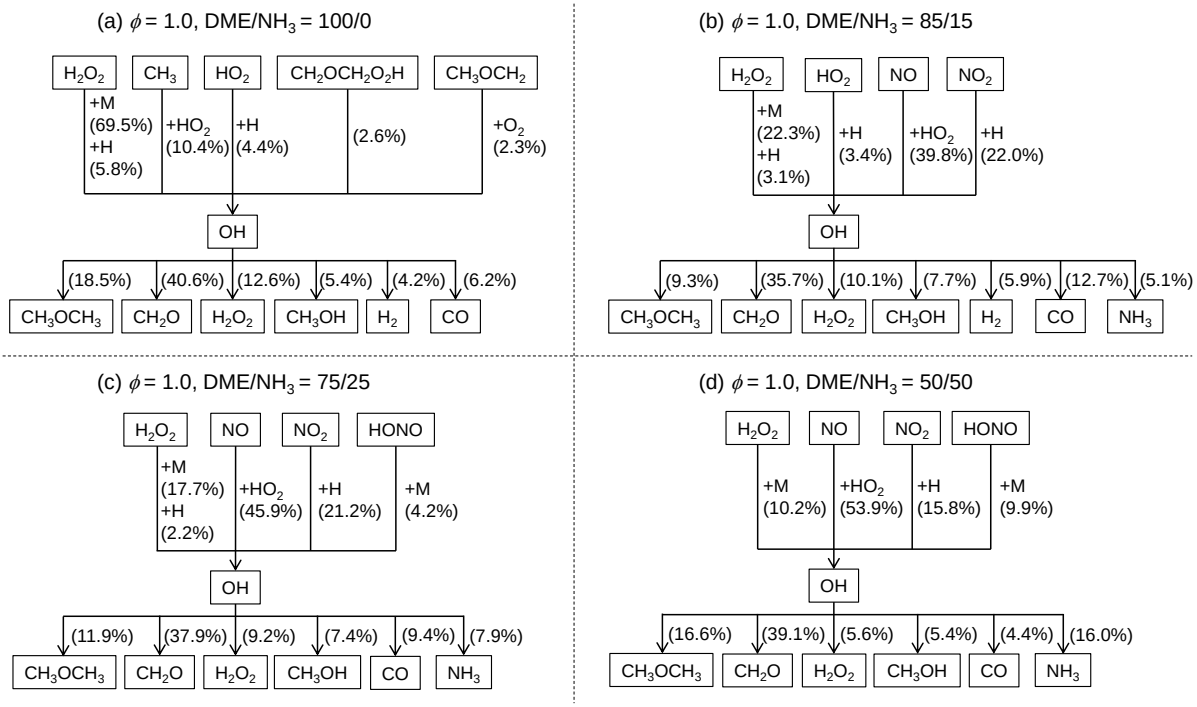

Figure 4-9: Path flux analyses for OH radicals at the blue flame HHR peak locations for the DME/NH_3 = (a) 100/0, (b) 85/15, (c) 75/25, and (d) 50/50 blends.

Figure 4-9 presents results of path flux analyses for OH radicals at blue flame HRR peak locations for the stoichiometric DME/NH_3 mixtures. In each diagram, upper pathways show major reactions for the OH radical production. Lower pathways show major species for the OH radical consumption. In the DME/NH_3 = 100/0 blend, a large proportion of the OH radicals is produced through the H_2O_2 decomposition (R22: H_2O_2 (+M) = 2OH (+M)) and is consumed mainly by CH_2O, DME, and H_2O_2. Once NH_3 is blended with DME (Figs. 4-9b–4-9d), more than 60% of the OH radical production is supported by NO and NO_2 reactions (R971: NO + HO_2 = NO_2 + OH and R973: NO_2 + H = NO + OH). The contribution of the H_2O_2 decomposition becomes smaller as the NH_3 fraction increases. The HONO decomposition (R1088: HONO (+M) = NO + OH (+M)) also becomes important for production of OH radicals at higher NH_3 fractions. HONO is produced mainly through

R1083: $H_2NO + NO_2 = HONO + HNO$. As the NH_3 fraction increases, NO_2 also reacts with species derived from the NH_3 oxidation such as NH_2 and H_2NO. Consequently, the contribution for the OH radical production by R973: $NO_2 + H = NO + OH$ decreases and that by R1088: HONO (+M) = NO + OH (+M) increases. Nevertheless, these reactions (R973 and R1088) hardly increase OH radical production to any considerable degree.

Regarding the OH radical consumption, the contribution of CO to OH radical consumption becomes larger in the DME/NH_3 = 85/15 and 75/25 blends than in the DME/NH_3 = 100/0 and 50/50 blends. When the NH_3 fractions in fuel blends increase from 15% to 50%, the contribution of CO to the OH radical consumption becomes one-third, whereas those of NH_3 are tripled, which indicates that, as the NH_3 fractions in fuel blends increase, not only the OH production through the NO–NO_2 catalytic loop but the OH radical consumption by NH_3 becomes larger than that by CO in the blue flame zone. It is noteworthy that that the NO–NO_2 catalytic loop converts less-reactive radicals into more-reactive radicals. Nevertheless, the quantities of radicals do not increase considerably through the loop because these reactions are chain-propagating reactions. Although CH_3O radicals produced through R1219: $CH_3 + NO_2 = CH_3O + NO$ generate H radicals from their decompositions, H radicals are consumed mainly through R973: $NO_2 + H = NO + OH$ in the blue flame zone. Therefore, despite the active OH radical production through the NO–NO_2 catalytic loop, the contribution of NH_3 to the OH radical consumption increases and the CO oxidation is inhibited in the blue flame zone. Consequently, more CO is left in the downstream region of the blue flame zone.

The CO oxidation proceeds at much higher temperature for cases with the larger amount of NH_3, i.e., hot flame locations shift to the higher temperature side.

4.3.4 Equivalence ratio effects on DME/NH_3 mixtures oxidation

The observed and computed hot flame locations of DME/NH_3 mixtures at equivalence ratios of ϕ = 0.5, 1.0, and 1.2 are presented in Fig. 4-10. In the DME/NH_3 = 100/0 blends, the observed hot flame locations change only slightly, irrespective of equivalence ratios. However, in other DME/NH_3 blends, the observed hot flame locations shift to the higher temperatures as the equivalence ratio increases. As the NH_3 fractions in fuel blends increase, hot flames at richer equivalence ratios locate in the higher temperature side. The largest shift of hot flames between ϕ = 0.5 and ϕ = 1.2 is observed for the DME/NH_3 = 50/50 blend. The computed hot flame locations show good agreement with the observed hot flame locations for all mixture conditions considered. The trend is especially well reproduced that hot flames shift to the higher temperatures as the equivalence ratio increases when NH_3 is blended with DME.

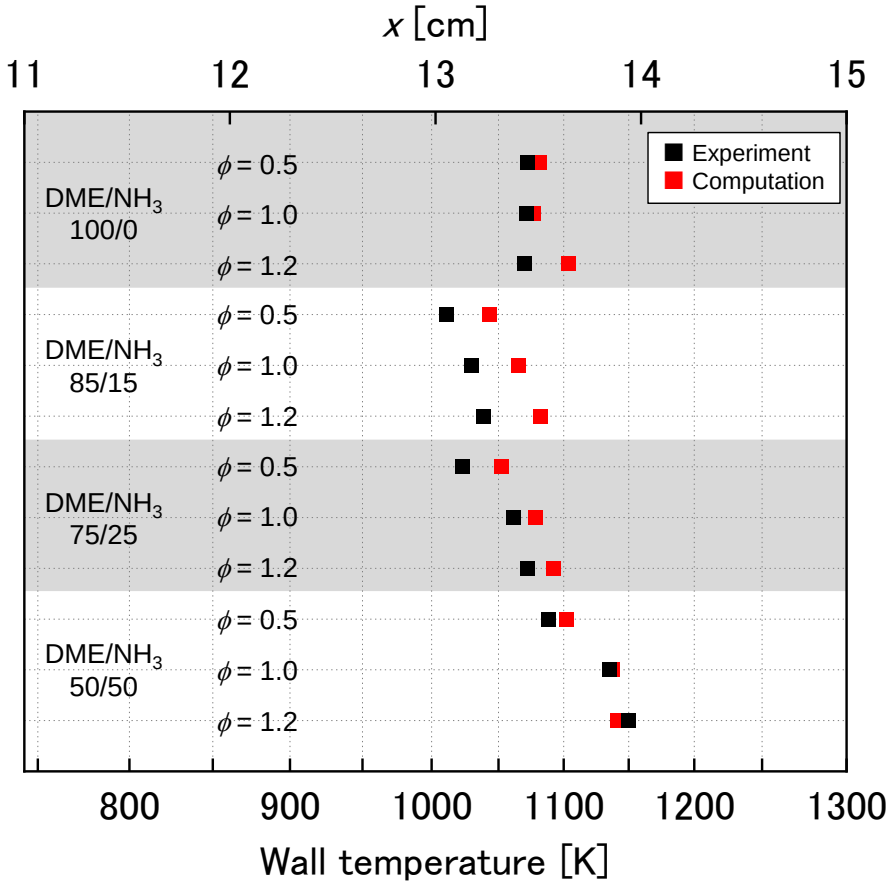

Figure 4-10: Brightness peak locations of observed weak flames (hot flames) and computed hot flame HRR peak locations of DME/NH_3 mixtures at the equivalence ratios of ϕ = 0.5, 1.0, and 1.2.

To investigate reasons why the hot flame locations shift to the higher temperatures for the same fuel blending ratio, ROP analyses for OH radical consumption are conducted. Since the difference in the observed hot flame locations between ϕ = 0.5 and 1.2 is the greatest for the DME/NH_3 = 50/50 blend, rates of OH radical consumption are investigated for the fuel blending ratios. Rates of OH radical consumption for the DME/NH_3 = 50/50 blend at ϕ = 0.5, 1.0, and 1.2 are presented in Fig. 4-11. When the equivalence ratio is increased from ϕ = 0.5 to ϕ = 1.0, the OH radical consumption becomes larger in both blue flame and hot flame zones. Also, the OH radical consumption by DME, CH_2O, and NH_3 becomes large, whereas

that by CO does not increase in the blue flame zone. In the hot flame zone, the OH consumption by CO increases for ϕ = 1.0. For the lean condition (ϕ = 0.5), R4: H_2 + OH = H_2O + H has smaller contribution to the OH radical consumption than R19: HO_2 + OH = H_2O + O_2 and other reactions. Therefore, R4 is not presented in Fig. 4-11a. For richer conditions (ϕ = 1.0 and 1.2), more H_2 is produced in the blue and hot flame zones, and the contribution of R4 to the OH radical consumption becomes much larger. Since the contribution of R19 becomes much smaller than that of other reactions, R19 is not presented in Figs. 4-11b and Fig. 4-11c.

When the equivalence ratio is further increased from ϕ = 1.0 to ϕ = 1.2, the contribution of CO to the OH radical consumption changes only slightly in the blue flame zone. However, the OH radical consumption by NH_3 and H_2 becomes larger than that by CO in both blue and hot flame zones. These trends indicate that CO has a lower priority for OH radical consumption than other species such as DME, CH_2O, NH_3, and H_2 because of the higher activation energy of CO. Therefore, because of the excess amounts of fuel and fuel-related species at richer equivalence ratios, more OH radicals are consumed by DME, CH_2O, NH_3, and H_2, but not by CO in the blue flame zone. Especially for ϕ = 1.2, the CO oxidation is inhibited because of excess amounts of NH_3 and H_2 even in the hot flame zone. Consequently, more CO is left for hot flames, which is why hot flames shift to the higher temperature side as the equivalence ratio increases only when NH_3 is blended with DME.

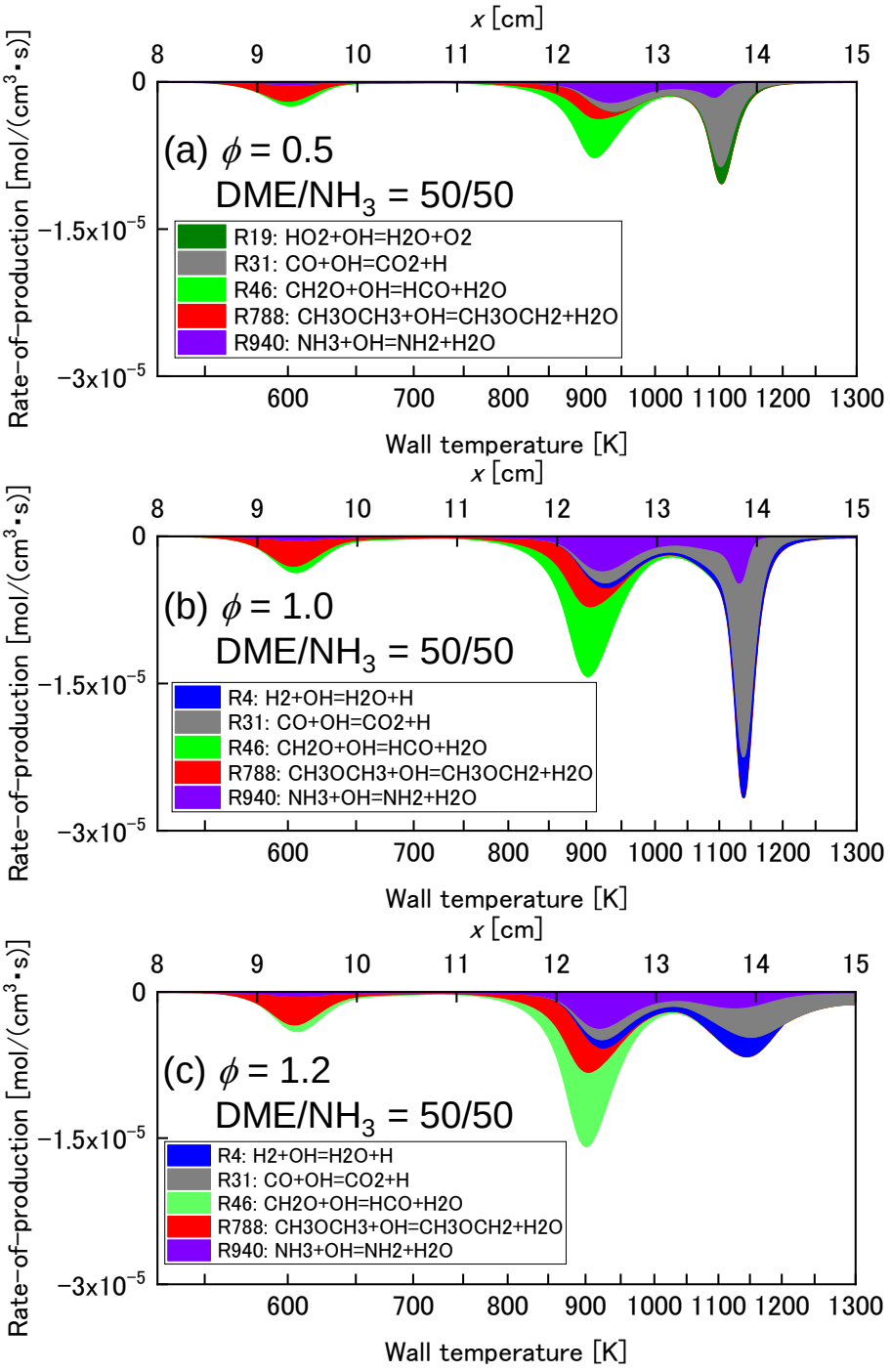

Figure 4-11: Rates of OH radical consumption in DME/NH_3 = 50/50 blends at the equivalence ratios of (a) ϕ = 0.5, (b) ϕ = 1.0, and (c) ϕ = 1.2. Negative ROP values denote consumption. The ROP values are stacked. The size of each colored area represents the contribution of each reaction.

4.4 Conclusions

In the present chapter, effects of mixture composition and equivalence ratios on oxidation and reactivity of the DME/NH_3 mixtures were examined based on weak flame responses in MFR. Results demonstrated that the observed hot flames shifted to the lower temperature side of the reactor when the NH_3 fraction in the fuel blend was increased from 0% to 15%, indicating that the addition of small amounts of NH_3 promotes the DME oxidation. As the NH_3 fraction increased further from 15% to 50%, hot flames shifted to the higher temperature side of the reactor. These trends in hot flame locations were also confirmed from computations simulating the MFR experiments.

Results of rate-of-production (ROP) analyses revealed that when NH_3 is blended with DME, NH_3 oxidation is triggered in the blue flame zone at around 800–1000 K, which yields NO and NO_2 as products. The produced NO and NO_2 start converting less-reactive radicals (HO_2→OH and CH_3→CH_3O) through the NO–NO_2 catalytic loop (R971: NO + HO_2 = NO_2 + OH, R973: NO_2 + H = NO + OH, R1219: NO_2 + CH_3 = NO + CH_3O). Radical sensitization through the NO–NO_2 catalytic loop promotes active radical production in the blue flame zone. Especially when the NH_3 fraction in the fuel blend is small, the CO oxidation proceeds more in the blue flame zone than in the hot flame zone, which is why the hot flame location shifts to the lower temperature side. However, when the NH_3 fraction in fuel blend increases further from 15% to 50%, NH_3 consumes more OH radicals in the blue flame zone instead of CO. Consequently, the CO oxidation in the blue flame zone is

inhibited, and is completed at higher temperatures, i.e., the hot flame shifts greatly to the higher temperature side.

When the equivalence ratio was varied, hot flame locations of the DME/NH_3 = 100/0 blends changed only slightly as the equivalence ratio increased. However, when NH_3 was blended with DME, hot flames shifted to the higher temperatures as the equivalence ratio increased. The ROP analyses showed that, because of the higher activation energy of the CO, OH radicals are mostly consumed by DME, CH_2O, NH_3, and H_2, but not by CO in the blue flame zone for richer equivalence ratios. When the equivalence ratio increased, the CO oxidation was inhibited even in the hot flame zone because excess amounts of NH_3 and H_2 consumed more OH radicals instead of CO. Therefore, the CO oxidation was inhibited. Consequently, hot flames shifted to the higher temperature side as the equivalence ratio increases when NH_3 is blended with DME.

Appendix

4.A Effects of surface reactions on flames in MFR

The quantitative understanding of effects of surface reactions or radical quenching on wall has advanced significantly in the last decade. In the case of methane, several researchers have reported that the estimated or measured sticking coefficients were two to four orders of magnitude smaller than the extensively used values [121]. Saiki et al. examined the effects of surface reactions on flames in a narrow channel with different wall materials using optical measurements, and reported that the initial sticking coefficients of alumina and quartz were estimated to 0 (inert) and 0.01 [122], respectively. Kizaki et al. examined that the effects of the tube diameters and pressure on species concentration and flame locations in MFR [123]. Computational predictions agreed well with measured species concentration for a quartz tube with inner diameter of 2 mm at atmospheric pressure when the initial sticking coefficient was set to 0.0005. No significant wall effects were observed at pressure above 0.05 atm.

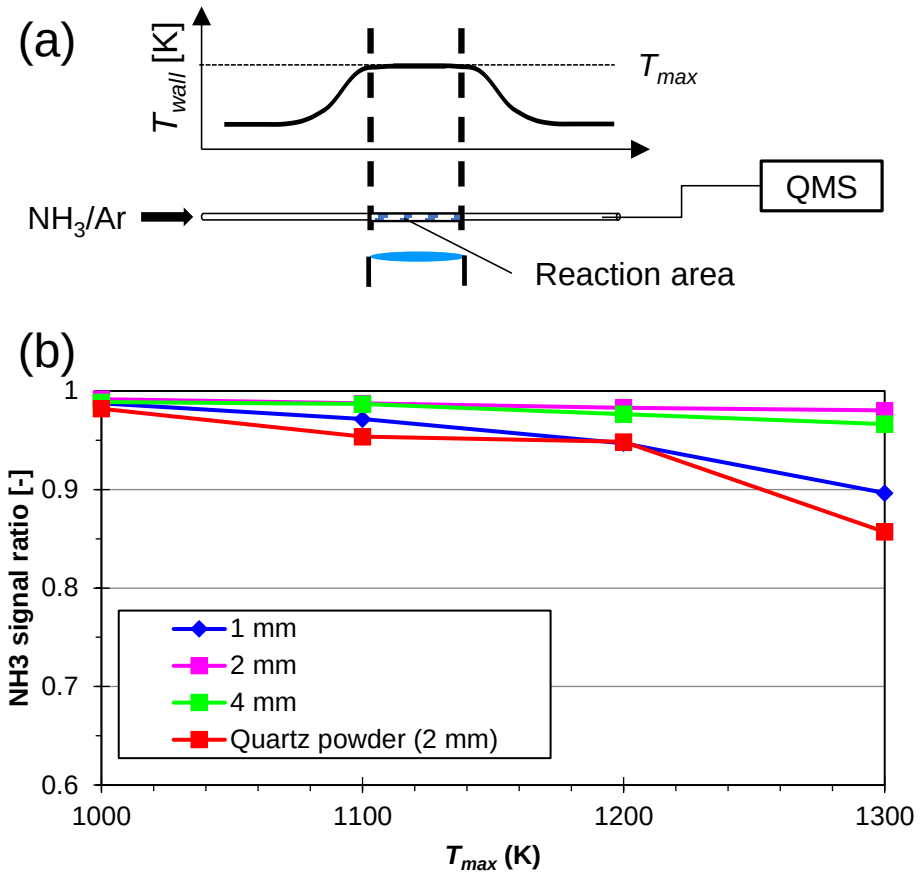

Figure 4A-1: (a) Schematic of the test setup. (b) Obtained NH_3 signal ratios (the ratio of NH_3 concentration at reactor exit to that at reactor inlet).

To investigate wall effects on flames in MFR for NH_3 cases, similar preliminary tests were conducted. The effects of the tube diameters on species concentration for weak flames in MFR were investigated. A schematic of the test setup is presented in Fig. 4A-1a. The experiment was conducted with heated quartz tubes with inner diameters of 1, 2, 4 mm, and a heated quart tube with inner diameter of 2 mm filled with quartz powder to maximize the surface-to-volume ratio of quartz. NH_3/Ar mixtures were introduced at inlet velocity of 10 cm/s. NH_3 concentration was measured by a quadrupole mass spectrometer (QMS) at the exit the reactor with the maximum wall temperatures of 1000, 1100, 1200 and 1300 K. A NH_3

signal ratio was defined as the ratio of NH_3 concentration at the reactor exit to that at the reactor inlet. Measured NH_3 signal ratios are presented in Fig. 4A-1b. The results indicate that no significant decrease of measured NH_3 concentration is observed for 2- and 4-mm cases whereas NH_3 concentration decreases by 10–15 % for the 1-mm and quartz powder cases. Therefore, the effects of surface reactions in MFR are negligible under the present experiment conditions However, it should be worthy to further investigate wall effects on flames of NH_3 mixtures in MFR under reduced pressure conditions.

4.B Model selection for individual reaction subsets

To select reaction subsets of DME and NH_3 for a combined chemical reaction model for DME/NH_3 fuel blends, model validation against weak flame (hot flame) locations in MFR and laminar burning velocity (S_L) are performed for neat DME/air and NH_3/air mixtures. Zhao model [105], DME2000 [106,107], HP-mech [108] and skeletal Aramco 3.0 [98,109] are selected as candidates for the DME reaction subset. Zhang [110], Mathieu [104], Glarborg [114], Nakamura [112] and Konnov [113] models are selected as candidates for the NH_3 reaction subset. For 1-D computations of weak flames for NH_3/air mixtures, the end of the computational domain is extended from 15 cm to 20 cm because no HRR peaks appear within 15 cm with some models. The wall temperature is kept at 1300 K for the extended domain. Also, S_L calculation is conducted by using the 1-D freely propagating flame model in Chemkin-Pro v.19.0. Mixture conditions are listed on Table 4B-1.

Table 4B-1: Mixture composition and inlet flow velocity of the mixtures.

Mixture	Equivalence ratio [-]	DME	NH_3	O_2	N_2	Inlet flow velocity [cm/s]
DME/air	1.0	0.065	0.000	0.196	0.738	2.00
NH_3/air	1.0	0.000	0.219	0.164	0.617	2.47

The brightness profile extracted from an observed weak flame image and the computed HRR profiles of the neat DME/air mixture are presented in Fig. 4B-1a. Hot flame locations indicated by locations of peaks of the computed HRR profiles by all reaction models show good agreement with the observed hot flame location. Especially, the predictions of weak flame locations by HP-mech and skeletal Aramco 3.0 are within the temperature range of ± 5 K from the observed weak flame location.

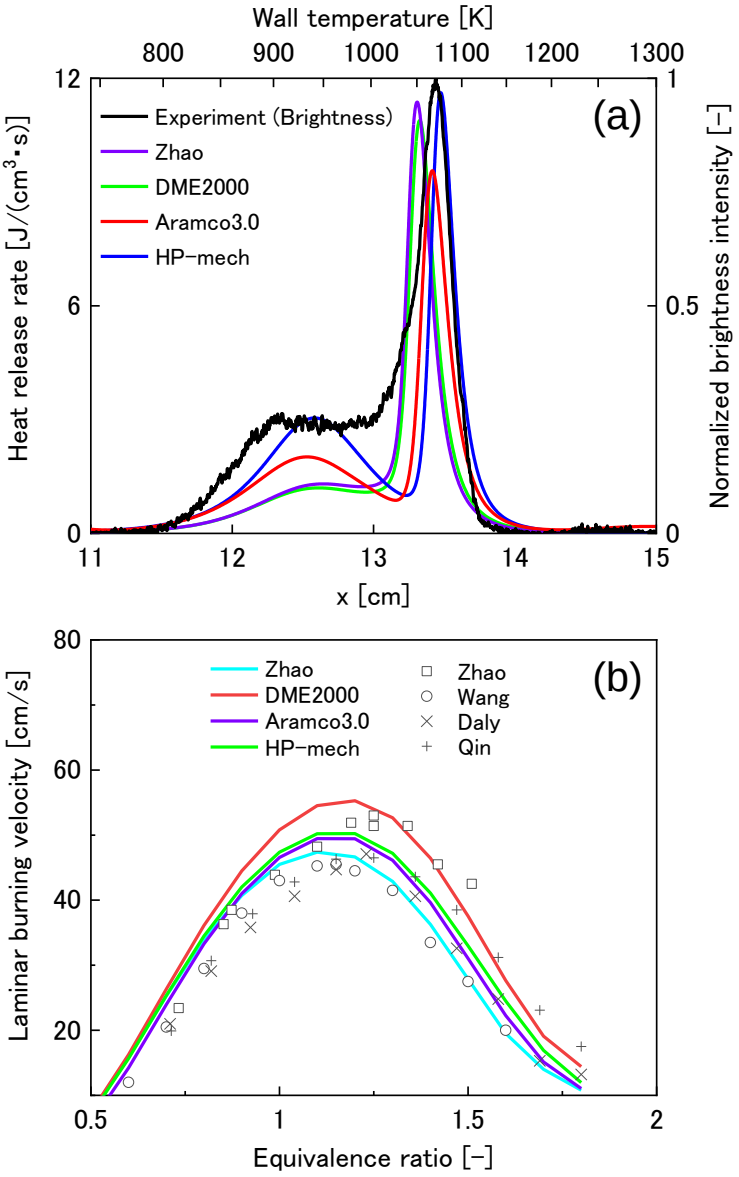

Figure 4B-1: (a) Observed and computed weak flame locations of the neat DME/air mixture. (b) Measured and computed laminar burning velocity of DME/air mixtures at atmospheric pressure and room temperature.

The measured and computed S_L of DME/air mixtures are presented in Fig. 4B-1b. The measured S_L are taken from earlier works by Zhao et al.[124], Wang et al.[125], Daly et al.[126], and Qin et al. [127]. All models slightly overpredict S_L on the lean side. DME2000 overpredict S_L for stoichiometric-to-slightly rich equivalence ratios. Predicted S_L values by HP-mech, Zhao model, and Aramco 3.0 are within the experimental scatters for richer

equivalence ratios. Considering the reproducibility of both weak flame locations and S_L of the DME/air mixture, HP-mech is chosen for the DME reaction subset.

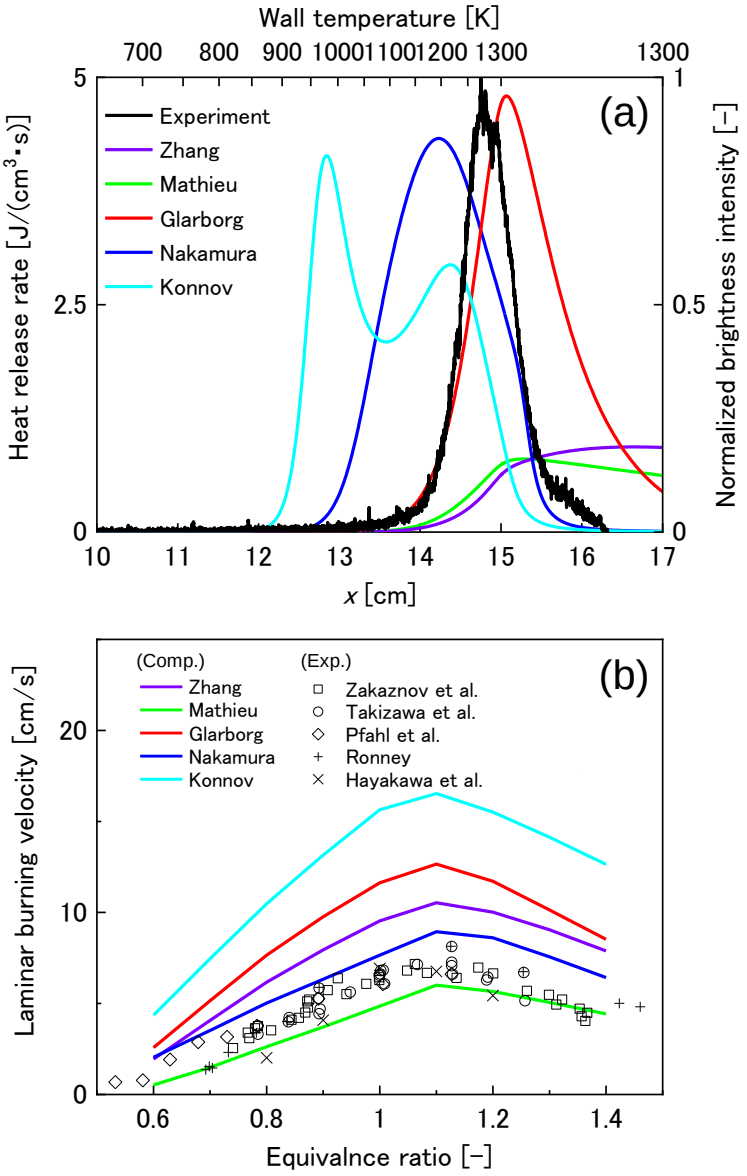

Figure 4B-2: (a) Observed and computed weak flame locations of stoichiometric NH_3/air mixtures. (b)Measured and computed laminar burning velocity of NH_3/air mixtures at atmospheric pressure and room temperature.

The brightness profile extracted from an observed weak flame image and the computed HRR profiles of the stoichiometric NH_3/air mixture are presented in Fig. 4B-2a. Single sharp

HRR peak appears in the predictions by Nakamura and Glarborg models. Double peaks appear in the result by Konnov model. No sharp peak is observed in the predictions by Mathieu and Zhang models.

The measured and computed S_L of NH_3/air mixtures are presented in Fig. 4B-2b. The measured S_L are taken from earlier works by Zakaznov et al.[128], Takizawa et al.[129], Pfahl et al.[130], Ronney [131], and Hayakawa et al. [132]. Nakamura model slightly overestimates S_L on the lean side. The discrepancy between the measured and computed S_L by Nakamura model becomes larger on the rich side. Mathieu model shows good reproducibility of the measured S_L on the rich side and slightly underestimates S_L on the lean-to-stoichiometry side. Zhang, Glarborg and Konnov models overpredict S_L for widely various equivalence ratios considered. Considering the reproducibility of both weak flame locations and S_L of NH_3/air mixtures, Nakamura model is chosen for the NH_3 reaction subset.

Chapter 5 :
Promoting and inhibiting effects of NO on CH_4 oxidation

5.1 Introduction

As also discussed in Chapter 1 and Chapter 3, nitric oxide (NO) has been widely known as one of major chemical species which has considerable effects on environment pollutions. On the other hand, NO exhibits promoting effects on oxidation of hydrocarbon fuels [120,133,134]. In terms of pollutant reduction and better efficiency of combustion applications, effects of NO addition on oxidation and reactivity of various types of fuels have been investigated intensively. In some practical applications such as ammonia/hydrocarbon combustion and reburning techniques, local NOx concentration near flames can be expected to be much higher. However, effects of high concentration of NO on oxidation and reactivity of hydrocarbons have not been examined widely. Therefore, the present chapter focuses on effects of NO on oxidation and reactivity of CH_4 for extended NO concentration in mixtures.

5.2 Experiment and Computation

A schematic of experimental setup is presented in Fig.5-1. For experiments, a vertical-type micro flow reactor (MFR) is employed also in this chapter to obtain higher spatial resolution of weak flames [65]. A quartz tube as a reactor passes through the center of a H_2–Air burner and a temperature profile with a maximum temperature of 1300 K is formed

on the reactor wall. The inner diameter of the quartz tube is 2 mm. The wall temperature profile is measured by inserting a K-type thermocouple from the bottom of the reactor. All the experiments are conducted at atmospheric pressure. The mole fractions of mixture components are presented in Table 5-1. The base mixture is composed of CH_4, O_2 and Ar. The mole fractions of CH_4 and O_2 are fixed. The increment of NO is balanced by reducing the Ar fractions. The equivalence ratio is calculated without considering the oxygen atom of NO. The NO concentration is varied in the range of 0.1–10% of the CH_4 concentration, which corresponds to 95-9480 ppm in total mixtures. CH_4, Ar and NO are stored in a steel tank with a pressure gauge by the partial pressure method. Flame observation is conducted with a digital camera (Nikon D810) with a bandpass filter (transparent wavelength 431.4 nm, half band width 6.5 nm) to reduce noises of the thermal radiation from the quartz tube. The exposure time is set to 3.5 minutes for each flame image.

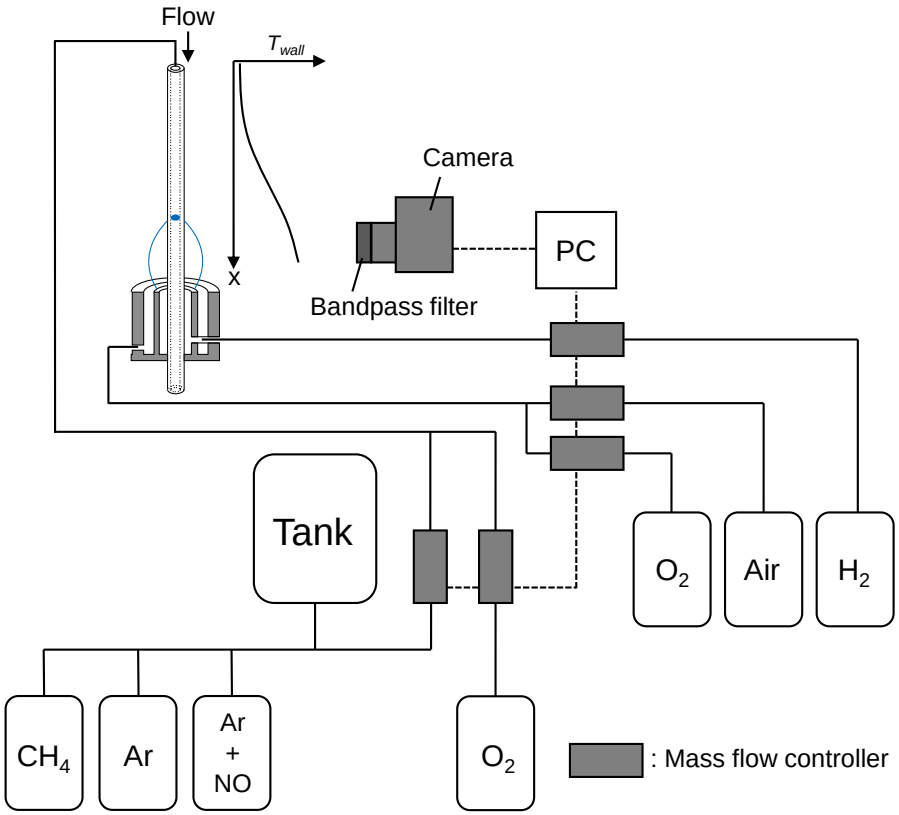

Figure 5-1: Schematic of the experimental setup.

Table 5-1: Mole fractions of test mixtures.

Mixture	CH_4	O_2	Ar	NO
Neat CH_4	0.0948	0.1896	0.7156	0 ppm
NO/CH_4 0.1%	0.0948	0.1896	0.7155	95 ppm
NO/CH_4 1%	0.0948	0.1896	0.7147	948 ppm
NO/CH_4 10%	0.0948	0.1896	0.7061	9480 ppm

The reactive flow in MFR is modeled with the same modified PREMIX code in Chemkin-Pro v19.0 [101] introduced in Chapter 3. For a chemical kinetic model, Song model (151 species and 2335 reactions) [43] is used. The wall temperature profile shown in Fig. 5-2 is used in the computation. A weak flame location in the computation is defined as the location of the peak of the heat release rate profile in each case.

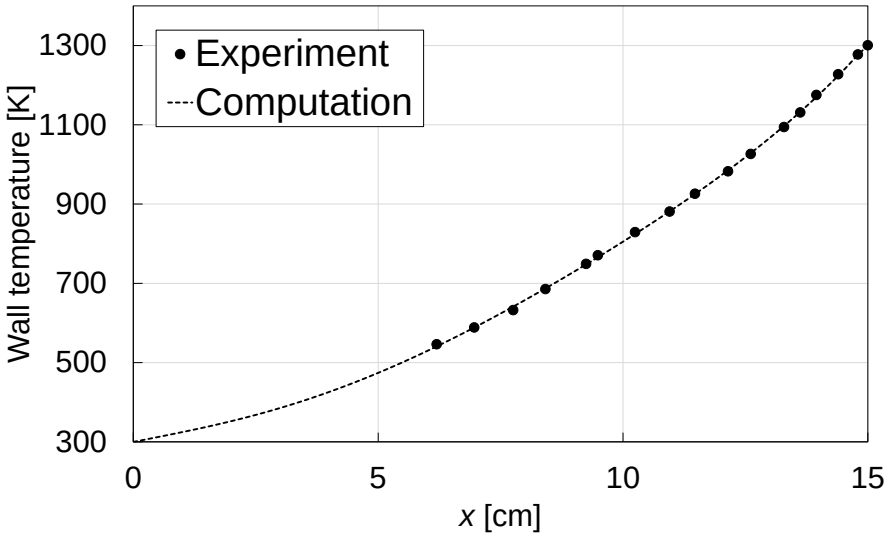

Figure 5-2: The measured wall temperatures and the estimated wall temperature profile used in the computation.

5.3 Results and Discussion

5.3.1 Effects of NO addition on CH_4/O_2/Ar weak flame locations

Figure 5-3a presents observed weak flame images of stoichiometric CH_4/O_2/Ar mixtures with/without NO addition. The observed weak flame of the NO/CH_4 0.1% case locates in a lower temperature region compared to the Neat CH_4 case, indicating NO addition enhances reactivity of the CH_4/O_2/Ar mixture. This trend becomes more obvious when the NO concentration further increases (NO/CH_4 1.0%). However, in the NO/CH_4 10% case, the flame location slightly shifts to the higher temperature side compared to the NO/CH_4 1.0% case. This implies that mixture reactivity is inhibited slightly at high NO concentration.

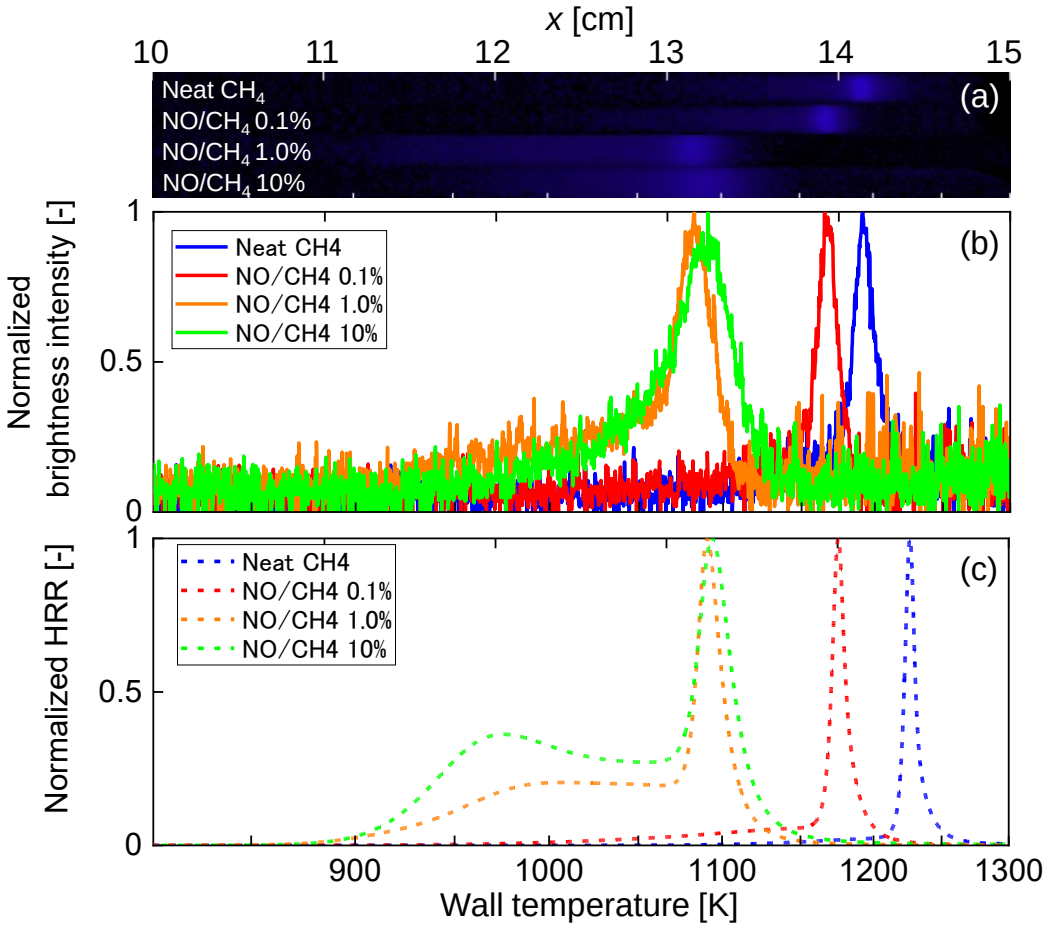

Figure 5-3: (a) Observed weak flame images of stoichiometric $CH_4/O_2/Ar$ mixtures with/without NO addition. (b) The normalized brightness intensity extracted from flame images. (c) The computed normalized heat release rate (HRR) profiles.

Figure 5-3b presents normalized brightness intensity extracted from weak flame images. As can be seen, the main flame zones become broader with higher NO concentration (NO/CH_4 1.0%, NO/CH_4 10%) compared to those with lower NO concentration (Neat CH_4 and NO/CH_4 0.1%). Figure 5-3c shows the normalized computed heat release rate (HRR) profiles for all test mixtures. There observed some quantitative differences in the wall temperatures at weak flame locations between the experiment and the computation. However, the computation qualitatively reproduces the overall trend in the experiment, that is, the weak flame location shifts greatly to the lower temperature side as the NO concentration increases

up to NO/CH_4 1.0%, and shift slightly to the higher temperature side as it further increases up to NO/CH_4 10%. This indicates that the reactivity indicated by the weak flame locations is the highest for the NO/CH_4 1.0% case, followed by the NO/CH_4 10%, NO/CH_4 0.1%, and Neat CH_4 cases. The following sections investigates how NO addition enhance/inhibits the reactivity of CH_4/O_2/Ar mixtures.

5.3.2 Radical sensitizing effects of NO on the reactivity of CH_4/O_2/Ar mixtures

To investigate how NO addition enhances the reactivity of CH_4/O_2/Ar mixtures, the rate-of-production (ROP) analyses are conducted. Figure 5-4 presents the rates of CH_4 consumption for the Neat CH_4 and NO/CH_4 1.0% cases. Negative ROP values denote speciesconsumption. It is obvious that CH_4 is consumed mostly by OH radical through R34: $CH_4 + OH = CH_3 + H_2O$ in both cases. However, the onset temperature of CH_4 oxidation is much lower and a large amount of CH_4 is consumed in the intermediate temperatures of 900–1050 K for the NO/CH_4 1.0% case.

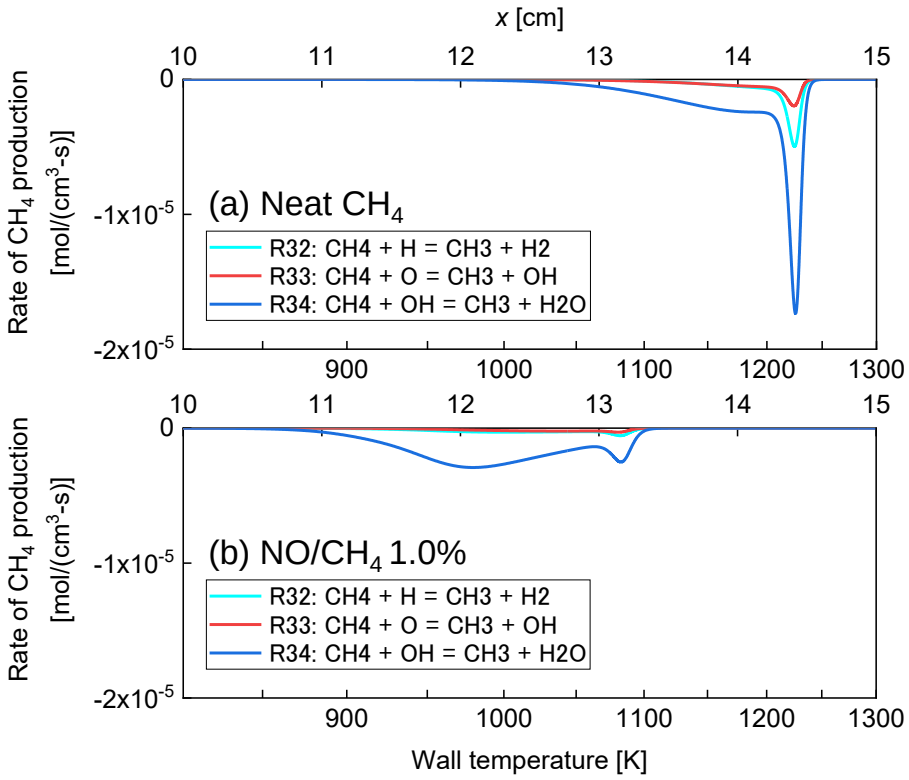

Figure 5-4: Rates of CH_4 radical consumption for (a) Neat CH_4 and (b) NO/CH_4 1.0%.

Figure 5-5 presents the rates of CH_3 radical consumption for the Neat CH_4 and NO/CH_4 1% cases. In the Neat CH_4 case, CH_3 radicals start being consumed at around 1050 K through R154: $CH_3 + CH_3 (+ M) = C_2H_6 (+ M)$ and R75: $CH_3 + HO_2 = CH_3O + OH$. In the higher temperatures above 1200 K, the contributions to CH_3 radical consumption by O, H and OH radicals (R31, R69 and R86) become larger. On the other hand, in the NO/CH_4 1.0% case, CH_3 radicals are consumed mostly in the intermediate temperatures of 900–1050 K through R2115: $CH_3 + NO_2 = CH_3O + NO$, and CH_3O radicals are produced. This indicates that NO_2 promotes CH_4 oxidation in the intermediate temperatures through converting less reactive species into more reactive species (i.e., $CH_3 \rightarrow CH_3O$). Since only NO is contained as an additive in the initial mixtures, NO_2 are expected to be produced from NO. Therefore, the

ROP of NO is investigated.

The rates of NO production/consumption for the NO/CH_4 1.0% and NO/CH_4 10% cases are presented in Fig. 5-6. In the NO/CH_4 1.0% case, NO is consumed mostly through the reaction with HO_2, R1929: NO + HO_2 = NO_2 + OH. This reaction also exhibits radical sensitization through converting HO_2 radicals into OH radicals. Subsequently, produced NO_2 is consumed through R2115: CH_3 + NO_2 = CH_3O + NO or R1969: NO_2 + H = NO + OH. Therefore, once NO is added to the CH_4/O_2/Ar mixtures, the OH radical production is enhanced through both R1929: NO + HO_2 = NO_2 + OH and R1969: NO_2 + H = NO + OH.

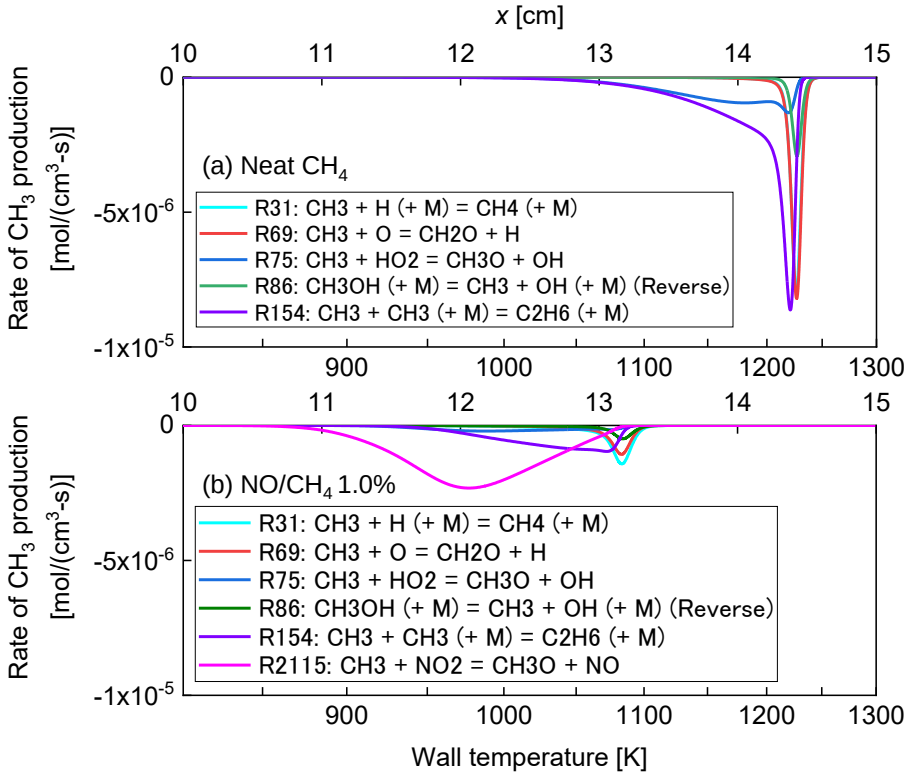

Figure 5-5: Rates of CH_3 radical consumption for (a) Neat CH_4 and (b) NO/CH_4 1.0%. Negative ROP values denote species consumption.

Consequently, the CH_4 oxidation is promoted from the intermediate temperatures. Moreover, CH_3 radicals are less reactive species and cannot be oxidized until temperature becomes sufficiently high for the Neat CH_4 case. However, in the presence of NO, CH_3 radicals can be converted into CH_3O radicals through R2115: $CH_3 + NO_2 = CH_3O + NO$. CH_3O radicals decompose easily into CH_2O and H radicals. CH_2O also reacts with OH radicals and produces HCO radicals, which eventually produce CO. As such, the oxidation of CH_4 further proceeds from intermediate temperatures with the help of the reactions of NO and NO_2.

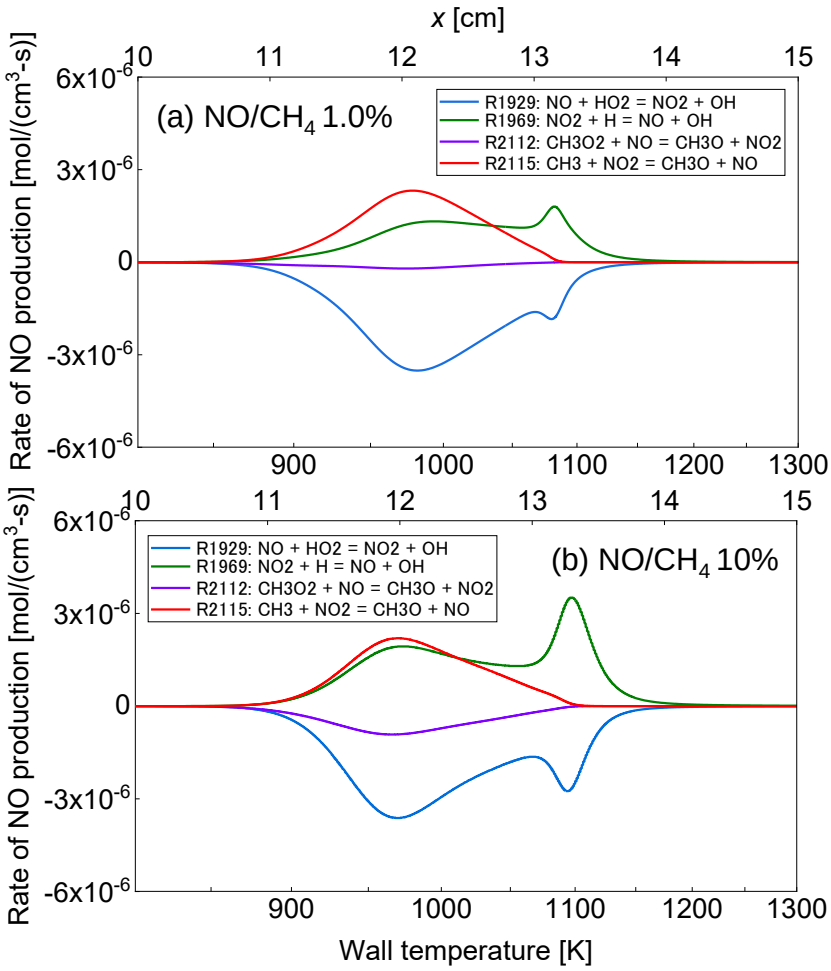

Figure 5-6: Rates of NO production/consumption for (a) NO/CH_4 1.0% and (b) NO/CH_4 10%. Positive/negative values denote species production/consumption.

As discussed in Chapter 4, these reactions are known as the NO–NO_2 loop reactions [33,43,47,116]. Through these reactions, NO and NO_2 convert less-reactive radicals such as HO_2 and CH_3 radicals into more-reactive species such as OH and CH_3O radicals, while NO and NO_2 themselves are regenerated in the loop. The effects of radical sensitization through NO–NO_2 loop reactions on hydrocarbon oxidation have been investigated extensively [42,46,117–120]. Additionally, it should be emphasized that the oxidation from CH_4 to CO proceeds via the reaction sequence, $CH_3 \rightarrow CH_3O \rightarrow CH_2O \rightarrow HCO \rightarrow CO$, and some of CO can be oxidized into CO_2 even from the intermediate temperatures of 900–1000 K. This reaction sequence of the CH_4 oxidation in the intermediate temperatures contributes to the heat releases in the corresponding temperature zones. Therefore, once the CH_4/O_2/Ar mixture contains NO as a mixture component, not only the initial oxidation of CH_4 but also subsequent intermediate temperature reactions can be enhanced, which appears as a large shift of weak flame locations to the lower temperatures between the Neat CH_4 and NO/CH_4 1.0% cases.

5.3.3 Inhibiting effects of NO on reactivity of CH_4/O_2/Ar mixtures

In both experiment and computation, the weak flame location shifts slightly to the higher temperature side as it further increases from NO/CH_4 1.0% to NO/CH_4 10%. This section focuses on how high concentration NO inhibits the reactivity of CH_4/O_2/Ar mixtures.

In the NO/CH_4 1.0% case as shown in Fig. 5-6a, R2115: $CH_3 + NO_2 = CH_3O + NO$ is a

dominant reaction for NO production in the intermediate temperatures whereas R1969: NO_2 + H = NO + OH is dominant in the high temperatures. On the other hand, in the NO/CH_4 10% case presented in Fig. 5-6b, the contribution of R1969: NO_2 + H = NO + OH becomes dominant even in the intermediate temperatures of 900–1000 K. Since H radical is a crucially important species for a chain branching reaction, R5: H + O_2 = O + OH, the rates of H radical consumption are investigated for the NO/CH_4 1.0% and NO/CH_4 10% cases. Figure 5-7 presents the rates of H radical consumption for the NO/CH_4 1.0% and NO/CH_4 10% cases.

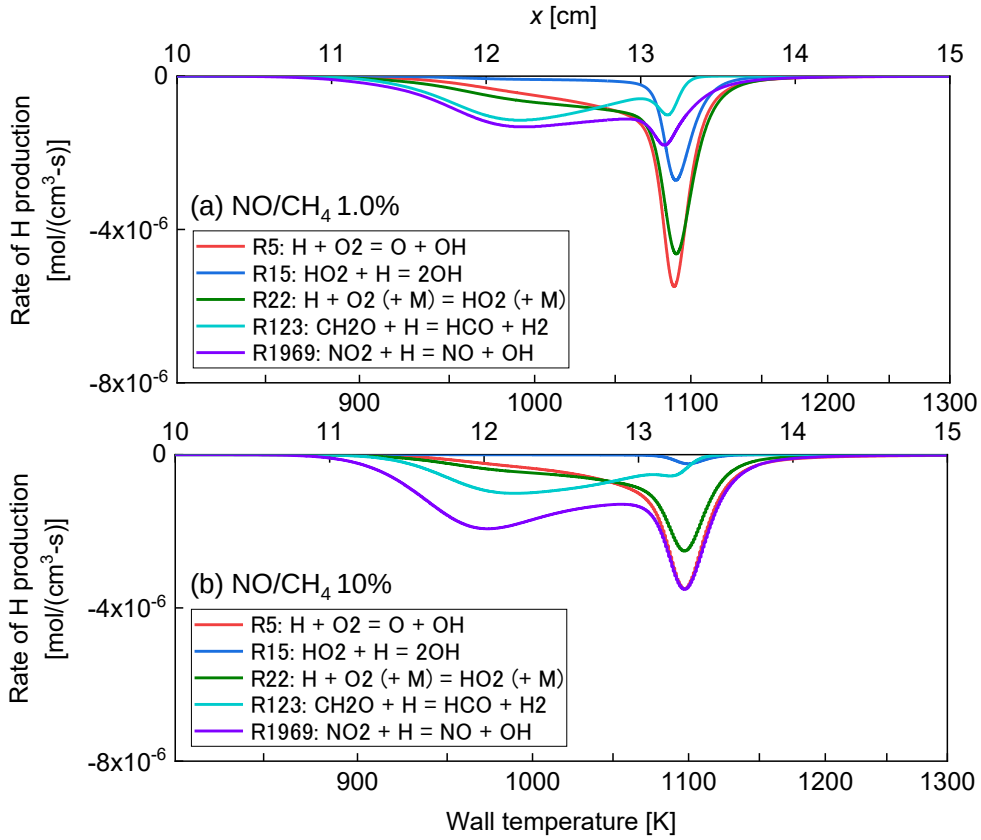

Figure 5-7: Rates of H radical consumption for (a) NO/CH_4 1.0% and (b) NO/CH_4 10%. Negative values denote species consumption.

In the NO/CH_4 1.0% case shown in Fig. 5-7a, R123: $CH_2O + H = HCO + H_2$ and R1969: $NO_2 + H = NO + OH$ are the main consumption reactions of H radicals in the intermediate temperatures of 900–1000 K. On the other hand, R5: $H + O_2 = O + OH$, R15: $HO_2 + H = 2OH$ and R22: $H + O_2 (+M) = HO_2 (+M)$ have large contribution to the H radical consumption in the high temperatures around 1100 K. In the NO/CH_4 10% case, however, R1969: $NO_2 + H = NO + OH$ still retains large contribution to H radical consumption over intermediate-to-high temperatures, and the reaction competes for H radicals with the main chain-branching reaction R5: $H + O_2 = O + OH$. Although the reaction R1969: $NO_2 + H = NO + OH$ produces OH radicals, it is a chain-propagating reaction which does not contribute to radical pool growth. Therefore, the small shift in the weak flame location between the NO/CH_4 1.0% and NO/CH_4 10% cases can be explained as follows. Compared to the Neat CH_4 and NO/CH_4 0.1% cases, the greater production of OH radicals through R1969: $NO_2 + H = NO + OH$ further promotes the CH_4 oxidation, and the weak flame location shifts to the lower temperature side for the NO/CH_4 1.0% case. However, once the NO concentration exceeds a certain point, the chain-propagating reaction R1969: $NO_2 + H = NO + OH$ and the chain-branching reaction R5: $H + O_2 = O + OH$ compete each other for H radicals. This competition for H radicals inhibits the production of active radical species. As a result, the CH_4 oxidation is inhibited and the weak flame location shifts to the slightly higher temperature side. Mathieu et al. had pointed out a similar effects of the NO_2 addition on ignition delay times of H_2/O_2/Ar mixtures in the shock tube experiments [135]. They varied

the NO_2 concentration in the range of 100–1600 ppm in the test mixtures and measured ignition delay times of $H_2/O_2/Ar$ mixtures. When 1600 ppm NO_2 is included in the $H_2/O_2/Ar$ mixture, the ignition delay time became shorter than that of the 100 ppm NO_2 case but it became longer than that of the 400 ppm NO_2 case. According to the computational results in the present study, the maximum NO_2 concentrations within reaction zones were 272 ppm for the NO/CH_4 1.0% case and 713 ppm for the NO/CH_4 10% case, respectively. These values correspond to the criteria in their study reasonably. Therefore, the small shift in the weak flame location observed in the NO/CH_4 10% case caused by the competition for H radicals between the chain-branching reaction R5: $H + O_2 = O + OH$ and the chain-propagating reaction R1969: $NO_2 + H = NO + OH$ due to the increase of NO_2 concentration. These findings contribute to reactivity controls of hydrocarbon fuels in the presence of high concentration NOx especially expected in hydrocarbon/ammonia combustion.

5.4 Conclusions

Effects of high concentration NO on oxidation and reactivity of stoichiometric $CH_4/O_2/Ar$ mixtures were investigated based on weak flame responses in MFR. The NO concentration in the mixture was varied for NO/CH_4 0.1–10%. The experimentally obtained results showed that the weak flame locations of the $CH_4/O_2/Ar$ mixture shifted to the lower temperature side as the NO concentration increased up to NO/CH_4 1.0%. However, the weak flame slightly shifted to the higher temperature side when the NO concentration further increased to

NO/CH_4 10%. These trends indicated that the reactivity of CH_4/O_2/Ar mixtures can be enhanced the NO concentrations increase up to NO/CH_4 1.0% but slightly inhibited for NO/CH_4 10%. The 1-D computation for weak flames could qualitatively reproduce the trends of weak flame locations observed in the experiments. The radical sensitizing effects of NOx through looping reactions of NO and NO_2 can promote the oxidation of CH_4 and the conversion of CH_3 into CH_3O, which realizes the oxidation sequence $CH_4 \rightarrow CH_3 \rightarrow CH_3O \rightarrow CH_2O \rightarrow HCO \rightarrow CO$ from the intermediate temperatures. Therefore, once the CH_4/O_2/Ar mixtures contain NO as a mixture component, not only lower temperature reactions but also subsequent intermediate temperature reactions can be enhanced, which results in visible enhancement in the oxidation of CH_4. The ROP analyses revealed that the great contribution of a chain-propagating reaction $NO_2 + H = NO + OH$ to the H radical consumption inhibits the production of active radical species at the NO concentration of 9480 ppm. Consequently, this results in a slight shift of the weak flame location. Therefore, the shift in the weak flame location observed at the higher NO concentration was mainly caused by the competition for H radicals between the chain-branching reaction $H + O_2 = O + OH$ and the chain-propagating reaction $NO_2 + H = NO + OH$ due to the increased NO_2 concentration.

Chapter 6:
Autoignition-assisted nonpremixed cool flames

6.1 Introduction

In conventional diesel engines, autoignition and autoignition-assisted flame propagation play critical roles in the ignition control. The first-stage ignition and the subsequent transition into a cool flame initiate the combustion process in an engine cylinder. Therefore, understanding cool flame characteristics of biofuels is essential for the efficient use of biofuels in existing diesel engines. Combustion phenomena in practical engines usually take place under high autoignition Damköhler number conditions, which is defined as the ratio between the flow residence time and the chemical reaction time. However, most of existing cool flame studies are conducted under low autoignition Damköhler numbers, where flame stabilization and autoignition are decoupled. In the present chapter, cool flame characteristics under high autoignition Damköhler number conditions are investigated using a counterflow burner and a Co-flow Axisymmetric Reactor-Assisted Turbulent (CARAT) burner introduced in Chapter 2.

In the present chapter, diethyl ether (DEE) is selected as the target fuel because of its rapid first-stage ignition at atmospheric pressure and its potential use as a biofuel for compression-ignition engines [136]. While the combustion characteristics of DEE have been investigated particularly for internal combustion engine conditions [137–140], the flame

stabilization conditions, and extinction and autoignition characteristics of DEE cool flames have not been reported. Moreover, recent works on the extinction of laminar cool flames [60,108,141] revealed that even the state-of-art chemical kinetic models fail to predict cool flame burning limits due to the strong coupling between combustion heat release and low-temperature kinetics. This applies even more to DEE models due to the limited experimental information of DEE oxidation available. Thus, the flame dynamics of DEE cool flames should be investigated under well-defined boundary conditions. Furthermore, essential data for DEE kinetic model development and validation have to be provided.

Motivated by the above discussions, the goal of the present work is to understand the flame stabilization and flame transitions of autoignition-assisted nonpremixed cool flames of DEE. The autoignition and extinction limits of laminar nonpremixed cool flames are first examined in a counterflow burner by varying the fuel concentration. The reproducibility of flame limits by recent chemical kinetic models are also investigated. Next, guided by the laminar flame measurements, turbulent nonpremixed cool flames are established by using a Co-flow Axisymmetric Reactor-Assisted Turbulent (CARAT) burner [61]. The lift-off heights are measured using formaldehyde (CH_2O) planar laser-induced fluorescence (PLIF). Finally, a correlation between the mean lift-off heights of the turbulent cool flames and the first-stage ignition delay times are examined.

6.2 Experimental and computational methods

6.2.1 Counterflow burner experiment

An atmospheric counterflow burner is utilized to stabilize laminar cool flames. The structure of the counterflow burner is presented in Chapter 2. The exit diameter of both the top and bottom burner nozzles is 1.3 cm. Each nozzle is surrounded by a co-flow channel in which heated nitrogen flows. The nozzle separation distance is kept at 2.25 cm throughout all measurements. Diethyl ether (DEE, Sigma Aldrich, anhydrous, ≧99%) is used as the fuel and air is used as the oxidizer. Liquid DEE is injected using a syringe pump (Harvard Apparatus, PHD 22/2000) into the vaporization chamber and mixed with heated nitrogen to facilitate atomization and vaporization. The DEE/nitrogen mixture is then expelled out of the upper burner nozzle and meets the heated air flow from the bottom nozzle. All the flows are heated to 550 K at the nozzle exits, unless otherwise stated. The temperatures of the flow at the nozzle exits are maintained within ±5 K using PID control. Since the cool flame chemiluminescence is quite dim, an unfiltered ICCD camera (Princeton Instruments, PI-MAX 4) is used to monitor the cool flame chemiluminescence.

6.2.2 CARAT burner experiment

The Co-flow Axisymmetric Reactor-Assisted Turbulent (CARAT) burner is employed to stabilize turbulent cool flames under well-defined boundary conditions. The structure of CARAT burner is presented in Chapter 2. The CARAT burner has three flows: an inner (main) fuel flow, a pilot flow, and a co-flow. The main flow velocity (U_0), the mole fraction of DEE

(X_{DEE}), and the flow temperature are varied over the range of 2.5–3.5 m/s, 0.02–0.04 and 500–600 K (based on the measured extinction/ignition limits from the laminar flame measurements), respectively. Both the pilot flow and the co-flow consist of heated air at the velocities of 1.0 m/s and 0.44 m/s, respectively. To prevent the recirculation flow occurring between the main flow and the co-flow, the pilot flow velocity is set to a non-zero value. The pilot flow can consist of pure O_2 to facilitate cool flame observation for some less reactive fuels. However, air is used as an oxidizer in this study as a result of the strong low temperature oxidation of DEE. Since cool flames exhibit weak chemiluminescence, planar laser-induced fluorescence of formaldehyde (CH_2O-PLIF) is used to measure the cool flame lift-off heights. Note that the formaldehyde fluorescence observed is entirely due to the strong low-temperature oxidation of DEE. Excitation is performed using the output of a frequency-tripled Nd:YAG laser (Quantel Q-smart 850, 355 nm, 10 Hz) at a beam energy of ~200 mJ/pulse. The beam is expanded into a sheet 200-μm in thickness and is incident over the centerline of the burner. The fluorescence is captured by a filtered ICCD camera (Princeton Instruments, PI-Max) through a GG-395 longpass filter. One hundred fluorescence images are averaged for each condition to produce a mean PLIF image for the observation of flame structure and lift-off height.

6.2.3 Numerical models

For the numerical work in this chapter, two different computations are conducted. To

simulate laminar counterflow flames, the steady one-dimensional computation is conducted using the OPPDIF package of Chemkin-Pro v19.0 [93]. Several chemical kinetic models are validated against the measured flame limits. The boundary conditions for the computation are determined based on the experimental conditions. The global strain rate is determined from burner exit velocities/compositions in the experiment based on the equations (2.1) and (2.2) presented in Chapter 2. The simulation employs same mixture flow velocities at nozzle exits as the experiment. A pseudo arc-length continuation procedure (i.e., OPPDIF calculations with restarts of previous solutions) is used to find HFE/CFE by increasing the strain rate gradually at a constant fuel concentration. The turning point right before a solution jumps off the hot/cool flame branch is determined as the hot/cool flame extinction limits.

To calculate adiabatic ignition delay times of DEE/air mixtures, the transient zero-dimensional computation is conducted using the AURORA package of Chemkin-Pro v19.0. The computation is conducted under a constant volume assumption. The peaks in the time history of [OH] are detected. As shown in Fig. 6-1, if there appear two peaks in a time history of [OH], the periods from the starting time to the first and second peaks are defined as the 1st and total ignition delay times, respectively.

The DEE kinetic models from the literature include the Tran model [142], the Tang model [143], and the Serinyel model [144]. Species and reactions that do not participate significantly in the DEE low-temperature oxidation have been removed from the Tran and Serinyel models, for the purpose of computational efficiency.

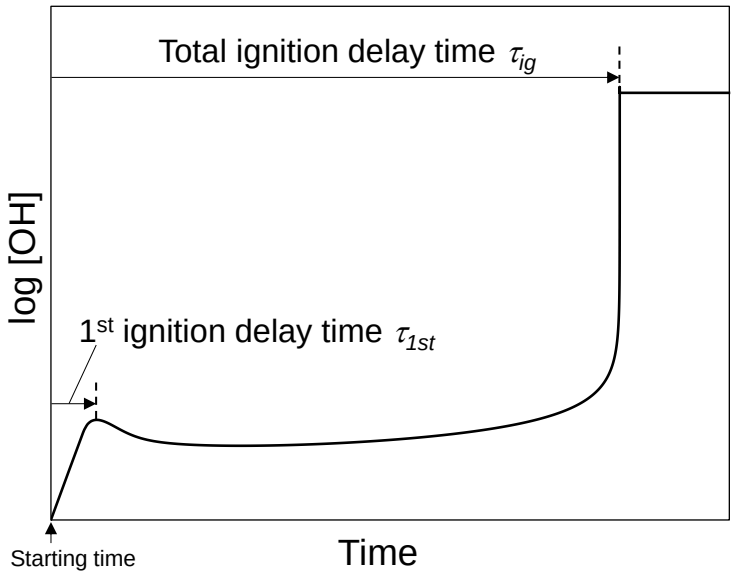

Figure 6-1: Definition of the 1st and total ignition delay times.

6.3 Results and discussions

6.3.1 Extinction and autoignition limits and auto-ignition assisted flames

In the present chapter, all experiments are conducted at atmospheric pressure. To measure the counterflow extinction limits (or ignition limits), the strain rate (a) is increased (or decreased) by simultaneously varying the nitrogen and air flow rates until a flame extinguishes (or ignites) while holding constantly the location of the stagnation plane. The "density-weighted" strain rate is determined from burner exit velocities and mixture composition in the experiment, and the simulation employs these same velocities and mixture composition, that is, the measurements and computational predictions are compared under the same boundary conditions. Figure 6-2a shows the comparison between experimental results and computational predictions for the extinction strain rates of both hot flames and cool flames plotted against the DEE mole fraction. In the measurements, the cool flame extinction

(CFE) limit is found to exceed the hot flame extinction (HFE) limit as the DEE fraction decreases between X_{DEE} = 0.1 and 0.08, resulting in a crossover point between HFE and CFE. This crossover point indicates the existence of a hysteresis between HFE and CFE. Similarly, Fig. 6-2b shows the computed hot flame and cool flame branches for two different fuel concentrations. For X_{DEE} = 0.12, hot flames directly extinguish into unburned mixtures as the strain rate is increased beyond the HFE limit. On the other hand, when the fuel concentration is lower (X_{DEE} = 0.03), the CFE limit exceeds the HFE limit. In this case, as the strain rate is increased, hot flames do not directly extinguish into unreactive mixtures but rather transition into cool flames [145]. Similarly, re-ignition of a cool flame at low strain rates results in the transition to a hot flame. This hysteresis between HFE and CFE occurs due to the higher sensitivity to the flame temperature of the hot flame [56].

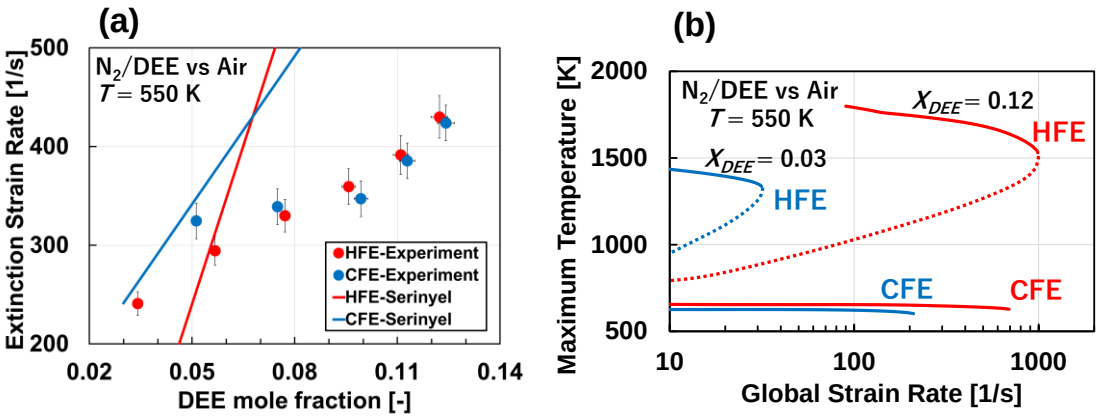

Figure 6-2: (a) Comparison of hot flame extinction (HFE) and cool flame extinction (CFE) limits between the experimental measurements and computational predictions for diluted DEE/air nonpremixed flames at T = 550 K and (b) computed hot and cool flame branches for diluted DEE/air cool flames at T = 550 K and two different DEE mole fractions with the Serinyel model [144]**.**

For the computation, although three kinetic models are employed, only the results by the Serinyel model are shown in Fig. 6-2a because the predictions by the Tran model and the Tang model are greatly different from the measurements (a_{CFE} < 200 s^{-1} for all X_{DEE} conditions). For the HFE limits, the Serinyel model overpredicts HFE at high X_{DEE} while it underpredicts HFE limits in low X_{DEE} region. For the CFE limits, although the Serinyel model generally lies above the measured CFE extinction strain rate, it can predict the CFE limits reasonably well for low X_{DEE} conditions. As observed in the experiments, a crossover between HFE and CFE also appears in the computational prediction at X_{DEE} ~ 0.068 with the Serinyel model. Note that the crossover point is also qualitatively replicated by the other two models (at X_{DEE} ~ 0.030 with the Tang model and at X_{DEE} ~ 0.037 with the Tran model), albeit under different conditions.

Next, the autoignition limits of cool flames are investigated by decreasing the fuel concentration (X_{DEE} = 0.05–0.13) at two different air temperatures. For the mixtures considered and for strain rates above a ~ 40 s^{-1}, no autoigniting cool flames can be observed at T = 500 K. However, autoignition-assisted cool flames are successfully stabilized at T = 550 K. The experimentally observed low-temperature autoignition (LTI) limits are plotted together with CFE in Fig. 6-3a. Although the strain rate at the CFE and LTI limits are quite close over the range considered, when the DEE fraction is larger than X_{DEE} ~ 0.10, the gap between CFE and LTI becomes larger. The cool flame at large X_{DEE} has a low autoignition Damköhler number and is therefore not stabilized as a result of autoignition. However, as the

DEE fraction becomes lower than X_{DEE} ~ 0.10, the CFE and LTI limits approach each other and eventually merge together. For X_{DEE} < 0.05, CFE and LTI are indistinguishable (loss of criticality occurs), therefore not presented.

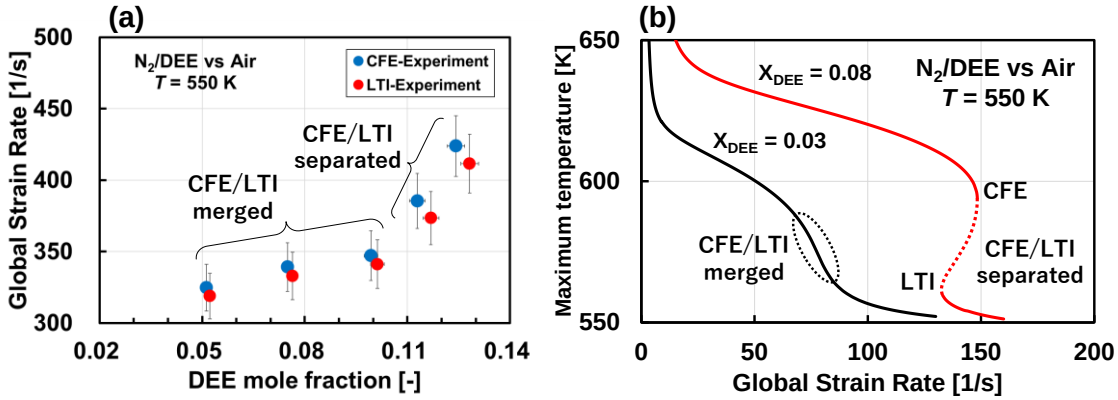

Figure 6-3: (a) Measured cool flame extinction (CFE) limits and the low temperature ignition (LTI) limits at T = 550 K and (b) computed ignition-to-extinction branches for diluted DEE/air cool flames at T = 550 K and two different DEE fractions with the Tran model [142]**.**

Figure 6-3b shows the computed S-curves (bifurcations diagrams showing the stable steady-state flame temperatures as a function of strain rate) using the Tran model [142] for X_{DEE} = 0.03 and 0.08 at T = 550 K. X_{DEE} = 0.03 corresponds to the fuel concentration for the merged CFE/LTI condition in Fig. 6-3a. Figure 6-3b shows that the ignition and extinction curves have two distinct relationships between the CFE and LTI limits. At a higher fuel concentration (X_{DEE} = 0.08) the CFE and LTI limits are separated, that is, moving between the cool flame and unburning steady states requires an extinction or ignition transition, and there exists a hysteresis between the CFE and the LTI limits. However, at a lower fuel concentration,

X_{DEE} = 0.03, the CFE and the LTI limits merge and the hysteresis disappears (loss of criticality occurs). Under this condition, there is a smooth transition between the unburning mixture and the cool flame. This cool flame regime corresponds to the CFE/LTI merged branch in Fig. 6-3a and is termed the autoignition-assisted cool flame regime. This flame regime provides a good validation target for the autoignition chemistry of the kinetic models and for the study of auto-ignition assisted turbulent flames. Therefore, based on these nonpremixed laminar flame measurements shown in Fig. 6-3, the turbulent autoignition-assisted cool flames can be readily stabilized in the DEE mole fraction range of X_{DEE} = 0.02-0.04 at the temperature of 550 K.

6.3.2 Autoignition-assisted turbulent lifted cool flames

In the previous section, the extinction and autoignition limits of laminar dilute DEE/air cool flames were measured in a counterflow configuration. According to the measurements in Fig. 6-3, autoignition-stabilized DEE/air nonpremixed cool flames can be realized at low fuel concentration (X_{DEE} ~ 0.02–0.04) at an air temperature of 550 K. Therefore, the stabilization of turbulent nonpremixed lifted cool flames is attempted in the CARAT burner under the following conditions: the main flow velocity, the DEE concentration, and the flow temperature are varied over the range of U_0 = 2.5–3.5 m/s, X_{DEE} = 0.02–0.04, and T = 500–600 K, respectively.

Figure 6-4a shows an instantaneous CH_2O-PLIF image of a turbulent cool flame for

X_{DEE} = 0.04 and U_0 = 3.00 m/s. The lifted flames are stabilized by autoignition at T = 550 K. Note that, at the main flow velocities used, the cool flames remain attached to the burner and are unable to lift off at T = 600 K. Moreover, under the present conditions, cool flames cannot be stabilized by autoignition at T = 500 K. These results are consistent with the laminar experiments, that is, isolated autoignition-stabilized cool flames are realized at a critical fuel concentration and at temperatures of T = 550 K or higher.

To quantify the mean lift-off height (H_L) of the turbulent lifted cool flames, averaged CH_2O-PLIF images are generated. The averaged CH_2O-PLIF images for the X_{DEE} = 0.04 condition can be seen in Fig. 6-4b. The lift-off height is defined as the lowest point above the burner where a PLIF signal of 70,000 counts is achieved (the PLIF images in Fig. 6-4b are on a scale of 62,000 to 95,000 counts). We note that the measured lift-off heights are not particularly sensitive to reasonable variations in the count threshold.

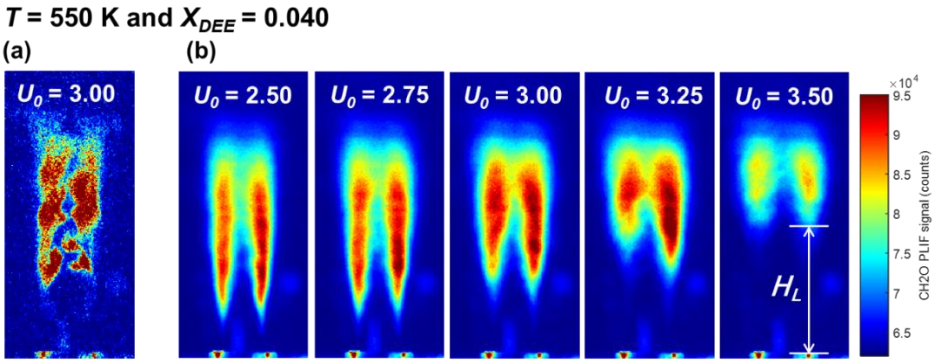

Figure 6-4: (a) An instantaneous CH_2O-PLIF image of a DEE lifted cool flame at U_0 = 3.00 m/s with X_{DEE} = 0.04 and T = 550 K and (b) the averaged CH_2O-PLIF images of DEE lifted flames at different main flow velocities with X_{DEE} = 0.04 and T = 550 K.

Based on the averaged PLIF images in Fig. 6-4b, the lift-off heights (H_L) of autoignition-assisted lifted cool flames at T = 550 K are measured and are plotted in Fig. 6-5. Decreasing the DEE mole fraction in the main flow increases H_L. H_L also increases as U_0 increases at a constant DEE mole fraction; however, the trend becomes nonlinear as the DEE fraction increases. This is caused by the inevitable heat loss during the autoignition process [146]. Specifically, Choi et al. [146–148] have proposed the following scaling for the lift-off height of autoignition-assisted lifted flames, based on a simple timescale argument: $H_L \sim U_0 \cdot \tau_{ig,ad}{}^2$ ($\tau_{ig,ad}$: the adiabatic total ignition delay time). Based on the thermal explosion theory [149], the following relation can be held between the Frank-Kamenetskii parameter (δ) and adiabatic/non-adiabatic ignition delay times ($\tau_{ig,ad}$, τ_{ig}):

$$\delta \sim \left(\frac{\tau_{ig,ad}}{\tau_{ig}}\right)^2 . \tag{6.1}$$

Since δ is correlated to the Damköhler number, which is expressed as τ_{Flow}/τ_{ig} (τ_{Flow}: the characteristic flow time), this relation can be regarded as the following form:

$$\tau_{ig} \sim \frac{\tau_{ig,ad}^2}{\tau_{Flow}} . \tag{6.2}$$

According to the experiments by Choi et al. [147], τ_{Flow} under non-adiabatic condition has the dependence on $\tau_{ig,ad}{}^2$. Since τ_{Flow} can be expressed as H_L/U_0, the proportionality can be derived:

$$H_L \sim U_0 \cdot \tau_{ig,ad}^2 . \tag{6.3}$$

In the present case, heat loss increases as the DEE fraction (and hence flame temperature) increases, which results in the trend in Fig. 6-5.

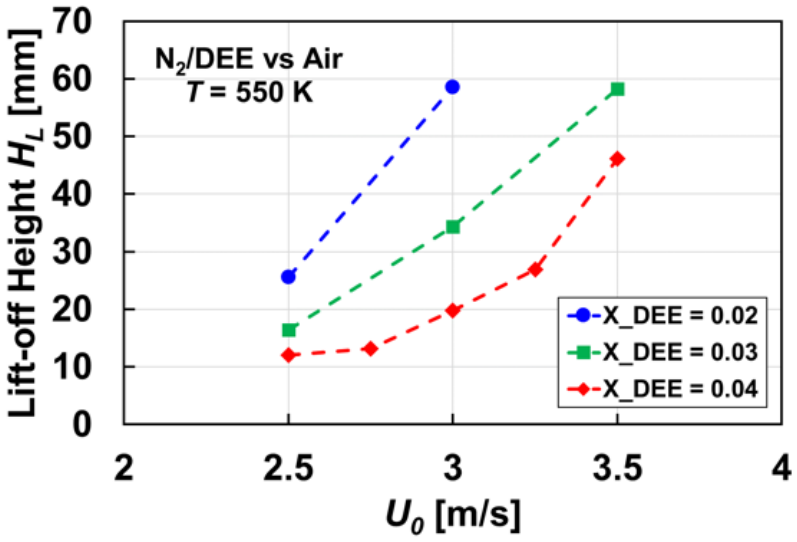

Figure 6-5: Measured cool flame lift-off heights (H_L) in the CARAT burner as a function of the main flow velocity (U_0) at T = 550 K.

Note that the results shown above are for weakly turbulent (Re_T ~ 30) flow conditions. Thus, it is reasonable to assume that the similar physics for laminar autoignition-assisted lifted flames hold for the present weakly turbulent conditions. Based on the assumption, a modified correlation is introduced as the scaling of the lift-off height of turbulent lifted cool flames:

$$H_L \sim U_0 \cdot \tau_{1st}^2 \,, \tag{6.4}$$

where τ_{1st} is the adiabatic first-stage ignition delay time. The τ_{1st} are calculated using an adiabatic homogeneous reactor model for stoichiometric DEE/air mixtures. The scaling results are shown in Fig. 6-6. Between the three models employed, the Serinyel model, which showed the best prediction of the CFE limits of DEE, especially for dilute conditions, collapses the measurements well. However, the Tang model and Tran model do not display the same level of correlation, which is reasonable since these models could not reproduce the

experimental flame limits. This result suggests that the physics of weakly turbulent autoignition-assisted lifted cool flames is analogous to that of the hot flame, that is, that the lift-off height of a cool flame is determined by the balance between the heat generation due to low-temperature oxidation and the heat loss as a result of the thermal dissipation in a turbulent mixing layer. Moreover, the results suggest that autoignition-assisted cool flame lift-off heights can potentially be used as targets for the chemical kinetic model validation.

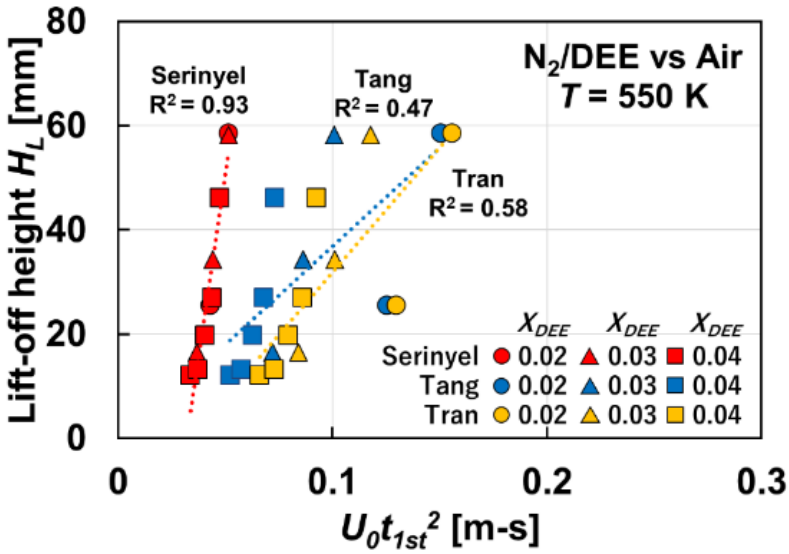

Figure 6-6: Correlation of cool flame lift-off heights (H_L) using first-stage ignition delay times (τ_{1st}) at T = 550 K calculated by the Serinyel model [144]**, the Tang model** [143] **and the Tran model** [142]**.**

6.4 Conclusions

The autoignition-assisted laminar and turbulent non-premixed cool flames of diethyl ether were investigated over various fuel concentration and temperatures. Laminar cool flame extinction and autoignition limits of DEE/air non-premixed flames were examined in a laminar counterflow burner configuration to identify the critical conditions under which

autoignition-assisted turbulent cool flames can be stabilized. The measurements showed that, with the decrease of fuel concentration, the cool flame extinction limit can exceed that of the hot flame. Under this condition, a hot flame can extinguish directly into a cool flame, and a cool flame can likewise re-ignite and transition to a hot flame. Moreover, with a further decrease of fuel concentration, the extinction limit of cool flames merges with the low-temperature ignition limit, resulting in an autoignition-assisted cool flame. Under this condition, a hysteresis between the cool flames and the unreactive mixtures disappears and a monotonic transition between the unburning mixtures and the cool flames appears. The measured extinction and autoignition limits are used to validate chemical kinetic models of DEE oxidation. The Serinyel model showed the best prediction of measured flame limits, especially at low fuel concentration.

At low fuel concentration suggested by the laminar flame measurements, a turbulent autoignition-assisted lifted cool flame of DEE/air was successfully observed at T = 550 K in the CARAT burner. A lift-off height scaling from a previous study of autoignition-assisted laminar lifted flames was modified for this study to $H_L \sim U_0 \cdot \tau_{1st}^2$, where τ_{1st} is the first-stage ignition delay time in a homogeneous reactor. The Serinyel model, which showed the best predictions of the measured laminar flame limits, also displayed the best correlation to the turbulent flame lift-off heights. These results imply that both counterflow cool flame extinction/ignition limits and autoignition-assisted cool flame lift-off heights can be used as targets for chemical kinetic model validation.

Chapter 7:
Conclusions and recommendations

7.1 Conclusions

In response to the rapid climate change, world's energy structure has been changing drastically. The introduction of low- and zero-carbon fuels to combustion applications is recommended strongly in all sectors including power generation, transportation, industry, buildings. Better understanding in combustion characteristics of new fuels is required for their flexible and efficient usage in conventional combustion applications. This dissertation focuses on oxidation and reactivity of various fuel mixtures, including syngas, small hydrocarbons, biofuels, and ammonia. Mixture composition is widely varied and its effects on mixture reactivity are investigated based on weak flame responses in a micro flow reactor with a controlled temperature profile. Dominant chemical reactions and species, which control oxidation and reactivity of mixtures, are identified for each mixture. Obtained results suggested that overall reactivity of mixtures is strongly affected by low-to-intermediate temperature chemical reactions preceding high temperature reactions.

In Chapter 3, in-cylinder fuel reforming characteristics of n-tridecane/air mixtures and the reactivity of $CO/H_2/CH_4$ mixtures were investigated. First, reformate products from in-cylinder fuel reforming of n-tridecane/air mixtures were estimated by the 0-D adiabatic transient simulation. The obtained results showed that the mole fractions of CO and H_2

become maximum at $\phi \approx 3$ and above $T_i \approx 500$ K, and then decrease as the equivalence ratio increases. The CO mole fraction is almost constant above $\phi \approx 5$ and $T_i \approx 500$ K while the H_2 mole fraction further decreases as the equivalence ratio increases. CH_4 and C_2H_4 are not produced below $\phi \approx 4$ while mole fractions of these species increase greatly above $\phi \approx 5$ and $T_i \approx 500$ K. Based on the estimated composition of reformate products, CO, H_2 and CH_4 were selected as representative components. Weak flame locations of the $CO/H_2/CH_4$ mixtures were investigated using MFR. Both experimental and numerical results showed that weak flame of $CO/H_2/CH_4$ mixtures shifted greatly to the higher temperature region as the H_2 fraction decreases and the CH_4 fraction increases, indicating the reactivity of the $CO/H_2/CH_4$/air mixtures decreases. ROP analysis for OH radicals demonstrated that OH radicals are consumed mainly by fuel components, CO, H_2, and CH_4 in all mixture compositions. For the CO/H_2 mixtures, OH radicals are mainly consumed by CO and H_2. Subsequently, H radicals are produced through $H_2 + OH = H + H_2O$ and $CO + OH = H + CO_2$. However, once CH_4 is included in the CO/H_2 mixtures, CH_4 also consumes OH radicals through $CH_4 + OH = CH_3 + H_2O$ and produces CH_3 radicals, which are less reactive species. The consumption rate of OH radicals by CH_4 became larger as the CH_4 fraction increased. Therefore, the primary factor of the significant decrease in the reactivity of the $CO/H_2/CH_4$ mixtures is the increase of the OH consumption by CH_4 and the CH_3 radical production due to the increase of the CH_4 fraction.

In Chapter 4, effects of composition and equivalence ratios on oxidation and reactivity of

DME/NH_3 mixtures were investigated using weak flame responses in MFR.

The trends in experimental and numerical results showed that the addition of small amounts of NH_3 (up to 15% in fuel blends) promotes the DME oxidation. As the NH_3 fraction increased further from 15% to 50%, the reactivity of DME/NH_3 mixtures decreased greatly. ROP analyses revealed that when NH_3 is blended with DME, low-to-intermediate temperature oxidation of DME induces NH_3 oxidation at around 800–1000 K, and NO and NO_2 are produced. The NO and NO_2 convert less-reactive radicals into more-reactive radicals (HO_2→ OH and CH_3→CH_3O) through the NO–NO_2 catalytic loop (NO + HO_2 = NO_2 + OH, NO_2 + H = NO + OH, NO_2 + CH_3 = NO + CH_3O). Radical sensitization through the NO–NO_2 catalytic loop promotes active radical production in the blue flame zone. This is the main reason why fuel oxidation is promoted with additions of small amounts of NH_3. However, when the NH_3 fraction in fuel blends increases further from 15% to 50%, more NH_3 consumes OH radicals in the blue flame zone instead of CO. Consequently, the CO oxidation in the blue flame zone is inhibited, resulting in large decreases in reactivity of DME/NH_3 mixtures. Hot flame locations of the DME/NH_3 = 100/0 blends changed only slightly as the equivalence ratio increased. However, when NH_3 was blended with DME, hot flames moved to the higher temperature side as the equivalence ratio increased. Because of the higher activation energy of the CO, OH radicals are mostly consumed by DME, CH_2O, NH_3, and H_2, but not by CO in the blue flame zone for richer equivalence ratios. At richer equivalence ratios, the CO oxidation was inhibited even in the hot flame zone because excess amounts of NH_3 and H_2

consumed more OH radicals. Therefore, the CO oxidation in the blue flame zone was inhibited, and hot flames shifted to the higher temperature side as the equivalence ratio increases only when NH_3 is blended with DME. These results indicate that NH_3 is capable of not only inhibiting but also promoting reactivity of hydrocarbon mixtures by changing the blending ratios and equivalence ratios.

In Chapter 5, effects of high concentration of NO on reactivity of CH_4/O_2/Ar mixtures were investigated. The observed weak flame locations indicated that the reactivity of CH_4/O_2/Ar mixtures was enhanced greatly as the NO concentration increased up to NO/CH_4 1.0%. However, the reactivity of the mixtures was inhibited when the NO concentration increased further up to NO/CH_4 10%. Chemical reaction analyses revealed that the NO–NO_2 loop reactions effectively convert less reactive radicals into more reactive radicals, i.e., $CH_3 \rightarrow CH_3O$, $HO_2 \rightarrow OH$, in intermediate temperatures of 900–1000 K, which were also discussed in Chapter 4. This radical sensitization by NO–NO_2 loop reactions promotes CH_4 oxidation from intermediate temperatures. Consequently, the oxidation of CH_4 is completed at much lower temperatures for the NO/CH_4 1.0% than that for the Neat CH_4 case. However, as the NO concentration increases further from NO/CH_4 1.0% to NO/CH_4 10%, the H radical consumption through $NO_2 + H = NO + OH$ becomes larger in both intermediate and high temperature region. Especially in high temperatures around 1100 K, $NO_2 + H = NO + OH$ competes with $H + O_2 = O + OH$ for H radicals. Since $NO_2 + H = NO + OH$ is a chain-propagating reaction, the reaction does not contribute to the increase of active radicals, while

the reaction $H + O_2 = O + OH$ does because it is a chain-branching reaction. Therefore, H radical consumption $NO_2 + H = NO + OH$ inhibits active radical production through $H + O_2 = O + OH$. Consequently, the CH_4 oxidation is inhibited, and the reactivity is decreased slightly for the NO/CH_4 10% case.

In Chapter 6, the autoignition-assisted laminar and turbulent non-premixed cool flames of diethyl ether (DEE) were investigated. For the laminar experiment, extinction and autoignition limits of DEE/air nonpremixed cool flames were examined in a laminar counterflow burner configuration. The experimental results indicated that there is a condition where the cool flame extinction limit can exceed that of the hot flame as the fuel concentration decreased. Under this condition, the hysteresis between a hot flame and a cool flame appeared, i.e., a hot flame extinguishes directly into a cool flame, and a cool flame re-ignite and transition to a hot flame. As the fuel concentration was further decreased, the extinction limit of a cool flame merged with the low-temperature ignition limit, resulting in the disappearance of the hysteresis between a cool flame and an unreactive mixture. The cool flames observed under this condition is an autoignition-assisted cool flame. Based on this finding, the conditions for turbulent cool flame experiments were determined, and a turbulent autoignition-stabilized lifted cool flame of DEE/air was successfully observed at T = 550 K in a CARAT burner. A lift-off height scaling from a previous study of autoignition-stabilized laminar lifted flames was modified for this study to $H_L \sim U_0 \cdot \tau_{1st}^2$, where τ_{1st} is the first-stage ignition delay time in a homogeneous reactor. The Serinyel model, which showed the best

predictions of the measured laminar flame limits, also provided the best correlation to the turbulent flame lift-off heights. Results obtained through the experimental work imply that both counterflow cool flame extinction/ignition limits and autoignition-assisted cool flame lift-off heights can be used as targets for chemical kinetic model validation.

7.2 Future recommendations

7.2.1 NH_3 reforming (Super-rich NH_3 combustion)

Fuel reforming of NH_3 at rich equivalence ratios should be an interesting topic to investigate. As mentioned in Chapter 4, NH_3 is a great H_2 source because the volumetric hydrogen density of liquid NH_3 is 1.5 times larger than that of liquid H_2. To produce H_2 from NH_3 effectively, thermal reforming of NH_3 is one key method. However, combustion characteristics of NH_3 at rich equivalence ratios have not been investigated well. Judging from the results of Chapter 4, the onset temperature of NH_3 oxidation is controllable with addition of reactive species which provides active radicals to the system. In the presence of hydrocarbons with multi-stage oxidation, NH_3 oxidation at low-to-intermediate temperatures can be realized. Since cool and blue flame reactions are strengthened at richer equivalence ratios, chemical interactions between NH_3 and hydrocarbon at low-to-intermediate temperatures may also be more strengthened. If this is possible, H_2 production from NH_3 in low-to-intermediate temperatures may be achieved.

7.2.2 Cool flames under turbulent/elevated pressure conditions

In actual internal combustion engines, the conditions in an engine cylinder is expected to be turbulent and high pressure. To investigate cool flame characteristics under engine-relevant conditions, turbulent/high pressure cool flame experiment should be conducted. Although turbulent nonpremixed cool flames were realized in the present work, the condition is still limited to a weakly turbulent condition. To further investigate roles of cool flames under an engine-relevant condition, the levels of turbulence should be expanded. Although diethyl ether (DEE) has strong low temperature reactions, turbulent DEE cool flames can be sustained with higher level of turbulence by adding ozone in the oxidizer.

Nomenclature

Symbol	Description	units
A	Cross sectional area of the stream tube encompassing the flame	cm^2
a	Strain rate	1/s
c_p	Specific heat capacity at constant pressure of the gas mixture	ergs/(g· K)
c_{pk}	Specific heat capacity at constant pressure of the *k*th chemical species	ergs/(g· K)
D	Nozzle diameter of counter flow burner	mm
d	Diameter of the reactor	cm
Da	Damköhler number	-
h_k	Specific enthalpy of the *k*th species	ergs/g
K	Total number of species	-
L	Separation distance between nozzles	mm
$\dot{M}$	Mass flux	g/cm^3
Nu	Nusselt number	-
Re	Reynolds number	-
Re_T	Turbulent Reynolds number	-
T	Gas phase temperature	K
T_0	Temperature at the inlet of the well-stirred reactor	K
T_w	Wall temperature of the micro flow reactor	K
U_F	Velocity of the fuel flow at nozzle exit	cm/s
U_O	Velocity of the oxidizer flow at nozzle exit	cm/s
u_{rms}	Root mean square of the turbulent velocity fluctuations	cm/s
Y_k	Mass fraction of the *k*th chemical species	-
λ	Specific heat capacity at constant pressure of gas mixture	cm^2/s
ρ_F	Density of the fuel flow at nozzle exit	kg/m^3
ρ_O	Density of the oxidizer flow at nozzle exit	kg/m^3
$\dot{\omega}$	Rate of production of the *k*th chemical species	mol/s
ϕ	Equivalence ratio	-

References

[1] International Energy Agency, Net Zero by 2050, 2021.

[2] UNFCCC, Kyoto Protocol to the United Nations Framework Convention on Climate Change, Kyoto, Japan, 1997, available at https://unfccc.int/sites/default/files/resource/docs/cop3/l07a01.pdf.

[3] UNFCCC, Paris Agreement to the United Nations Framework Convention on Climate Change, 2015, available at https://unfccc.int/files/essential_background/convention/application/pdf/english_paris_agreement.pdf.

[4] Japan Ship Technology Research Association, Ministry of Land Infrastructure Transport and Tourism, Roadmap to Zero Emission from International Shipping, 2020, available at https://www.mlit.go.jp/common/001354314.pdf.

[5] International Maritime Organization, PROTOCOL OF 1978 RELATING TO THE INTERNATIONAL CONVENTION FOR THE PREVENTION OF POLLUTION FROM SHIPS, 1973, available at https://wwwcdn.imo.org/localresources/en/KnowledgeCentre/ConferencesMeetings/Documents/MARPOL%20Protocol%20of%201978.pdf.

[6] International Maritime Organization, AMENDMENTS TO THE ANNEX OF THE PROTOCOL OF 1997 TO AMEND THE INTERNATIONAL CONVENTION FOR THE PREVENTION OF POLLUTION FROM SHIPS, 1973, AS MODIFIED BY THE

PROTOCOL OF 1978 RELATING THERETO, MEPC.132(53), 2005, available at https://wwwcdn.imo.org/localresources/en/KnowledgeCentre/IndexofIMOResolutions/MEPCDocuments/MEPC.132(53).pdf.

[7] International Maritime Organization, AMENDMENTS TO THE ANNEX OF THE PROTOCOL OF 1997 TO AMEND THE INTERNATIONAL CONVENTION FOR THE PREVENTION OF POLLUTION FROM SHIPS, 1973, AS MODIFIED BY THE PROTOCOL OF 1978 RELATING THERETO, MEPC.203(62), 2011, available at https://wwwcdn.imo.org/localresources/en/KnowledgeCentre/IndexofIMOResolutions/MEPCDocuments/MEPC.203(62).pdf.

[8] International Maritime Organization, INITIAL IMO STRATEGY ON REDUCTION OF GHG EMISSIONS FROM SHIPS, MEPC.304(72), 2018, available at https://wwwcdn.imo.org/localresources/en/KnowledgeCentre/IndexofIMOResolutions/MEPCDocuments/MEPC.304(72).pdf.

[9] M. Koebel, M. Elsener, M. Kleemann, Urea-SCR: a promising technique to reduce NOx emissions from automotive diesel engines, Catal. Today 59 (2000) 335–345.

[10] R. Burch, J.P. Breen, F.C. Meunier, A review of the selective reduction of NOx with hydrocarbons under lean-burn conditions with non-zeolitic oxide and platinum group metal catalysts, Appl. Catal. B Environ. 39 (2002) 283–303.

[11] L. Tartakovsky, M. Sheintuch, Fuel reforming in internal combustion engines, Prog. Energy Combust. Sci. 67 (2018) 88–114.

[12] T. Kamimoto, M.H. Bae, High combustion temperature for the reduction of particulate in diesel engines, SAE Tech. Pap. (1988) 880423.

[13] K. Akihama, A Point of Contact between a φ-T Map and Engine Combustion Concepts, J. Combust. Soc. Japan 56 (2014) 291–297.

[14] R. Chacartegui, M. Torres, D. Sánchez, F. Jiménez, A. Muñoz, T. Sánchez, Analysis of main gaseous emissions of heavy duty gas turbines burning several syngas fuels, Fuel Process. Technol. 92 (2011) 213–220.

[15] K. Göransson, U. Söderlind, J. He, W. Zhang, Review of syngas production via biomass DFBGs, Renew. Sustain. Energy Rev. 15 (2011) 482–492.

[16] T. Tian, Q. Li, R. He, Z. Tan, Y. Zhang, Effects of biochemical composition on hydrogen production by biomass gasification, Int. J. Hydrogen Energy 42 (2017) 19723–19732.

[17] Ministry of Land Infrastructure Transport and Tourism, Green Growth Strategy Through Achieving Carbon Neutrality in 2050, 2020.

[18] A. Valera-Medina, H. Xiao, M. Owen-Jones, W.I.F. David, P.J. Bowen, Ammonia for power, Prog. Energy Combust. Sci. 69 (2018) 63–102.

[19] H. Kobayashi, A. Hayakawa, K.D.K.A. Somarathne, E.C. Okafor, Science and technology of ammonia combustion, Proc. Combust. Inst. 37 (2019) 109–133.

[20] O. Kurata, N. Iki, T. Matsunuma, T. Inoue, T. Tsujimura, H. Furutani, H. Kobayashi, A. Hayakawa, Performances and emission characteristics of NH3-air and NH_3-CH_4-air

combustion gas-turbine power generations, Proc. Combust. Inst. 36 (2017) 3351–3359.

[21] J. Li, H. Huang, N. Kobayashi, C. Wang, H. Yuan, Numerical study on laminar burning velocity and ignition delay time of ammonia flame with hydrogen addition, Energy 126 (2017) 796–809.

[22] X. He, B. Shu, D. Nascimento, K. Moshammer, M. Costa, R.X. Fernandes, Auto-ignition kinetics of ammonia and ammonia/hydrogen mixtures at intermediate temperatures and high pressures, Combust. Flame 206 (2019) 189–200.

[23] A. Ichikawa, A. Hayakawa, Y. Kitagawa, K.D. Kunkuma Amila Somarathne, T. Kudo, H. Kobayashi, Laminar burning velocity and Markstein length of ammonia/hydrogen/air premixed flames at elevated pressures, Int. J. Hydrogen Energy 40 (2015) 9570–9578.

[24] M. Pochet, V. Dias, B. Moreau, F. Foucher, H. Jeanmart, F. Contino, Experimental and numerical study, under LTC conditions, of ammonia ignition delay with and without hydrogen addition, Proc. Combust. Inst. 37 (2019) 621–629.

[25] L. Dai, S. Gersen, P. Glarborg, H. Levinsky, A. Mokhov, Experimental and numerical analysis of the autoignition behavior of NH_3 and NH_3/H_2 mixtures at high pressure, Combust. Flame 215 (2020) 134–144.

[26] J.H. Lee, J.H. Kim, J.H. Park, O.C. Kwon, Studies on properties of laminar premixed hydrogen-added ammonia/air flames for hydrogen production, Int. J. Hydrogen Energy 35 (2010) 1054–1064.

[27] P. Kumar, T.R. Meyer, Experimental and modeling study of chemical-kinetics mechanisms for H_2-NH_3-air mixtures in laminar premixed jet flames, Fuel 108 (2013) 166–176.

[28] O. Mathieu, M.M. Kopp, E.L. Petersen, Shock-tube study of the ignition of multi-component syngas mixtures with and without ammonia impurities, Proc. Combust. Inst. 34 (2013) 3211–3218.

[29] Z. Tian, Y. Li, L. Zhang, P. Glarborg, F. Qi, An experimental and kinetic modeling study of premixed NH_3/CH_4/O_2/Ar flames at low pressure, Combust. Flame 156 (2009) 1413–1426.

[30] E.C. Okafor, Y. Naito, S. Colson, A. Ichikawa, T. Kudo, A. Hayakawa, H. Kobayashi, Experimental and numerical study of the laminar burning velocity of CH_4–NH_3–air premixed flames, Combust. Flame 187 (2018) 185–198.

[31] E.C. Okafor, Y. Naito, S. Colson, A. Ichikawa, T. Kudo, A. Hayakawa, H. Kobayashi, Measurement and modelling of the laminar burning velocity of methane-ammonia-air flames at high pressures using a reduced reaction mechanism, Combust. Flame 204 (2019) 162–175.

[32] L. Dai, S. Gersen, P. Glarborg, A. Mokhov, H. Levinsky, Autoignition studies of NH_3/CH_4 mixtures at high pressure, Combust. Flame 218 (2020) 19–26.

[33] S. Arunthanayothin, A. Stagni, Y. Song, O. Herbinet, T. Faravelli, F. Battin-Leclerc, Ammonia-methane interaction in jet-stirred and flow reactors: An experimental and

kinetic modeling study, Proc. Combust. Inst. 38 (2020) 345–353.

[34] L. Yu, W. Zhou, Y. Feng, W. Wang, J. Zhu, Y. Qian, X. Lu, The effect of ammonia addition on the low-temperature autoignition of *n*-heptane: An experimental and modeling study, Combust. Flame 217 (2020) 4–11.

[35] L. Dai, H. Hashemi, P. Glarborg, S. Gersen, P. Marshall, A. Mokhov, H. Levinsky, Ignition delay times of NH_3/DME blends at high pressure and low DME fraction: RCM experiments and simulations, Combust. Flame 227 (2021) 120–134.

[36] H. Kobayashi, A. Hayakawa, K.D.K.A. Somarathne, E.C. Okafor, Science and technology of ammonia combustion, Proc. Combust. Inst. 37 (2019) 109–133.

[37] E.C. Okafor, H. Yamashita, A. Hayakawa, K.D.K.A. Somarathne, T. Kudo, T. Tsujimura, M. Uchida, S. Ito, H. Kobayashi, Flame stability and emissions characteristics of liquid ammonia spray co-fired with methane in a single stage swirl combustor, Fuel 287 (2021) 119433.

[38] A.A. Khateeb, T.F. Guiberti, G. Wang, W.R. Boyette, M. Younes, A. Jamal, W.L. Roberts, Stability limits and NO emissions of premixed swirl ammonia-air flames enriched with hydrogen or methane at elevated pressures, Int. J. Hydrogen Energy 46 (2021) 11969–11981.

[39] Z. An, M. Zhang, W. Zhang, R. Mao, X. Wei, J. Wang, Z. Huang, H. Tan, Emission prediction and analysis on CH4/NH3/air swirl flames with LES-FGM method, Fuel 304 (2021) 121370.

[40] M. Yao, Z. Zheng, H. Liu, Progress and recent trends in homogeneous charge compression ignition (HCCI) engines, Prog. Energy Combust. Sci. 35 (2009) 398–437.

[41] S. Gersen, A. V. Mokhov, J.H. Darmeveil, H.B. Levinsky, P. Glarborg, Ignition-promoting effect of NO2 on methane, ethane and methane/ethane mixtures in a rapid compression machine, Proc. Combust. Inst. 33 (2011) 433–440.

[42] H. Zhao, L. Wu, C. Patrick, Z. Zhang, Y. Rezgui, X. Yang, G. Wysocki, Y. Ju, Studies of low temperature oxidation of *n*-pentane with nitric oxide addition in a jet stirred reactor, Combust. Flame (2018).

[43] Y. Song, L. Marrodán, N. Vin, O. Herbinet, E. Assaf, C. Fittschen, A. Stagni, T. Faravelli, M.U. Alzueta, F. Battin-Leclerc, The sensitizing effects of NO_2 and NO on methane low temperature oxidation in a jet stirred reactor, Proc. Combust. Inst. 37 (2019) 667–675.

[44] M.W. Slack, A.R. Grillo, Shock tube investigation of methane-oxygen ignition sensitized by NO_2, Combust. Flame 40 (1981) 155–172.

[45] C.L. Rasmussen, A.E. Rasmussen, P. Glarborg, Sensitizing effects of NOx on CH_4 oxidation at high pressure, Combust. Flame 154 (2008) 529–545.

[46] P. Dagaut, A. Nicolle, Experimental study and detailed kinetic modeling of the effect of exhaust gas on fuel combustion: Mutual sensitization of the oxidation of nitric oxide and methane over extended temperature and pressure ranges, Combust. Flame 140 (2005) 161–171.

[47] P. Dagaut, G. Dayma, Mutual sensitization of the oxidation of nitric oxide and a natural gas blend in a JSR at elevated pressure: Experimental and detailed kinetic modeling study, J. Phys. Chem. A 110 (2006) 6608–6616.

[48] M. Zhou, O.R. Yehia, C.B. Reuter, C.M. Burger, Y. Murakami, H. Zhao, Y. Ju, Kinetic effects of NO addition on *n*-dodecane cool and warm diffusion flames, Proc. Combust. Inst. 38 (2021) 2351–2360.

[49] F. Tagliante, T. Poinsot, L.M. Pickett, P. Pepiot, L.-M. Malbec, G. Bruneaux, C. Angelberger, A conceptual model of the flame stabilization mechanisms for a lifted Diesel-type flame based on direct numerical simulation and experiments, Combust. Flame 201 (2019) 65–77.

[50] A. Krisman, E.R. Hawkes, J.H. Chen, A parametric study of ignition dynamics at ECN Spray A thermochemical conditions using 2D DNS, Proc. Combust. Inst. 37 (2019) 4787–4795.

[51] A. Krisman, E.R. Hawkes, M. Talei, A. Bhagatwala, J.H. Chen, A direct numerical simulation of cool-flame affected autoignition in diesel engine-relevant conditions, Proc. Combust. Inst. 36 (2017) 3567–3575.

[52] R.N. Dahms, G.A. Paczko, S.A. Skeen, L.M. Pickett, Understanding the ignition mechanism of high-pressure spray flames, Proc. Combust. Inst. 36 (2017) 2615–2623.

[53] S. Deng, P. Zhao, D. Zhu, C.K. Law, NTC-affected ignition and low-temperature flames in nonpremixed DME/air counterflow, Combust. Flame 161 (2014) 1993–1997.

[54] A. Krisman, E.R. Hawkes, M. Talei, A. Bhagatwala, J.H. Chen, Characterisation of two-stage ignition in diesel engine-relevant thermochemical conditions using direct numerical simulation, Combust. Flame 172 (2016) 326–341.

[55] A.G. Novoselov, C.K. Law, M.E. Mueller, Direct Numerical Simulation of turbulent nonpremixed “cool” flames: Applicability of flamelet models, Proc. Combust. Inst. 37 (2019) 2143–2150.

[56] Y. Ju, C.B. Reuter, O.R. Yehia, T.I. Farouk, S.H. Won, Dynamics of cool flames, Prog. Energy Combust. Sci. 75 (2019) 100787.

[57] T. Zhang, Y. Ju, Structures and propagation speeds of autoignition-assisted premixed n-heptane/air cool and warm flames at elevated temperatures and pressures, Combust. Flame 211 (2020) 8–17.

[58] V. Nayagam, D.L. Dietrich, P. V. Ferkul, M.C. Hicks, F.A. Williams, Can cool flames support quasi-steady alkane droplet burning?, Combust. Flame 159 (2012) 3583–3588.

[59] S.H. Won, B. Jiang, P. Diévart, C.H. Sohn, Y. Ju, Self-sustaining n-heptane cool diffusion flames activated by ozone, Proc. Combust. Inst. 35 (2015) 881–888.

[60] C.B. Reuter, M. Lee, S.H. Won, Y. Ju, Study of the low-temperature reactivity of large n-alkanes through cool diffusion flame extinction, Combust. Flame 179 (2017) 23–32.

[61] A.G. Novoselov, C.B. Reuter, O.R. Yehia, S.H. Won, M.K. Fu, K. Kokmanian, M. Hultmark, Y. Ju, M.E. Mueller, Turbulent nonpremixed cool flames: Experimental measurements, Direct Numerical Simulation, and manifold-based combustion

modeling, Combust. Flame 209 (2019) 144–154.

[62] Y. Murakami, H. Nakamura, T. Tezuka, G. Asai, K. Maruta, Reactivity of $CO/H_2/CH_4$/Air Mixtures Derived from In-Cylinder Fuel Reformation Examined by a Micro Flow Reactor with a Controlled Temperature Profile, Combust. Sci. Technol. 193 (2021) 266–279.

[63] Y. Murakami, H. Nakamura, T. Tezuka, K. Hiraoka, K. Maruta, Effects of mixture composition on oxidation and reactivity of DME/NH_3/air mixtures examined by a micro flow reactor with a controlled temperature profile, Combust. Flame 238 (2022) 111911.

[64] Y. Murakami, C.B. Reuter, O.R. Yehia, Y. Ju, Studies of autoignition-assisted nonpremixed cool flames, Proc. Combust. Inst. 38 (2021) 2333–2340.

[65] K. Maruta, T. Kataoka, N. Kim, S. Minaev, R. Fursenko, Characteristics of combustion in a narrow channel with a temperature gradient, Proc. Combust. Inst. 30 (2005) 2429–2436.

[66] S. Minaev, K. Maruta, R. Fursenko, Nonlinear dynamics of flame in a narrow channel with a temperature gradient, Combust. Theory Model. 11 (2007) 187–203.

[67] H. Oshibe, H. Nakamura, T. Tezuka, S. Hasegawa, K. Maruta, Stabilized three-stage oxidation of DME/air mixture in a micro flow reactor with a controlled temperature profile 1300 K, Combust. Flame 157 (2010) 1572–1580.

[68] F.E. Fendell, Ignition and extinction in combustion of initially unmixed reactants, J.

Fluid Mech. 21 (1965) 281–303.

[69] M. Hori, H. Nakamura, T. Tezuka, S. Hasegawa, K. Maruta, Characteristics of *n*-heptane and toluene weak flames in a micro flow reactor with a controlled temperature profile, Proc. Combust. Inst. 34 (2013) 3419–3426.

[70] M. Hori, A. Yamamoto, H. Nakamura, T. Tezuka, S. Hasegawa, K. Maruta, Study on octane number dependence of PRF/air weak flames at 1–5 atm in a micro flow reactor with a controlled temperature profile, Combust. Flame 159 (2012) 959–967.

[71] A. Yamamoto, H. Oshibe, H. Nakamura, T. Tezuka, S. Hasegawa, K. Maruta, Stabilized three-stage oxidation of gaseous *n*-heptane/air mixture in a micro flow reactor with a controlled temperature profile, Proc. Combust. Inst. 33 (2011) 3259–3266.

[72] Y. Tsuboi, T. Yokomori, K. Maruta, Lower limit of weak flame in a heated channel, Proc. Combust. Inst. 32 (2009) 3075–3081.

[73] J. Topps, D. Townend, The light emission from cool and blue flames in the two-stage process of ignition of ether- and acetaldehyde-oxygen mixtures, Trans. Faraday Soc. 42 (1946) 345–351.

[74] S. Suzuki, M. Hori, H. Nakamura, T. Tezuka, S. Hasegawa, K. Maruta, Study on cetane number dependence of diesel surrogates/air weak flames in a micro flow reactor with a controlled temperature profile, Proc. Combust. Inst. 34 (2013) 3411–3417.

[75] S. Kikui, H. Nakamura, T. Tezuka, S. Hasegawa, K. Maruta, Study on combustion and ignition characteristics of ethylene, propylene, 1-butene and 1-pentene in a micro flow

reactor with a controlled temperature profile, 163 (2016) 209–219.

[76] H. Nakamura, S. Hasegawa, Combustion and ignition characteristics of ammonia/air mixtures in a micro flow reactor with a controlled temperature profile, Proc. Combust. Inst. 36 (2017) 4217–4226.

[77] S. Takahashi, H. Nakamura, T. Tezuka, S. Hasegawa, K. Maruta, Multi-stage oxidation of a CH_2F_2/air mixture examined by weak flames in a micro flow reactor with a controlled temperature profile, Combust. Flame 201 (2019) 140–147.

[78] S. Takahashi, H. Nakamura, T. Tezuka, K. Maruta, Effects of blending ratios on the reactivities of CH_2F_2/C_2HF_5 refrigerant blends, Proc. Combust. Inst. 38 (2020) 2487–2495.

[79] K. Seshadri, F.A. Williams, Structure and extinction of counterflow diffusion flames above condensed fuels: Comparison between poly(methyl methacrylate) and its liquid monomer, both burning in nitrogen–air mixtures, J. Polym. Sci. Polym. Chem. Ed. 16 (1978) 1755–1778.

[80] G. Asai, Y. Watanabe, S. Ishiguro, G. Shibata, H. Ogawa, Y. Kobashi, T. Suzuki, Diesel Fuel Reformation by Piston Compression of Rich Mixture, Trans. Soc. Automot. Eng. Japan 49 (2018) 24–29.

[81] H. Nakamura, H. Takahashi, T. Tezuka, S. Hasegawa, K. Maruta, K. Abe, Effects of CO-to-H_2 ratio and diluents on ignition properties of syngas examined by weak flames in a micro flow reactor with a controlled temperature profile, Combust. Flame 172

(2016) 94–104.

[82] E.L. Petersen, D.M. Kalitan, A.B. Barrett, S.C. Reehal, J.D. Mertens, D.J. Beerer, R.L. Hack, V.G. McDonell, New syngas/air ignition data at lower temperature and elevated pressure and comparison to current kinetics models, Combust. Flame 149 (2007) 244–247.

[83] J. Natarajan, T. Lieuwen, J. Seitzman, Laminar flame speeds of H_2/CO mixtures: Effect of CO_2 dilution, preheat temperature, and pressure, Combust. Flame 151 (2007) 104–119.

[84] A. Frassoldati, T. Faravelli, E. Ranzi, The ignition, combustion and flame structure of carbon monoxide/hydrogen mixtures. Note 1: Detailed kinetic modeling of syngas combustion also in presence of nitrogen compounds, Int. J. Hydrogen Energy 32 (2007) 3471–3485.

[85] F.L. Dryer, M. Chaos, Ignition of syngas/air and hydrogen/air mixtures at low temperatures and high pressures: Experimental data interpretation and kinetic modeling implications, Combust. Flame 152 (2008) 293–299.

[86] S.M. Walton, X. He, B.T. Zigler, M.S. Wooldridge, An experimental investigation of the ignition properties of hydrogen and carbon monoxide mixtures for syngas turbine applications, Proc. Combust. Inst. 31 (2007) 3147–3154.

[87] S. Gersen, H. Darmeveil, H. Levinsky, The effects of CO addition on the autoignition of H_2, CH_4 and CH_4/H_2 fuels at high pressure in an RCM, Combust. Flame 159 (2012)

3472–3475.

[88] O. Mathieu, J. Hargis, A. Camou, C. Mulvihill, E.L. Petersen, Ignition delay time measurements behind reflected shock-waves for a representative coal-derived syngas with and without NH_3 and H_2S impurities, Proc. Combust. Inst. 35 (2015) 3143–3150.

[89] A.B. Mansfield, M.S. Wooldridge, The effect of impurities on syngas combustion, Combust. Flame 162 (2015) 2286–2295.

[90] C. Liu, H. Song, P. Zhang, Z. Wang, M.S. Wooldridge, X. He, G. Suo, A rapid compression machine study of autoignition, spark-ignition and flame propagation characteristics of $H_2/CH_4/CO$/air mixtures, Combust. Flame 188 (2018) 150–161.

[91] Y. Murakami, H. Nakamura, T. Tezuka, S. Hasegawa, G. Asai, K. Maruta, Properties of in-cylinder fuel reformation and ignition characteristics of $CO/H_2/CH_4$ mixtures, in: 11th Asia-Pacific Conf. Combust. ASPACC 2017, 2017.

[92] T.C. Williams, C.R. Shaddix, Contamination of carbon monoxide with metal carbonyls: Implications for combustion research, Combust. Sci. Technol. 179 (2007) 1225–1230.

[93] ANSYS®, Chemkin-Pro, Release 19.0, Chemkin-Pro, Release 19.0, (2019).

[94] M. Kopp, M. Brower, O. Mathieu, E. Petersen, F. Güthe, CO_2* chemiluminescence study at low and elevated pressures, Appl. Phys. B Lasers Opt. 107 (2012) 529–538.

[95] M.M. Kopp, O. Mathieu, E.L. Petersen, Rate determination of the CO_2* chemiluminescence reaction $CO + O + M \rightleftarrows CO_2^* + M$, Int. J. Chem. Kinet. 47 (2014) 50–72.

[96] H. Wang, USC Mech Version II, J. Chem. Inf. Model. (2013).

[97] University of California at San Diego, Chemical-Kinetic Mechanisms for Combustion Applications, (2016).

[98] C.-W. Zhou, Y. Li, U. Burke, C. Banyon, K.P. Somers, S. Ding, S. Khan, J.W. Hargis, T. Sikes, O. Mathieu, E.L. Petersen, M. AlAbbad, A. Farooq, Y. Pan, Y. Zhang, Z. Huang, J. Lopez, Z. Loparo, S.S. Vasu, H.J. Curran, An experimental and chemical kinetic modeling study of 1,3-butadiene combustion: Ignition delay time and laminar flame speed measurements, Combust. Flame 197 (2018) 423–438.

[99] H. Zhao, J. Fu, F.M. Haas, Y. Ju, Effect of prompt dissociation of formyl radical on 1,3,5-trioxane and CH_2O laminar flame speeds with CO_2 dilution at elevated pressure, Combust. Flame 183 (2017) 253–260.

[100] X. Shen, X. Yang, J. Santner, J. Sun, Y. Ju, Experimental and kinetic studies of acetylene flames at elevated pressures, Proc. Combust. Inst. 35 (2015) 721–728.

[101] A. Kéromnès, W.K. Metcalfe, K.A. Heufer, N. Donohoe, A.K. Das, C.J. Sung, J. Herzler, C. Naumann, P. Griebel, O. Mathieu, M.C. Krejci, E.L. Petersen, W.J. Pitz, H.J. Curran, An experimental and detailed chemical kinetic modeling study of hydrogen and syngas mixture oxidation at elevated pressures, Combust. Flame 160 (2013) 995–1011.

[102] M.A. Mueller, T.J. Kim, R.A. Yetter, F.L. Dryer, Flow Reactor Studies and Kinetic Modeling of the H2/O2 Reaction, Int. J. Chem. Kinet. 31 (1999) 113–125.

[103] X.. Zheng, C.. Law, Ignition of premixed hydrogen/air by heated counterflow under

reduced and elevated pressures, Combust. Flame 136 (2004) 168–179.

[104] O. Mathieu, E.L. Petersen, Experimental and modeling study on the high-temperature oxidation of Ammonia and related NOx chemistry, Combust. Flame 162 (2015) 554–570.

[105] Z. Zhao, M. Chaos, A. Kazakov, F.L. Dryer, Thermal decomposition reaction and a comprehensive kinetic model of dimethyl ether, Int. J. Chem. Kinet. 40 (2008) 1–18.

[106] S.L. Fischer, F.L. Dryer, H.J. Curran, Reaction kinetics of dimethyl ether. I: high-temperature pyrolysis and oxidation in flow reactors, Int. J. Chem. Kinet. 32 (2000) 713–740.

[107] H.J. Curran, S.L. Fischer, F.L. Dryer, Reaction kinetics of dimethyl ether. II: Low-temperature pyrolysis and oxidation in flow reactors, Int. J. Chem. Kinet. 32 (2000) 741–759.

[108] C.B. Reuter, R. Zhang, O.R. Yehia, Y. Rezgui, Y. Ju, Counterflow flame experiments and chemical kinetic modeling of dimethyl ether/methane mixtures, Combust. Flame 196 (2018) 1–10.

[109] W. Huang, Q. Zhao, Z. Huang, H.J. Curran, Y. Zhang, A kinetics and dynamics study on the auto-ignition of dimethyl ether at low temperatures and low pressures, Proc. Combust. Inst. 38 (2020) 601–609.

[110] Y. Zhang, O. Mathieu, E.L. Petersen, G. Bourque, H.J. Curran, Assessing the predictions of a NOx kinetic mechanism on recent hydrogen and syngas experimental

data, Combust. Flame 182 (2017) 122–141.

[111] P. Glarborg, J.A. Miller, B. Ruscic, S.J. Klippenstein, Modeling nitrogen chemistry in combustion, Prog. Energy Combust. Sci. 67 (2018) 31–68.

[112] H. Nakamura, S. Hasegawa, T. Tezuka, Kinetic modeling of ammonia/air weak flames in a micro flow reactor with a controlled temperature profile, Combust. Flame 185 (2017) 16–27.

[113] A.A. Konnov, Implementation of the NCN pathway of prompt-NO formation in the detailed reaction mechanism, Combust. Flame 156 (2009) 2093–2105.

[114] P. Glarborg, J.A. Miller, B. Ruscic, S.J. Klippenstein, Modeling nitrogen chemistry in combustion, Prog. Energy Combust. Sci. 67 (2018) 31–68.

[115] P. Grajetzki, T. Onda, H. Nakamura, T. Tezuka, K. Maruta, Investigation of the chemical and dilution effects of major EGR constituents on the reactivity of PRF by weak flames in a micro flow reactor with a controlled temperature profile, Combust. Flame 209 (2019) 13–26.

[116] P. Dagaut, J. Luche, M. Cathonnet, The low temperature oxidation of DME and mutual sensitization of the oxidation of DME and nitric oxide: Experimental and detailed kinetic modeling, Combust. Sci. Technol. 165 (2001) 61–84.

[117] Y.L. Chan, J.H. Bromly, A.A. Konnov, D.K. Zhang, The comparative and combined effects of nitric oxide and higher alkanes in sensitizing methane oxidation, Combust. Sci. Technol. 184 (2012) 114–132.

[118] K.P. Shrestha, S. Eckart, A.M. Elbaz, B.R. Giri, C. Fritsche, L. Seidel, W.L. Roberts, H. Krause, F. Mauss, A comprehensive kinetic model for dimethyl ether and dimethoxymethane oxidation and NOx interaction utilizing experimental laminar flame speed measurements at elevated pressure and temperature, Combust. Flame 218 (2020) 57–74.

[119] Y.L. Chan, F.J. Barnes, J.H. Bromly, A.A. Konnov, D.K. Zhang, The differentiated effect of NO and NO2 in promoting methane oxidation, Proc. Combust. Inst. 33 (2011) 441–447.

[120] P. Dagaut, F. Lecomte, S. Chevailler, M. Cathonnet, Mutual sensitization of the oxidation of nitric oxide and simple fuels over an extended temperature range: Experimental and detailed kinetic modeling, Combust. Sci. Technol. 148 (1999) 27–57.

[121] S. Raimondeau, D. Norton, D.G. Vlachos, R.I. Masel, Modeling of high-temperature microburners, Proc. Combust. Inst. 29 (2002) 901–907.

[122] Y. Saiki, Y. Suzuki, Effect of wall surface reaction on a methane-air premixed flame in narrow channels with different wall materials, Proc. Combust. Inst. 34 (2013) 3395–3402.

[123] Y. Kizaki, H. Nakamura, T. Tezuka, S. Hasegawa, K. Maruta, Effect of radical quenching on CH4/air flames in a micro flow reactor with a controlled temperature profile, Proc. Combust. Inst. 35 (2015) 3389–3396.

[124] Z. Zhao, A. Kazakov, F.L. Dryer, Measurements of dimethyl ether/air mixture burning

velocities by using particle image velocimetry, Combust. Flame 139 (2004) 52–60.

[125] Y.L. Wang, P.S. Veloo, F.N. Egolfopoulos, T.T. Tsotsis, A comparative study on the extinction characteristics of non-premixed dimethyl ether and ethanol flames, Proc. Combust. Inst. 33 (2011) 1003–1010.

[126] C.A. Daly, J.M. Simmie, J. Würmel, N. DjebaÏli, C. Paillard, Burning velocities of dimethyl ether and air, Combust. Flame 125 (2001) 1329–1340.

[127] X. Qin, Y. Ju, Measurements of burning velocities of dimethyl ether and air premixed flames at elevated pressures, Proc. Combust. Inst. 30 (2005) 233–240.

[128] V.F. Zakaznov, L.A. Kursheva, Z.I. Fedina, Determination of normal flame velocity and critical diameter of flame extinction in ammonia-air mixture, Combust. Explos. Shock Waves 14 (1978) 710–713.

[129] K. Takizawa, A. Takahashi, K. Tokuhashi, S. Kondo, A. Sekiya, Burning velocity measurements of nitrogen-containing compounds, J. Hazard. Mater. 155 (2008) 144–152.

[130] U.J. Pfahl, M.C. Ross, J.E. Shepherd, K.O. Pasamehmetoglu, C. Unal, Flammability limits, ignition energy, and flame speeds in H2-CH4-NH3- N2O-O2-N2 mixtures, Combust. Flame 123 (2000) 140–158.

[131] P.D. Ronney, Effect of Chemistry and Transport Properties on Near-Limit Flames at Microgravity, Combust. Sci. Technol. 59 (1988) 123–141.

[132] A. Hayakawa, T. Goto, R. Mimoto, Y. Arakawa, T. Kudo, H. Kobayashi, Laminar

burning velocity and Markstein length of ammonia/air premixed flames at various pressures, Fuel 159 (2015) 98–106.

[133] M.U. Alzueta, R. Bilbao, M. Finestra, Methanol oxidation and its interaction with nitric oxide, Energy and Fuels 15 (2001) 724–729.

[134] P. Dagaut, G. Dayma, Mutual sensitization of the oxidation of nitric oxide and a natural gas blend in a JSR at elevated pressure: Experimental and detailed kinetic modeling study, J. Phys. Chem. A 110 (2006) 6608–6616.

[135] O. Mathieu, A. Levacque, E.L. Petersen, Effects of NO2 addition on hydrogen ignition behind reflected shock waves, Proc. Combust. Inst. 34 (2013) 633–640.

[136] L.S. Tran, J. Pieper, H.H. Carstensen, H. Zhao, I. Graf, Y. Ju, F. Qi, K. Kohse-Höinghaus, Experimental and kinetic modeling study of diethyl ether flames, Proc. Combust. Inst. 36 (2017) 1165–1173.

[137] J.H. Mack, D.L. Flowers, B.A. Buchholz, R.W. Dibble, Investigation of HCCI combustion of diethyl ether and ethanol mixtures using carbon 14 tracing and numerical simulations, Proc. Combust. Inst. 30 (2005) 2693–2700.

[138] S. Sivalakshmi, T. Balusamy, Effect of biodiesel and its blends with diethyl ether on the combustion, performance and emissions from a diesel engine, Fuel 106 (2013) 106–110.

[139] D.C. Rakopoulos, C.D. Rakopoulos, E.G. Giakoumis, A.M. Dimaratos, Studying combustion and cyclic irregularity of diethyl ether as supplement fuel in diesel engine,

Fuel 109 (2013) 325–335.

[140] D.H. Qi, H. Chen, L.M. Geng, Y.Z. Bian, Effect of diethyl ether and ethanol additives on the combustion and emission characteristics of biodiesel-diesel blended fuel engine, Renew. Energy 36 (2011) 1252–1258.

[141] O.R. Yehia, C.B. Reuter, Y. Ju, Kinetic effects of n-propylbenzene on *n*-dodecane counterflow nonpremixed cool flames, Combust. Flame 208 (2019) 262–272.

[142] L.S. Tran, O. Herbinet, Y. Li, J. Wullenkord, M. Zeng, E. Bräuer, F. Qi, K. Kohse-Höinghaus, F. Battin-Leclerc, Low-temperature gas-phase oxidation of diethyl ether: Fuel reactivity and fuel-specific products, Proc. Combust. Inst. 37 (2019) 511–519.

[143] Z. Tang, L. Zhang, X. Chen, G. Tang, Improved Kinetic Mechanism for Diethyl Ether Oxidation with a Reduced Model, Energy and Fuels 31 (2017) 2803–2813.

[144] Z. Serinyel, M. Lailliau, S. Thion, G. Dayma, P. Dagaut, An experimental chemical kinetic study of the oxidation of diethyl ether in a jet-stirred reactor and comprehensive modeling, Combust. Flame 193 (2018) 453–462.

[145] C.B. Reuter, S.H. Won, Y. Ju, Experimental study of the dynamics and structure of self-sustaining premixed cool flames using a counterflow burner, Combust. Flame 166 (2016) 125–132.

[146] S.K. Choi, S.H. Chung, Autoignited and non-autoignited lifted flames of pre-vaporized n-heptane in coflow jets at elevated temperatures, Combust. Flame 160 (2013) 1717–1724.

[147] B.C. Choi, K.N. Kim, S.H. Chung, Autoignited laminar lifted flames of propane in coflow jets with tribrachial edge and mild combustion, Combust. Flame 156 (2009) 396–404.

[148] B.C. Choi, S.H. Chung, Autoignited laminar lifted flames of methane, ethylene, ethane, and n-butane jets in coflow air with elevated temperature, Combust. Flame 157 (2010) 2348–2356.

[149] T. Boddington, J.F. Griffiths, K. Hasegawa, Induction times to thermal ignition in systems with distributed temperatures: An experimental test of theoretical interpretations, Combust. Flame 55 (1984) 297–305.

Acknowledgements

I would like to tell myself 4 years ago that my decision to be a Ph. D. student was truly right. I had a lot of enjoyable moments with ups and downs during my Ph. D., and they could not be better without all those who around me.

I would first like to express my sincere gratitude to my supervisor, Professor Hisashi Nakamura for all his guidance and support. He provided me many opportunities

to grow up as a researcher. He always has stood by me and given me responsibility from the first moment of my graduate school career. I am also grateful to Professor Kaoru Maruta for all his advice and support during my graduate study. He guided me with great passion for combustion science and gave me a lot of opportunities to see how the world works. He always provided me the best research environment and encouraged me constantly in a lot of ways. I would like to thank Professor Yiguang Ju for welcoming me at Princeton University as a visiting scholar. He inspired me a lot not only as a researcher but also as an educator through all the discussions and conversations we had. I only spent 10 months in Princeton, but the time and experience I had there completely changed my view of combustion research. I would also like to acknowledge Professor Hideaki Kobayashi and Professor Akihiro Hayakawa for putting in the time and effort to review this dissertation and for providing valuable advice. Professors Youhi Morii, Yuji Saito and Ajit Kumar Dubey helped me a lot for completing my Ph. D. study. Thank you all for the great communication and discussion at the lab. All my experiments could not have been done without the help by Mr. Takuya Tezuka. I appreciate his constant assistance deeply. I also thank Ms. Hiromi Ito and Ms. Reiko Chiba for helping me greatly in all the administrative works.

I also would like to acknowledge Dr. Go Asai and Dr. Kenji Hiraoka from Yanmar Holdings Co, Ltd. for their support through the collaborative works. I could have many insights and inspirations from our collaborations.

To my present and former lab members and visiting scholars, thank you for all the great assistance. Shintaro Takahashi, we experienced a lot of fun and struggles together throughout 6 years of our graduate school careers. My graduate school life would have been completely different without you. Starting with the road trip to Hokkaido, writing the JSPS proposal overnight, going snowboarding, relaxing at Hanjunmaku sauna after experiments, finding good restaurants, all of them made my life in Sendai a lot colorful and delightful. Keisuke Kanayama, Takaki Akiba, Keisuke Akita, you all helped and inspired me a lot in my graduate school life. I really enjoyed spending time with you all both at the lab and in private. It was always stimulating and amusing to discuss and share our thoughts not only about research but also about many interests. Taichi Mukouyama, Yoshimichi Yamamoto, Mayu Suzuki, Akira Tsunoda, Yoshiki Hirano, Kenta Tamaoki, Kazutaka Sagawa, Ayaka Hashimoto, Takumi Harada, Daiki Nakao and Kaito Hirose have been great lab members. They made the

lab a comfortable place and helped me in a lot of ways. I always enjoyed having fun time with you all.

To Ju's lab members, Omar Yehia, Aric Rousso, Hao Zhao, Francis Zhang, Timothy Chen, Hongtao Zhong, Wenbin Xu, Mengni Zhou are wonderful lab members. They welcome and helped me a lot during my stay in Princeton University. It was always exciting to talk about a lot of things with them. I especially would like to thank Omar Yehia, Mengni Zhou, Wenbin Xu for their support in cool flame experiments. Late night experiments we had were tough, but still exciting and enjoyable. My life in Princeton could not be better without your support.

Finally, I would like to thank my family for their constant support and encouragement in my educational pursuits. Even with the distance between Osaka and Sendai, my parents always have stood by me and encouraged me throughout my graduate life. It is always a very precious and irreplaceable moment for me to talk about everything with you both until late night when I come back to Osaka.

My sisters, Atsuko and Yoko, have been my greatest mentors and inspirations since when I was a kid. It is now a pleasure of my life to see how you both make your dreams come true. Akira is the best human being who brought joy and laughter to our entire family. I look forward to having more fun time together.

This work had been mainly carried out at the Institute of Fluid Science, Tohoku University, Japan and at Princeton University, USA. I acknowledge the financial support from the Research Fellowship Program for Young Scientists provided by the Japan Society for the Promotion of Science, Grants-in-Aid for JSPS Fellows Grant Number 19J11887.

January 11, 2022
Yuki Murakami